

Design and Development of the Phoenix-1B Hybrid Rocket

Udil Balmogim

Submitted in fulfilment of the academic requirements for the degree of Master of Science in Mechanical Engineering, College of Agriculture, Engineering and Science, University of KwaZulu-Natal.

Durban, South Africa

March 2017

Supervisors: Dr. Michael J. Brooks

Co-Supervisor: Mr. Jean-Francois Pitot de la Beaujardiere

Co-Supervisor: Ms. Kirsty Veale

Declaration 1: Plagiarism

I, Udil Balmogim, declare that,

- i. The research reported in this dissertation/thesis, except where otherwise indicated, is my original work.
- ii. This dissertation/thesis has not been submitted for any degree or examination at any other university.
- iii. This dissertation/thesis does not contain other persons' data, pictures, graphs or other information, unless specifically acknowledged as being sourced from other persons.
- iv. This dissertation/thesis does not contain other persons' writing, unless specifically acknowledged as being sourced from other researchers. Where other written sources have been quoted, then:
 - a. Their words have been re-written but the general information attributed to them has been referenced;
 - b. Where their exact words have been used, their writing has been placed inside quotation marks, and referenced.
- v. Where I have reproduced a publication of which I am an author, co-author or editor, I have indicated in detail which part of the publication was actually written by myself alone and have fully referenced such publications.
- vi. This dissertation/thesis does not contain text, graphics or tables copied and pasted from the Internet, unless specifically acknowledged, and the source being detailed in the dissertation/thesis and in the References sections.

Signed:..... Date:.....

Mr Udil Balmogim

Declaration 2: Publications

Balmogim U.*, Brooks M., Pitot de la Beaujardiere J.P., Veale K., Genevieve B. and Roberts L.W., “Preliminary Design of the Phoenix-1B Hybrid Rocket”, 51st AIAA/ASME/SAE/ASEE Joint Propulsion Conference and Exhibit, Orlando, Florida, July 2015.

Genevieve B., Pitot J., Brooks M., Chowdhury S., Veale K., Leverone F., Balmogim U.† and Mawbey R., “Flight Test of the Phoenix-1A Hybrid Rocket”, 51st AIAA/ASME/SAE/ASEE Joint Propulsion Conference and Exhibit, Orlando, Florida, July 2015.

*Primary author

†Co-author

Signed:..... Date:.....

Mr Udil Balmogim

As the candidate’s supervisor I agree/do not agree to the submission of this thesis.

Signed:..... Date:.....

Dr. Michael J. Brooks

As the candidate’s co-supervisor I agree/do not agree to the submission of this thesis.

Signed:..... Date:.....

Mr. Jean-Francois Pitot de la Beaujardiere

As the candidate’s co-supervisor I agree/do not agree to the submission of this thesis.

Signed:..... Date:.....

Ms. Kirsty Veale

Acknowledgements

My sincere thanks and deep appreciation to the following:

- My supervisors, Dr. Michael Brooks, Mr. Jean Pitot and Ms. Kirsty Veale, for their guidance and patience throughout this research project. Indeed without their mentorship, this project would have not been possible.
- Mr. Bernard Genevieve for his guidance and selfless assistance for the duration of this work.
- Mr. Timothy Velthuysen and Mr. Chikhar Maharaj for their assistance with the rocket assembly and testing preparations.
- Ms. Fiona Leverone, for her assistance with HYROPS and many hours spent generating launch footprints.
- The Aerospace Systems Research Group (ASReG): Mr. Donald Fitzgerald, Mr. Creason Chetty, Mr. Nalendran Singh and Ms. Raisa Theba, for their assistance with the testing preparations.
- The UKZN Mechanical engineering workshop technicians for their advice on CNC machining best practices.
- The South African National Space Agency (SANSA) for providing financial support through their bursary, as well as funding my journey to the 64th International Astronautical Congress (IAC) in Toronto, Canada.
- Rheinmetall Denel Munition (RDM) and in particular Mr. Charl Barnard for his advice on nozzle design and manufacturing of the rocket nozzles at no cost to the project.
- Overberg Test Range (OTR) and in particular Mr. Danie Henning for his patience and understanding and Mr. Leon Korkie for his selfless assistance with the telemetry system.
- My brother, Mr. Nesham Balmogim, for his assistance with telemetry design and the understanding of the IRIG standards.
- Fibrewound and in particular Mr. Scott McClure for his advice on the composite design of the rocket nose and fin can.
- Assured Quality Engineering for their guidance on CNC machining.
- The South African Air Force (SAAF) for sponsoring the use of the Overberg Test Range.
- The National Research Foundation (NRF) Thuthuka grant for financial contributions.

Last but not least, thank you to my parents, Mr. Manilall Balmogim and Mrs. Initha Balmogim, and my brothers Nesham and Kershan Balmogim for their never ending support, patience and understanding. Thank you to my friends for providing humour during stressful times.

Abstract

In August 2014, South Africa's first university-based hybrid rocket, Phoenix-1A, was launched at the Overberg Test Range near Cape Agulhas. The vehicle suffered nozzle and parachute failures during flight which, together with a reduced oxidiser load, reduced the nominal design apogee of 10 km to 2.5 km. The aim of this research was to improve on the design and performance of the prototype demonstrator and thereby develop a workhorse hybrid sounding rocket, named Phoenix-1B, to serve as a reliable platform for future hybrid rocket research at the University of KwaZulu-Natal (UKZN). Analysis of Phoenix-1A shortcomings served as the starting point for the new design, which utilises a paraffin wax and nitrous oxide propellant combination. The focus of this research was the propulsion system, with specific attention being paid to the nozzle and injector designs. In addition, an aerodynamic study was applied to the 1 m long $\frac{3}{4}$ parabolic nose cone and four tapered swept fins. Final design of the aluminium oxidiser tank and combustion chamber bulkheads incorporated finite element analyses to ensure an operational safety factor greater than 1.5. The oxidiser tank and combustion chamber assemblies were pressure tested to 80 and 60 bars respectively. A key output of the present work is an analysis of the effect of aluminium loading in the paraffin wax fuel grain, which indicated a potential rocket mass reduction of 23 kg when transitioning from a pure paraffin grain to one containing 40% aluminium by mass. The analysis also indicated that combustion temperature rises with aluminium loading, increasing from 3300 K for pure paraffin to 3600 K for 40% aluminised fuel. Consequently, an iterative transient thermo-structural analysis was conducted on the nozzle, resulting in an optimised design able to sustain the higher operating temperatures as well as mitigate the risk of failure as seen with Phoenix-1A. The final manufactured composite nozzle has a throat diameter of 32 mm, an expansion ratio of 6.38, and a length of 156 mm. The nozzle has a steel casing which provides structural support to the silica phenolic insulation and graphite throat insert. A two phase CFD analysis, coupled with analytical mass flow rate models, was used to configure the axial injector and reduce the potential for combustion instabilities associated with the nitrous oxide flow. The Phoenix-1B motor has a design thrust of 5 kN to propel the fully loaded vehicle, with a mass of 70 kg, a length of 4.3 m and a diameter of 164 mm, to an altitude of 16 km.

Table of Contents

Declaration 1: Plagiarism	ii
Declaration 2: Publications	iii
Acknowledgements.....	iv
Abstract	v
List of Figures.....	x
List of Tables.....	xiv
Nomenclature	xvi
1. Introduction	1
1.1. Background.....	1
1.1.1. Rocket propulsion.....	1
1.1.2. Sounding rockets	3
1.2. Phoenix history	4
1.3. Phoenix-1B objectives.....	4
1.4. Dissertation outline.....	5
2. Phoenix-1B Design Criteria.....	7
2.1. Introduction.....	7
2.2. Phoenix-1A Hybrid Sounding Rocket	7
2.2.1. P1A vehicle design	7
2.2.2. P1A hot fire test and GSE	9
2.2.3. P1A flight test.....	11
2.3. P1B design evolution.....	14
2.3.1. P1A cost and mass analysis.....	14
2.3.2. Oxidiser tank	14
2.3.3. Airframe manufacture.....	15
2.3.4. Recovery system.....	17
2.3.5. Nozzle failure	18
2.3.5. GSE improvements	19

2.4. Summary.....	20
3. Phoenix-1B Hybrid Propulsion System Design.....	21
3.1. Introduction.....	21
3.2. Hybrid rocket internal ballistics	21
3.3 Design and simulation programs.....	26
3.3.1. Hybrid rocket performance code	27
3.3.2. 6 DOF flight dynamics simulator	28
3.4. Aluminium loading effects study	30
3.4.1. Aim and methodology of study	30
3.4.2. Effect of metallisation on hybrid motor design and performance	32
3.4.3. Effect on nozzle.....	35
3.5. P1B system level design.....	39
3.5.1. Design methodology.....	39
3.5.2. P1B specifications	40
3.6. Summary.....	45
4. Phoenix-1B Propulsion System Component Design.....	46
4.1. Introduction.....	46
4.2. Instrumentation and feed system.....	46
4.3. Bulkhead retention methods	48
4.3.1. Spiral locking ring	48
4.3.1. Bolted bulkheads	52
4.4. P1B pressure vessel.....	54
4.4.1. Oxidiser and combustion chamber shell	54
4.4.2. Bulkheads.....	55
4.4.3. Manufacturing and pressure testing.....	59
4.6. Summary.....	60
5. Phoenix-1B Nozzle Design and Analysis.....	61
5.1. Introduction.....	61

5.2. Design of rocket nozzles	61
5.2.1. Background	61
5.2.2. Design methodology	64
5.2.3. Design requirements and constraints	65
5.2.4. Nozzle erosion	66
5.2.5. Design assumptions	67
5.3. Thermo-structural methodology	68
5.4. Nozzle loading	68
5.4.1 Aluminised fuel motor specifications	68
5.4.2. Thermal loading	72
5.4.2. Structural loading	76
5.4.3. Temporal and spatial modelling	76
5.5. Thermo-structural analysis	78
5.5.1. 40% Aluminised fuel grain nozzle design.....	78
5.5.2. 2D axisymmetric analysis	81
5.5.2. 3D cyclic analysis.....	83
5.6. Discussion.....	86
5.7. Summary.....	88
6. Phoenix-1B Injector Design and Analysis	89
6.1. Introduction.....	89
6.2. Injector design.....	89
6.2.1. Combustion instabilities in hybrid rocket motors.....	89
6.2.2. Injector type	91
6.3 Mass flow rate modelling	93
6.4. Two phase CFD and final design	96
6.6. Summary.....	99
7. Phoenix-1B aerodynamics	100
7.1. Introduction.....	100

7.2. Nose cone design.....	100
7.3. Fin design.....	103
7.5 Summary.....	104
8. Final design and testing of Phoenix-1B.....	105
8.1. Introduction.....	105
8.2. P1B vehicle design comparison	105
8.3. Cold flow test	109
8.4. Summary.....	113
9. Conclusion and recommendations	114
9.1. Overview	114
9.2. Conclusions.....	114
9.3. Recommendations and future work.....	117
References	118
Appendix A : Nozzle design flow chart.....	123
Appendix B : MATLAB code for nozzle loading calculations	124
Appendix C : Manufacturing drawings	132
Appendix D : Videos	140

List of Figures

Chapter 1

Figure 1.1: Chemical rocket propulsion systems (Leverone, 2013)	2
Figure 1.2: Hybrid rocket schematic (Leverone, 2013)	2
Figure 1.3: Sounding rocket flight trajectory and events (Marconi, 2016)	3
Figure 1.4: Phoenix-1B Hybrid Sounding Rocket	6

Chapter 2

Figure 2.1: CAD rendition of P1A cross section (Chowdhury, 2012).....	7
Figure 2.2: P1A Hot Fire Test on the MLP, adapted from ASReG UKZN (2013)	10
Figure 2.3: Comparison of P1A hot fire and theoretical design data	11
Figure 2.4: Conical injector used during P1A hot fire test (Genevieve, 2013)	11
Figure 2.5: (a) P1A in launch position on MLP; (b) P1A leaving the launch pad at OTR (Genevieve, et al., 2015)	12
Figure 2.6: P1A flight path and trajectory	13
Figure 2.7: Flight dynamics of P1A (Genevieve, et al., 2015)	13
Figure 2.8: Relative cost (a) and mass (b) of P1A	14
Figure 2.9: P1A oxidiser tank showing increased wall thickness (Chowdhury, 2012).....	15
Figure 2.10: P1A interstage connecting the oxidiser tank to the combustion chamber (Balmogim, et al., 2015).....	15
Figure 2.11: P1A upper airframe showing parachute separation, (top) drogue deployment, (bottom) main deployment	16
Figure 2.12: (a) Fibre layup, (b) layer compaction with packaging tape	16
Figure 2.12 (cont.): (c) layup enclosed in heat shrink tape before oven curing, (d) cured layup being machined.....	17
Figure 2.13: Drogue parachute deployment (Balmogim, et al., 2015).....	17
Figure 2.14: Retrieval of shock cord from impact site.....	18
Figure 2.15: (a) Ignition and rocket movement, (b) nozzle failure, (c) boat tail ejection (Genevieve, et al., 2015)	18
Figure 2.16: (a) Nozzle failure and remains of nozzle retainer showing burn through, (b) clearance between nozzle and nozzle retainer (adapted from Genevieve (2013))	19

Chapter 3

Figure 3.1: Diffusion layer combustion in a hybrid motor (Humble and Altman, 1995).....	21
---	----

Figure 3.2: Visualisation of the boundary layer and energy balance in a hybrid motor (Zilliac and Karageyoglu, 2006).....	22
Figure 3.3: Entrainment mechanism in non-classical fuel grains showing roll waves (Karabeyoglu, 2012)	25
Figure 3.4: Hierarchy model of HYROPS (Leverone, 2013).	27
Figure 3.5: HRPC motor design	28
Figure 3.6: Hybrid rocket performance simulator	28
Figure 3.7: Start up GUI of HYROPS	29
Figure 3.8: Methodology for aluminised fuel grain study.....	31
Figure 3.9: Interpolated regression rate coefficient and density data.....	32
Figure 3.10: C^* variation with O/F ratio for different aluminium loadings	33
Figure 3.11: Increase in density specific impulse with increasing aluminium loading.....	34
Figure 3.12: Booster length reduction with increasing aluminium loading (Balmogim, et al., 2015)	35
Figure 3.13: Combustion temperature variation for different aluminium loadings	36
Figure 3.14: Mole Fraction of liquid phase alumina in nozzle	37
Figure 3.15: Mole Fraction of solid phase alumina in nozzle	37
Figure 3.16: Temperature distribution in nozzle.....	37
Figure 3.17: Oxidising species for (a) 10%, (b) 20%, (c) 30%, (d) 40%	38
Figure 3.17 (cont.): (e) 50% aluminium loading	39
Figure 3.18: P1B design methodology.....	40
Figure 3.19: Characteristic velocity VS O/F ratio for varying combustion pressure.....	41
Figure 3.20: HRPC nozzle nomenclature, (a) bell nozzle, (b) conical nozzle (Genevieve, 2013)	43
Figure 3.21: Theoretical P1B pressure and thrust time traces	43
Figure 3.22: Combustion temperature time trace	44

Chapter 4

Figure 4.1: Schematic of propulsion system with sensors	47
Figure 4.2: Cross section of retaining ring design (Balmogim, et al., 2015).....	49
Figure 4.3: Von Mises stresses of retainer ring design for internal pressure of 65 bar.	51
Figure 4.4: Von Mises stress with 10x scaled deformation (a) close up spiral ring region, (b) Iso-capped surface showing stresses higher than 276 MPa.....	51
Figure 4.5: (a) Tube deformation and ring movement; (b) Pressure vessel failure at 150 bars (Balmogim, et al., 2015)	52
Figure 4.6: Bolted bulkhead FEA model.....	53

Figure 4.7: (a) Von Mises stress on shell, (b) Close-up of high stress area (deformation scaled up 20x)	53
Figure 4.8: Bolt-pretension study	54
Figure 4.9: P1B propulsion system illustrating location of bulkheads.....	55
Figure 4.10: Coupler mount	56
Figure 4.11: (Left) fore bulkhead assembly, (right) Von Mises stresses in Pascal.....	56
Figure 4.12: Schematic of vent system	57
Figure 4.13: (Left) aft bulkhead assembly and (right) Von Mises stresses in Pascal	58
Figure 4.14: (Left) injector bulkhead assembly and (right) Von Mises stresses in Pascal.....	58
Figure 4.15: (a) Fore bulkhead assembly, (b) aft bulkhead assembly, (c) injector bulkhead assembly.....	59
Figure 4.16: Pressure testing setup of (a) oxidiser tank and (b) combustion chamber	60

Chapter 5

Figure 5.1: Approximate optimization approach (Seitzman, 2012).....	63
Figure 5.2: Nozzle design angles (adapted from Sutton and Biblarz (2001))	64
Figure 5.3: Nozzle design methodology used for P1B.....	65
Figure 5.4: Physiochemical processes in a nozzle causing erosion (Thakre, 2008)	66
Figure 5.5: Thermo-structural methodology	68
Figure 5.6: Pressure and thrust time traces for 40% aluminised fuel.....	71
Figure 5.7: Combustion temperature for 40% aluminised fuel grain.....	72
Figure 5.8: Convective heat transfer coefficient along nozzle contour at instantaneous 40 bar chamber pressure	77
Figure 5.9: Pressure and temperature variation along nozzle contour at instantaneous 40 bar chamber pressure	77
Figure 5.10 : Temporal and spatial modelling methodology.....	78
Figure 5.11: Cross section of the final nozzle design for 40% aluminised fuel grain motor.....	79
Figure 5.12: Close-up of nozzle showing dimples.....	79
Figure 5.13: Spatial and temporal convective heat transfer coefficient distribution through the nozzle for a 40% aluminised grain.....	80
Figure 5.14: Spatial and temporal pressure distribution through the nozzle for a 40% aluminised grain.	80
Figure 5.15: Spatial and temporal temperature distribution through the nozzle for a 40% aluminised grain.....	81
Figure 5.16: Temperature distribution in the nozzle insulation components (left) and in the structure (right)	82

Figure 5.17: Temperature distribution at end of burn for the model including RTV adhesive (left) and the simplified case (right)	82
Figure 5.18: Cyclic symmetry 3D model for final thermo-structural analysis	83
Figure 5.19: Temperature distribution at (a) 5 s, (b) 10 s and (c) 15 s.....	85
Figure 5.20: Von Mises stress distribution on nozzle structure at (a) 5 s, (b) 10 s and (c) 15 s ..	85
Figure 5.21: Comparison of convective heat transfer between 40% aluminised fuel and pure paraffin fuel at 40 bar chamber pressure	86
Figure 5.22: Manufactured P1B nozzle components	87
Figure 5.23: Completed P1B nozzle with bonded components	87

Chapter 6

Figure 6.1: Pressure time traces of hot fire with impinging injector (Waxman, et al., 2010)	91
Figure 6.2: Pressure time traces of hot fire with axial injector (Waxman, et al., 2010).....	91
Figure 6.3: (a) Axial injection and (b) impinging injection in a hybrid rocket motor (Sutton and Biblarz, 2001).....	92
Figure 6.4: Nitrous oxide vapour pressure vs temperature.....	93
Figure 6.5: Nitrous oxide density vs temperature	93
Figure 6.6: Nitrous oxide compressibility factor vs temperature.....	94
Figure 6.7: Injector orifice cross section defining flow parameters (Soloman, 2011)	94
Figure 6.8: Nitrous oxide vapour volume fraction for (top) 65 bar upstream and 40 bar downstream pressure and (bottom) 57 bar upstream and 38 bar downstream pressure	97
Figure 6.9: Cross-sectional rendition of the combustion chamber fore end.....	98
Figure 6.10: (a) Injector plate installed on the vehicle in readiness for cold flow testing, (b) view of the 60 one millimetre diameter orifices of the injector plate.....	98

Chapter 7

Figure 7.1: Nose cone shape selection chart (Minnesota and Stroick, 2011)	100
Figure 7.2: Coefficient of drag as a function of Mach number	101
Figure 7.3: Mach distribution for P1B at Mach 1.1	102
Figure 7.4: Pressure distribution on nose cone	102
Figure 7.5: Manufactured nose cone.....	102
Figure 7.6: Fin design nomenclature (Chowdhury, 2012).....	103
Figure 7.7: P1B fin can installed on the combustion chamber	104

Chapter 8

Figure 8.1: Simulated ballistic trajectory and speed of P1B for a launch angle of 80° with no wind at Overberg Test Range.....	108
Figure 8.2: Cross-section rendition of the final design of P1B	108
Figure 8.3: P1B Cold flow test	109
Figure 8.4: Pressure VS time traces of the liquid and vapour pressure in the flight tank for test duration	110
Figure 8.5: Pressure VS time traces of the liquid and vapour pressure in the flight tank until quick-connect failure	110
Figure 8.6: Injector plume development	111
Figure 8.7: Injector plate being ejected from the injector bulkhead during cold flow test.....	111
Figure 8.7 (cont.): Injector plate being ejected from the injector bulkhead during cold flow test	112
Figure 8.8: (a) Injector plate damage after impact, (b) injector bulkhead.....	112
Figure 8.9: Cross-section rendition of the improved injector bulkhead design	112

Appendix A

Figure A.1: Standard nozzle design procedure (NASA, 1975)	123
---	-----

Appendix C

Figure C.1: Combustion chamber casing	133
Figure C.2: Oxidiser tank shell.....	134
Figure C.3: Fore bulkhead.....	135
Figure C.4: Aft bulkhead.....	136
Figure C.5: Injector bulkhead.....	137
Figure C.6: Coupler mount.....	138
Figure C.7: Injector plate	139

List of Tables

Chapter 2

Table 2.1: P1A vehicle specifications, adapted from Geneviève (2013) and Chowdhury (2012)..8	
Table 2.2: P1A vehicle performance, adapted from Geneviève (2013) and Chowdhury (2012) ..9	
Table 2.3: P1A flight events	13

Chapter 3

Table 3.1: Ballistic coefficients and regression rate at an oxidiser mass flux of 1000 kg/s.m ² ...	24
Table 3.1 (cont.): Ballistic coefficients and regression rate at an oxidiser mass flux of 1000 kg/s.m ²	25
Table 3.2: Effect of aluminium loading on motor performance	33
Table 3.3: Effect of aluminium loading on booster mass.....	34
Table 3.4: Effect of aluminium loading on booster dimensions	34
Table 3.5: P1B steady state design specifications	41
Table 3.5(cont.): P1B steady state design specifications.....	42
Table 3.6: Nozzle design specifications	42
Table 3.7: Time-averaged performance parameters for P1B.....	44

Chapter 4

Table 4.1: Density coefficients for nitrous oxide (Green and Perry, 2008)	48
Table 4.2: Carbon steel material properties (Smalley , 2015)	50
Table 4.3: Aluminium 6061-T6 material properties (MatWeb, 2016).....	50
Table 4.4: Analytical results of spiral retaining ring design.....	50
Table 4.5: Safety factors the oxidiser and combustion chamber vessels	60

Chapter 5

Table 5.1: 40% aluminised fuel grain and nozzle specifications	69
Table 5.2: Nozzle specifications for 40% aluminised fuel grain, nomenclature correlates to Figure 3.20	70
Table 5.3: Time-averaged motor performance parameters for a 40% aluminised paraffin fuel grain	70
Table 5.3 (cont.): Time-averaged motor performance parameters for a 40% aluminised paraffin fuel grain.....	71

Chapter 7

Table 7.1: P1B fin dimensions	103
-------------------------------------	-----

Chapter 8

Table 8.1: Design specification comparison between P1A and P1B	106
Table 8.1(cont.): Design specification comparison between P1A and P1B.....	107
Table 8.2: Theoretical performance comparison between P1A and P1B.....	107

Nomenclature

Symbols

Symbol	Description	Units
A	Area	m^2
a	Ballistic coefficient	-
Bi	Biot number	-
C^*	Characteristic velocity	m/s
C	Coefficient	-
Cd	Coefficient of drag or coefficient of discharge	-
C_f	Coefficient of thrust	-
c_r	Root chord	m
c_t	Tip chord	m
D	Diameter	m
d	Groove depth	m
F	Force or Thrust	N
G	Mass flux	$kg/m^2 \cdot s$
h	Enthalpy or height	J/kg
K	Parabola constant	-
k	Conductivity	$W/m^2 \cdot K$
L	Length	m
M	Mach number	-
MW	Molecular Weight	g/mol
m	Ballistic exponent related to port length or mass	-
\dot{m}	Mass flow rate	kg/s
N	Number	-
Nu	Nusselt number	-
n	Ballistic exponent related to propellant combination	-
P	Pressure	Pa
Pr	Prandtl number	-
\dot{Q}	Rate of heat transfer	J/s
\dot{q}	Specific rate of heat transfer	$J/kg \cdot s$
\dot{r}	Regression rate	m/s
r	Radius	m
r_i	Root span	m

R	Radius	m
Re	Reynolds number	-
S	Strength	Pa
s	Wing span	m
SF	Safety factor	-
T	Temperature	K
t	Thickness	m
U	Velocity	m/s
u	Velocity	m/s
\dot{V}	Volumetric flow rate	m ³ /s
w	Sweep	m
x	Axial length or position	m
y	Radial length	m

Greek

Symbol	Description	Units
α	Thermal diffusivity	m ² /s
β	Blowing/blocking factor	-
γ	Ratio of specific heats	-
ε	Emissivity or expansion ratio	-
θ	Launch angle	m ²
κ	Non-equilibrium factor	-
μ	Viscosity	Pa · s
ρ	Density	kg/m ³
σ	Stefan-Boltzmann constant or stress or correction factor	W/m ² · K ⁴
τ	Time	s
∞	Free stream	-

Subscripts

Symbol	Description
a	Ambient
aw	Adiabatic wall
b	Burning surface or bubble
c	Characteristic or pertaining to the flame

<i>e</i>	Exit plane
<i>f</i>	Fuel or final
<i>g</i>	Gas
<i>inj</i>	Injector
<i>l</i>	Liquid
<i>N₂O</i>	Nitrous oxide
<i>n</i>	Nozzle
<i>ox</i>	Oxidiser
<i>p</i>	Port
<i>r</i>	Residence
<i>s</i>	Surface or shear
<i>t</i>	Throat
<i>tot</i>	Total
<i>v</i>	Vapor
<i>wg</i>	Gas side wall
<i>y</i>	Yield
<i>0</i>	Stagnation or total

Abbreviations

Acronym	Description
ASReG	Aerospace Systems Research Group
CAE	Computer aided engineering
CEA	Chemical Equilibrium with Applications
CFD	Computational fluid dynamics
CFRP	Carbon fibre reinforced plastic
DOF	Degree of freedom
FEA	Finite element analysis
FPS	Frames per second
GFRP	Glass fibre reinforced plastic
GUI	Graphical user interface
GSE	Ground support equipment
HEM	Homogenous equilibrium model
HDPE	High density polyethylene
HRPC	Hybrid Rocket Performance Code
HSR	Hybrid Sounding Rocket

HSRP	Hybrid Sounding Rocket Programme
HTPB	Hydroxyl-terminated polybutadiene
HYROPS	Hybrid rocket performance simulator
LOX	Liquid oxygen
LP	Launch pad
MEOP	Maximum expected operating pressure
MLP	Mobile launch platform
MOV	Main oxidiser valve
N ₂ O	Nitrous oxide
NASA	National Aeronautics and Space Administration
NHNE	Non-homogeneous Non-equilibrium
NI	National Instruments
OD	Outer diameter
O/F	Oxidiser-to-fuel ratio
OTR	Overberg test range
P1A	Phoenix-1A
P1B	Phoenix-1B
PDB	Propellant distribution board
UKZN	University of KwaZulu-Natal
RTV	Room temperature vulcanising silicone

Constants

Symbol	Value	Description
g	9.81 m/s ²	Gravity
σ	5.6704 x 10 ⁻⁸ W/m ² · K ⁴	Stefan-Boltzmann

1. Introduction

1.1. Background

1.1.1. Rocket propulsion

Rocket propulsion is a class of jet propulsion in which stored mass, known as propellant, is combusted and ejected from the vehicle at high velocity. Under the conservation of momentum and Newton's third law, a force is generated in the opposite direction to the ejected fluid propelling the vehicle. Kinetic energy is imparted to the propellant from an energy source, thus producing the necessary high propellant velocities and consequently the thrust. There are three classes of rocket propulsion, namely chemical, nuclear and solar (Sutton and Biblarz, 2001). In a thermal nuclear rocket, energy from a nuclear reactor is used to heat propellant to high temperatures before expanding through a nozzle (Babula, 2016). Nuclear rockets are not currently used in modern propulsion systems due to radioactive risk and high cost. Solar thermal rockets are rarely employed and work on the same principle as the nuclear variant, but use solar energy as the heat source. Chemical rocket propulsion is the most commonly used system. The controlled reaction of the onboard oxidiser and fuel generates an extremely high temperature gas that is expanded through the nozzle, converting the thermal energy of the gas into kinetic energy and accelerating the flow.

Chemical rockets can be grouped into three categories, namely liquid, solid and hybrid. As the name suggests, liquid propellant rockets use liquid propellants that are fed into a thrust chamber at high pressures. Feeding of propellant to the thrust chamber is achieved either with a pump system or a pressure differential system (i.e. pressure-fed). Liquid propellants can further be classed into monopropellant and bi-propellant depending on whether there are one or two propellants. Solid propellant rocket motors consist of a single solid grain that is a mixture of a fuel and oxidiser. Solid fuelled rockets have the highest energy density in comparison to the other propulsion systems. Liquid rockets also have a relatively high energy density but offer substantial control over thrust generation by regulating the flow of fuel and oxidiser into the combustion chamber.

Hybrid propulsion systems are a middle ground between liquid bi-propellant and solid fuelled rockets. The fuel and oxidiser are stored in two different phases and are allowed to react in a controlled manner only when needed. Generally, the oxidiser is stored as a liquid and the fuel as a solid, however, there have been some instances where the reverse configuration was used. Figure 1.1 shows a schematic of the different chemical rocket propulsion systems.

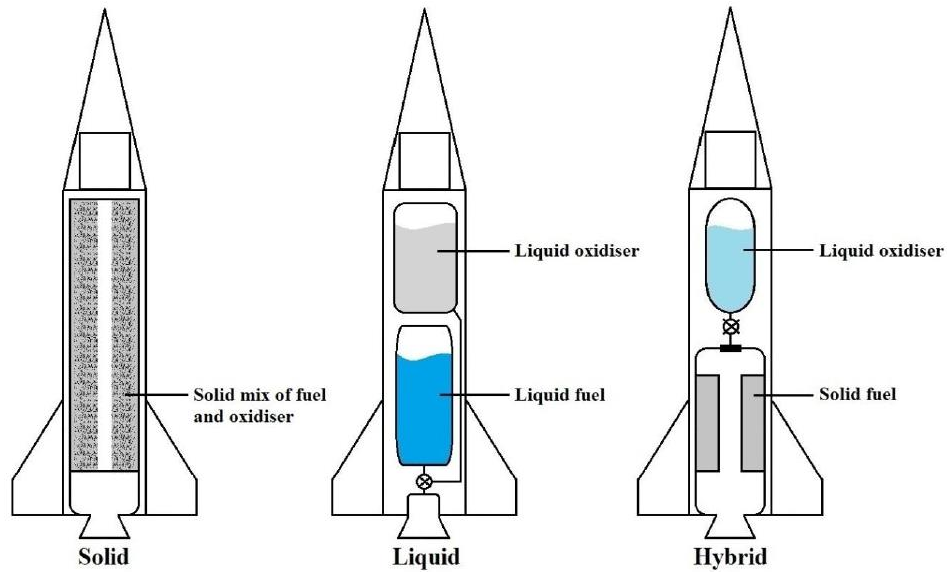


Figure 1.1: Chemical rocket propulsion systems (Leverone, 2013)

The standard hybrid rocket schematic is shown in Figure 1.2. In its base form, a hybrid propulsion system consists of an oxidiser tank, a solid fuel grain, a feed system to control the flow of oxidiser to the combustion chamber and a nozzle to convert the thermal energy into kinetic energy. In some cases a pressurant tank is included to maintain the oxidiser tank pressure. During operation, the pressure in the oxidiser tank drives the oxidiser flow to the combustion chamber where it is ignited with the vaporised fuel and then expelled out of the nozzle at high velocity.

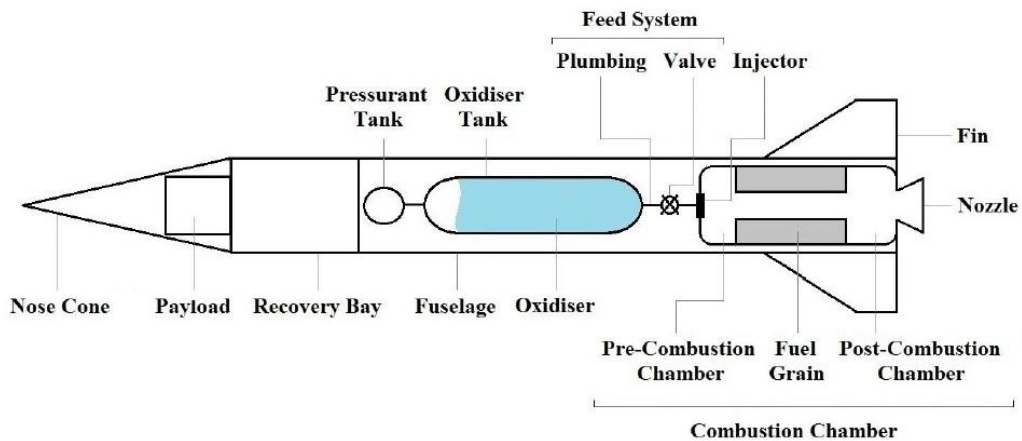


Figure 1.2: Hybrid rocket schematic (Leverone, 2013)

The fuel and oxidiser are kept apart and in different phases, resulting in a generally safer system as compared to the liquid and solid variants. For this reason, and because of lower costs, hybrid rockets have become popular among academic institutions seeking to develop sub-orbital

sounding rockets. The diffusion-based combustion present in hybrid rockets is tolerant of grain imperfections, unlike solid fuelled rocket motors where a single crack in the propellant grain can result in catastrophic failure. The main feed system valve allows for the flow of oxidiser to be controlled, and since the combustion process in a hybrid is dependent on oxidiser mass flow, the motor has the potential to be throttled. Due to simplicity and the non-hazardous nature of hybrid rockets, their cost of development is significantly lower than that of the liquid and solid variants. Nevertheless, hybrid rocket motors tend to suffer from lower combustion efficiency due to incomplete oxidiser and fuel mixing. As the motor burns, the fuel burning surface area increases which alters the operating oxidiser to fuel ratio (O/F ratio). This is known as the O/F shift and is detrimental to performance. The lower combustion efficiency coupled with the O/F shift result in a hybrid rocket motor having a relatively low energy density when compared to the liquid and solid variants.

1.1.2. Sounding rockets

High altitude sounding rockets are instrument-carrying vehicles with the purpose of conducting scientific research during flight. They provide a quick and relatively low-cost access to Earth's mesosphere and lower thermosphere (40 – 120 km) for astronomy, geophysics and microgravity experiments, and planetary probe development (Martin and Pfaff Jr., 2016). Sounding rockets also serve as a platform to test prototypes of components and subsystems that are intended for space launch vehicles and satellites (Indian Space Research Organisation, 2016). The sub-orbital flight trajectory of an unguided sounding rocket is characterised as a parabolic path allowing for a relatively long near-apogee duration, as depicted in Figure 1.3.

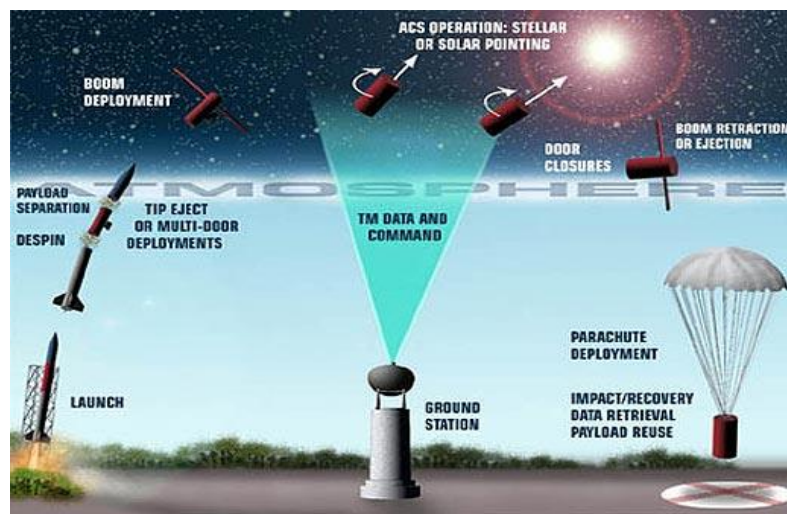


Figure 1.3: Sounding rocket flight trajectory and events (Marconi, 2016)

1.2. Phoenix history

To date, three postgraduate students have contributed to the development of the Phoenix Hybrid Sounding Rocket Programme (HSRP), namely Genevieve (2013), Chowdhury (2012) and Leverone (2013). Genevieve and Chowdhury worked on the programme's first hybrid sounding rocket (HSR), Phoenix-1A (P1A). This was a technical demonstrator and used to gain knowledge on hybrid rocket design, development and testing. Genevieve developed a hybrid rocket motor design and performance methodology in software form, while Chowdhury developed a six degree of freedom rocket flight simulator. These two codes can be used in conjunction with each other to design and optimise a hybrid rocket. The development of P1A started in 2010 with the design and manufacture of a lab scale motor (Brooks, et al., 2010). Data from the lab-scale testing was fed into the design of the P1A motor which suffered developmental delays due to multiple ignition failures. The P1A hybrid motor was successfully ignited in August 2013 with the flight test occurring in August 2014. Leverone (2013) developed the design for a 100 km apogee hybrid rocket that utilised the same propellant combination as P1A, that is, SASOL 0907 paraffin wax and nitrous oxide. The 11 m long rocket was named Phoenix-2A (P2A). This remained a design investigation and was never manufactured.

1.3. Phoenix-1B objectives

Following the P1A and P2A work, the next step in the programme was the development of an experimental hybrid rocket that could be launched on an ongoing basis to test new technologies. Phoenix-1B (P1B) requires that the cost of development be minimised and to aid in rapid development, the components should to be modular. This will enable select components to be amended without redesigning the entire rocket. The initial plan for the P1B series of rockets was to test-fly aluminised fuel grains which increase performance. To date, there has been limited research and testing of aluminised paraffin wax fuel grains, but these have the potential to substantially reduce rocket dead mass. The design of P1B must permit safe and controlled operation. In summary, the objectives of this study are to:

1. Provide a modular propulsion system design to aid in the progression of the Phoenix HSRP.
2. Improve the design, apogee and motor performance of P1A.
3. The new vehicle must be cost effective and have a reduced mass.
4. Improve the ground support system to ensure a specified mass of oxidiser is loaded into the flight tank as well as develop an oxidiser flow rate measurement capability.

1.4. Dissertation outline

In order to develop an effective design, the failures and shortfalls of P1A were analysed, thereby providing the initial design criteria and areas of focus for P1B. Chapter 2 briefly describes the P1A vehicle and associated problems that were encountered during the development and testing phases. This provided the author with a foundation on which to develop the current study.

A brief description of hybrid rocket operation is given in Chapter 3 with an explanation of the fuel grain regression rate parameter. This is a fundamental parameter in the design of hybrid rockets and directly affects performance. The operation of the hybrid rocket performance simulator (HYROPS) is discussed with reference to the design of P1B. The results of an investigation to determine the effect of aluminium loading in the fuel grain are also discussed. The procedural design of the P1B vehicle together with the final design and expected performance are then described.

Chapter 4 is dedicated to the design and analysis of the rocket motor's structural components, adhering to the specifications laid out in Chapter 3. The chapter addresses a proposed method for the oxidiser mass flow rate measurement, bulkhead retention methods and oxidiser loading.

One of the main reasons for the significantly lower than expected apogee of P1A was a nozzle failure, as described in Chapter 2. Chapter 5 includes the comprehensive re-design and analysis of a composite nozzle to ensure that weaknesses in the P1A motor are eliminated. Manufacturing of the P1B nozzle was undertaken by Rheinmetall Denel Munition who also provided design advice. A design methodology is described along with requirements and constraints. Chapter 5 also includes the results of transient thermo-structural analyses that were conducted to ensure that the nozzle can withstand the conditions encountered during a motor burn. The design objective of modularity required the structure of the nozzle to be designed for the most extreme case, being the operation of a 40% aluminised paraffin wax grain. Information from the study in Chapter 3 was used to develop a motor that utilised a 40% aluminium / 60% paraffin wax fuel and nitrous oxide. The specifications and performance of this new motor were determined, after which the thermo-structural analysis was undertaken.

Acoustic combustion instabilities were clearly audible during the hot fire test of P1A, as discussed in Chapter 2. To mitigate these for P1B, a brief review of combustion instability and the related influence of injector design is provided in Chapter 6. Multiple methods to characterise the two phase mass flow rate of nitrous oxide are discussed and are compared to two phase CFD results.

Even though this work is mainly focused on the P1B propulsion system, the aerodynamic design of the rocket airframe was also considered. Details of a glass fibre reinforce plastic (GFRP) nose cone and fin can are given in Chapter 7.

Chapter 8 provides a comparison between P1A and P1B, showing the improvements from the old to new. The final design and performance of the P1B HSR, as depicted in Figure 1.4, is presented. Lastly, the dissertation is concluded in Chapter 9 where a summary of the work is given together with recommendations for future improvements.



Figure 1.4: Phoenix-1B Hybrid Sounding Rocket

2. Phoenix-1B Design Criteria

2.1. Introduction

This chapter describes the design and testing of the P1A hybrid rocket and serves as a foundation for the design of P1B as described through the remainder of the dissertation. The P1A shortcomings are analysed so as to develop the initial design requirements and constraints for P1B. In doing so, an improved design was generated with an emphasis on cost-effectiveness, performance, modularity and reliability.

2.2. Phoenix-1A Hybrid Sounding Rocket

2.2.1. P1A vehicle design

P1A was developed by two postgraduate students in the UKZN Aerospace Systems Research Group (ASReG). Geneviève (2013) designed the hybrid propulsion system and Chowdhury (2012) worked on the aerodynamics and flight stability. This rocket formed part of the first phase of the UKZN Phoenix HSRP to gain experience in hybrid sounding rocket design, development and testing. Being a technical demonstrator, a conservative approach was taken during the design process to ensure operational safety. The vehicle used a paraffin wax (SASOL 0907 wax) fuel and nitrous oxide propellant combination. The rocket followed the conventional hybrid rocket layout with the liquid nitrous oxide stored in the oxidiser tank and the solid fuel grain being enclosed in the combustion chamber, as shown in Figure 2.1.

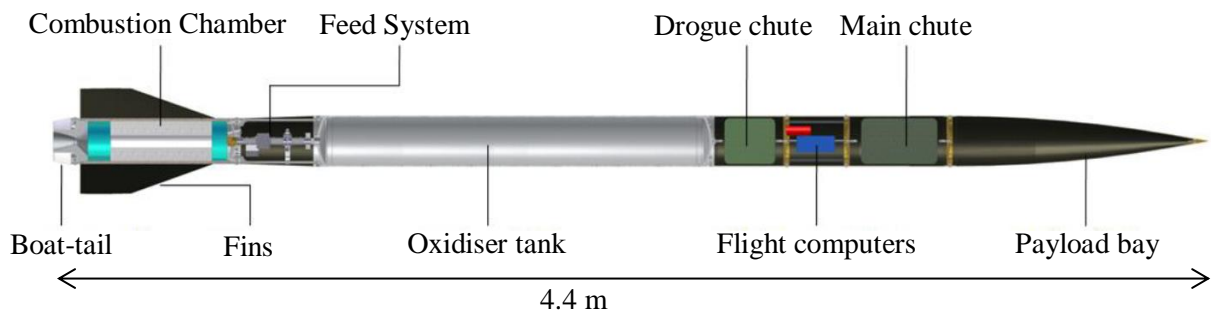


Figure 2.1: CAD rendition of P1A cross section (Chowdhury, 2012)

The propulsion system for P1A was designed to launch a 1 kg payload to 10 km in altitude. Vehicle design optimisation was achieved with the use of the hybrid rocket performance code (HRPC) (Genevieve, 2013) and HYROPS (Chowdhury, 2012). Tables 2.1 and 2.2 provide the vehicle's specifications and performance characteristics respectively.

Table 2.1: P1A vehicle specifications, adapted from Geneviève (2013) and Chowdhury (2012)

Section	Parameter	Unit	Specification
Combustion chamber	Propellant		SASOL 0907 Paraffin Wax
	Composition		97% Wax, 3% Charcoal
	Port Configuration		Single cylindrical
	Initial Port Diameter	m	0.05
	Grain Diameter	m	0.156
	Grain Length	m	0.4
	Combustion chamber length	m	0.66
	Combustion chamber diameter	m	0.18
Nozzle	Material		ATJ Graphite
	Type		Convergent-Divergent (CD)
	Shape		Bell-Shaped
	Expansion Ratio		5.99
	Throat Diameter	m	0.0298
	Exit Diameter	m	0.0731
	Nozzle length	m	0.134
Oxidiser tank	Oxidiser		Nitrous Oxide
	Supercharge Gas		Helium
	Design Oxidiser Mass	kg	30
	Design Supercharge Gas Mass	kg	0.006
	Tank Volume	m ³	0.043
	Ullage	%	10
	Initial Tank Pressure	bar	65
	Tank length	m	1.6
	Tank diameter	m	0.2
Aerostructure	Nose cone shape		Ogive
	Forward airframe length	m	1.9
	Forward airframe diameter	m	0.2
	Recovery		Dual parachute
	Material		Carbon fibre
	Deployment system		Carbon dioxide (pyrotechnic)
	Fins		Four clipped-delta plan form trapezoidal fins with hexagonal cross sectional aerofoil profile

Table 2.2: P1A vehicle performance, adapted from Geneviève (2013) and Chowdhury (2012)

Parameter	Unit	Specification
Design peak thrust	N	4250
Design O/F		6
Design combustion efficiency	%	95
Combustion chamber pressure	bar	40
Oxidiser mass flow rate	kg/s	1.34
Vacuum specific impulse	s	243
Total impulse	Ns	75 000
Design apogee altitude	m	15013
Maximum speed	m/s	571
Maximum acceleration	m/s ²	32.8
Ballistic flight time	s	126
Liquid burnout	s	19.8
Motor flame out	s	25

Commercially bought flight computers were installed to monitor the flight dynamics and control the parachute deployment events. A dual deployment setup was utilised with the drogue parachute deployed at apogee and the main parachute to be deployed at lower altitude. This was intended to limit the drift during decent and thus reduce the impact footprint.

2.2.2. P1A hot fire test and GSE

After a few failed hot fire attempts, mainly due to ignition problems (Genevieve, 2013), the hybrid propulsion system of P1A was successfully fired in August 2013. Figure 2.2 shows the P1A motor being tested on the Phoenix's Mobile Launch Platform (MLP). The MLP was designed to conduct rocket static testing as well as to launch hybrid rockets. Prior to launch and testing the rocket is fuelled with oxidiser from the supply tanks via a propellant distribution board (PDB). The PDB consists of valves and gauges to safely control the propellant flow and permit flight tank pressurisation. In the case of P1A, gaseous helium was used as a pressurant.

Fuelling and launch commands are sent remotely through an Ethernet cable from the host computer to the National Instruments (NI) CompactRIO installed on the MLP. The LabVIEW code features a graphical user interface (GUI) which permits systematic control of propellant loading and testing. Real-time data acquisition and display allows for system monitoring and recording of valuable measurements during tests.

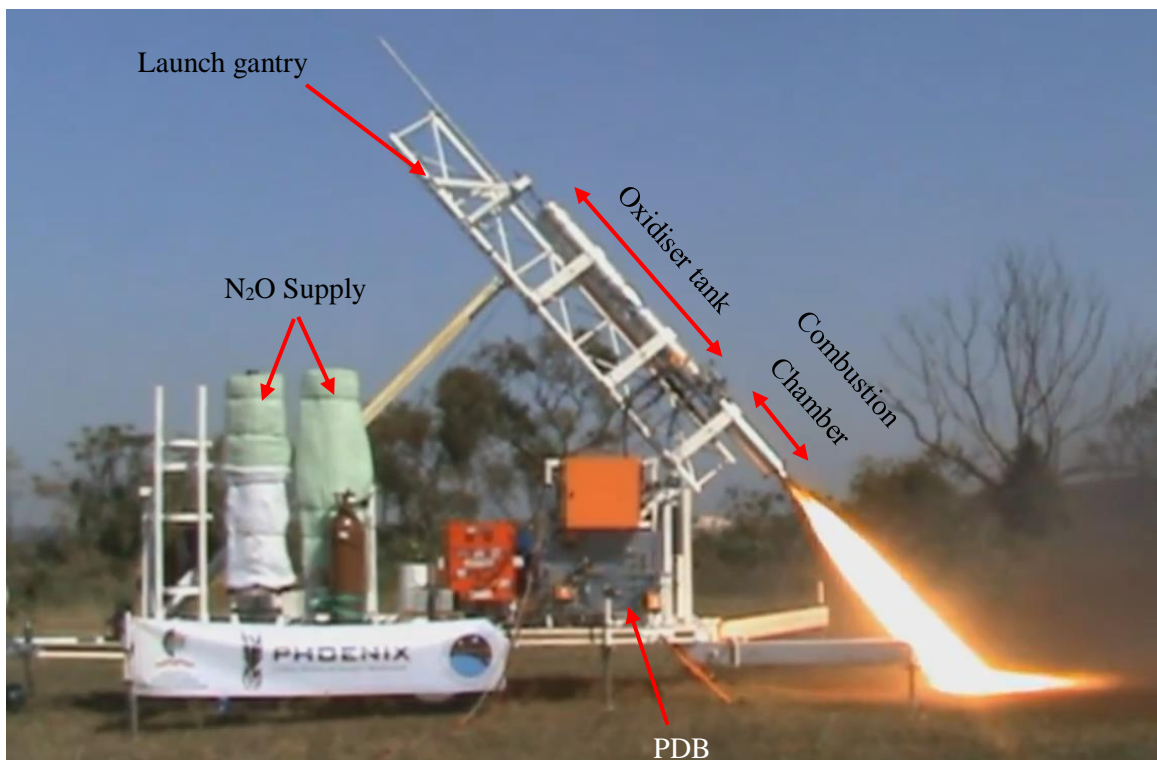


Figure 2.2: P1A Hot Fire Test on the MLP, adapted from ASReG UKZN (2013)

Successful ignition of the motor resulted in a peak thrust of 3250 N and a maximum combustion chamber pressure of 40 bar. The pressure and thrust time traces in Figure 2.3 are indicative of a hybrid motor operating with a blowdown system. That is, the oxidiser tank pressure decays as oxidiser is consumed. It is likely that a reduced oxidiser mass flow rate and lower combustion efficiency resulted in a reduction in the peak thrust. Having no accurate oxidiser mass flow rate measurement, this speculation could not be validated. High-frequency acoustic combustion instabilities were audible during the hot fire test. A video of this test is supplied in Appendix D.1. Combustion instabilities negatively affect combustion efficiency, thus reducing the thrust being generated (Sutton and Biblarz, 2001). The main cause was thought to be the conical injector (Figure 2.4) which reduces the hot gas re-circulation zone in the pre-combustion chamber. The hot gas re-circulation heats up the expanding nitrous oxide after the injector to promote oxidiser vaporisation (Sutton and Biblarz, 2001). The injector was changed to an axial design for the flight test. Chapter 6 includes a discussion of this phenomenon.

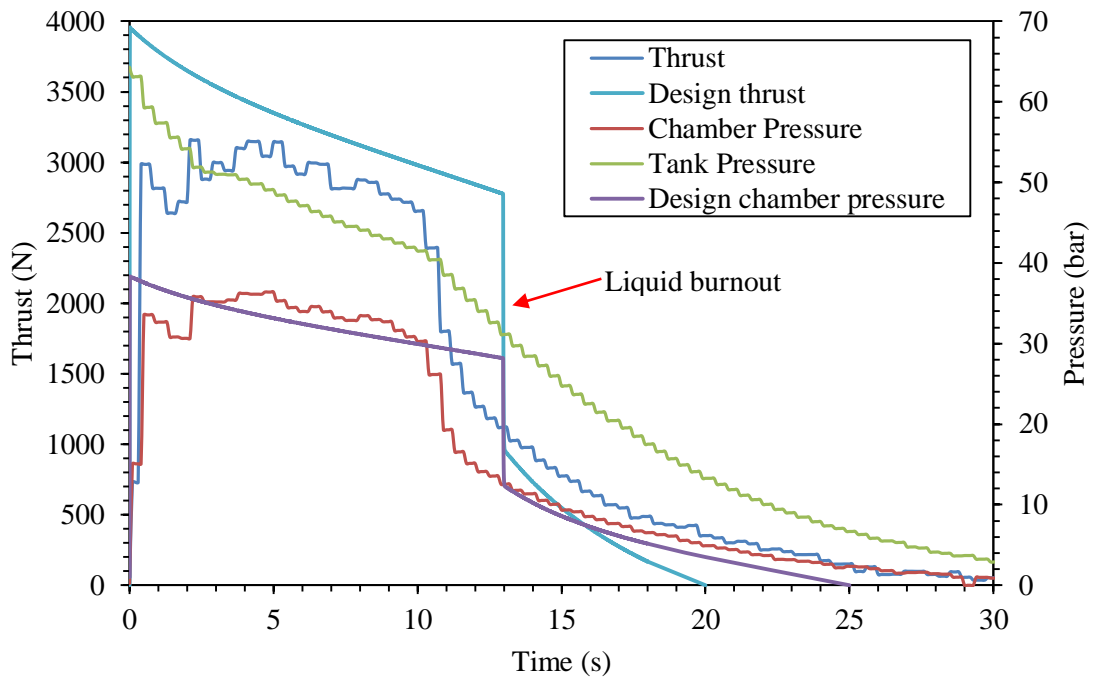


Figure 2.3: Comparison of P1A hot fire and theoretical design data

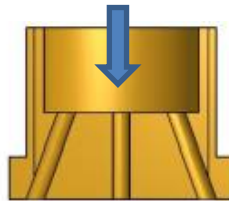


Figure 2.4: Conical injector used during P1A hot fire test (Genevieve, 2013)

Difficulties in transferring nitrous oxide to the flight tank on the MLP resulted in 20 kg being loaded instead of the design mass of 30 kg. Under-fuelling had a domino-effect of reducing burn time and increasing ullage volume which accelerated the pressure decay and reduced oxidiser mass flux. This hindered the diffusion combustion process (Balmogim, et al., 2015) and reduced total impulse to 40 kNs (Genevieve, et al., 2015). Modelling the flight trajectory of P1A with the hot fire test data showed that the vehicle would achieve an apogee of 6 km (Genevieve, et al., 2015) as opposed to the design apogee of 10 km. This was a direct consequence of under-fuelling and a lower than expected combustion efficiency.

2.2.3. P1A flight test

The technical demonstrator was launched in August 2014 from Denel's Overberg Test Range (OTR) in the Western Cape, South Africa. A myriad of trajectory tracking and monitoring instruments were utilised during the test flight. These included cintheodolites, infrared imagers, a C-band monopulse radar and a Weibel Doppler-based radar. Static high-speed cameras

(operating at 250 FPS) were located near the launch pad to capture motor ignition and movement on the launch rail (Genevieve, et al., 2015). The vehicle achieved a reduced apogee of 2.5 km which was due to under-fuelling and nozzle failure during lift-off. Recovery system failure resulted in the rocket's unfortunate destructive impact 55 s after launch. Successful spin stabilisation was achieved due to the 0.5° canted fins. This, coupled with the off-axis thrust generated from the nozzle burn through, caused the vehicle to 'cork-screw' during the powered phase of the flight (Appendix D.2). Figure 2.5(a) shows the fully assembled vehicle in launch position with the fuelling umbilical connected and Figure 2.5(b) shows the rocket leaving the launch pad. For safety reasons, the launch angle was limited to 75° causing a flattened flight path as seen in Figure 2.6.

Various events can be seen from the data and video footage supplied by OTR, as summarised in Table 2.3 and depicted in Figure 2.7. The 88 kg vehicle (lift-off mass) achieved a maximum velocity of 203.8 m/s and a peak acceleration of 30.3 m/s^2 . Impact occurred 4 km from the launch pad which resulted in the destruction of the vehicle and all onboard data storage. During ignition the rocket's main oxidiser valve (MOV) was first partially opened to 25%, this was to avoid igniter blow out and motor hard start. Due to the nature of hybrid motors, the pressure rises rapidly during ignition and then settles as the nozzle chokes. In some instances the pressure rises significantly which may cause structural damage and this is known as hard-starting.

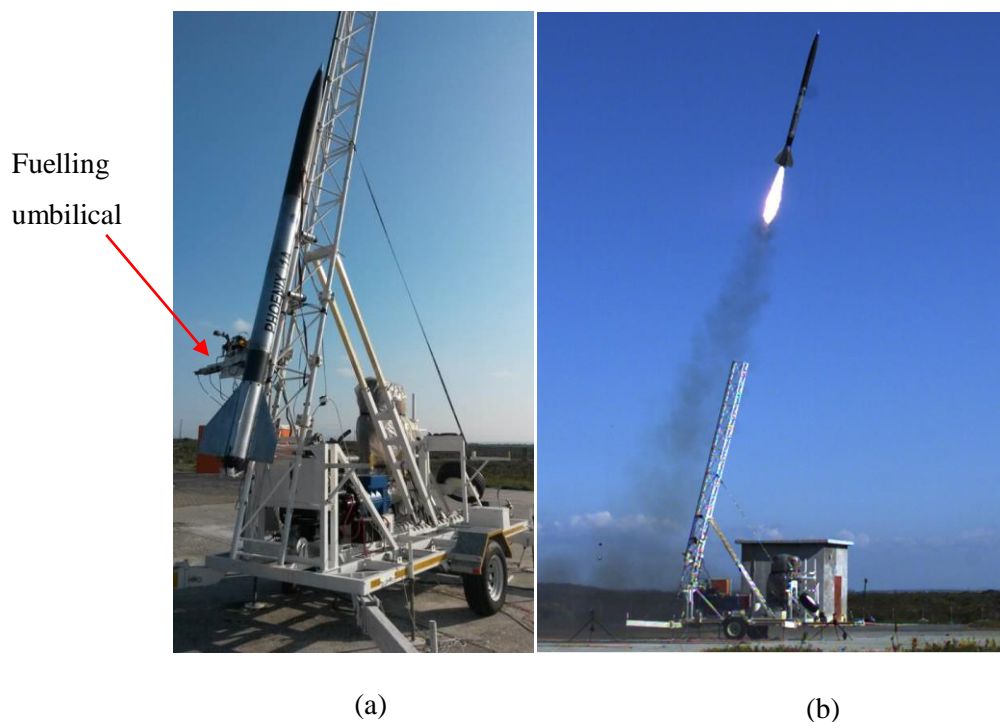


Figure 2.5: (a) P1A in launch position on MLP; (b) P1A leaving the launch pad at OTR (Genevieve, et al., 2015)

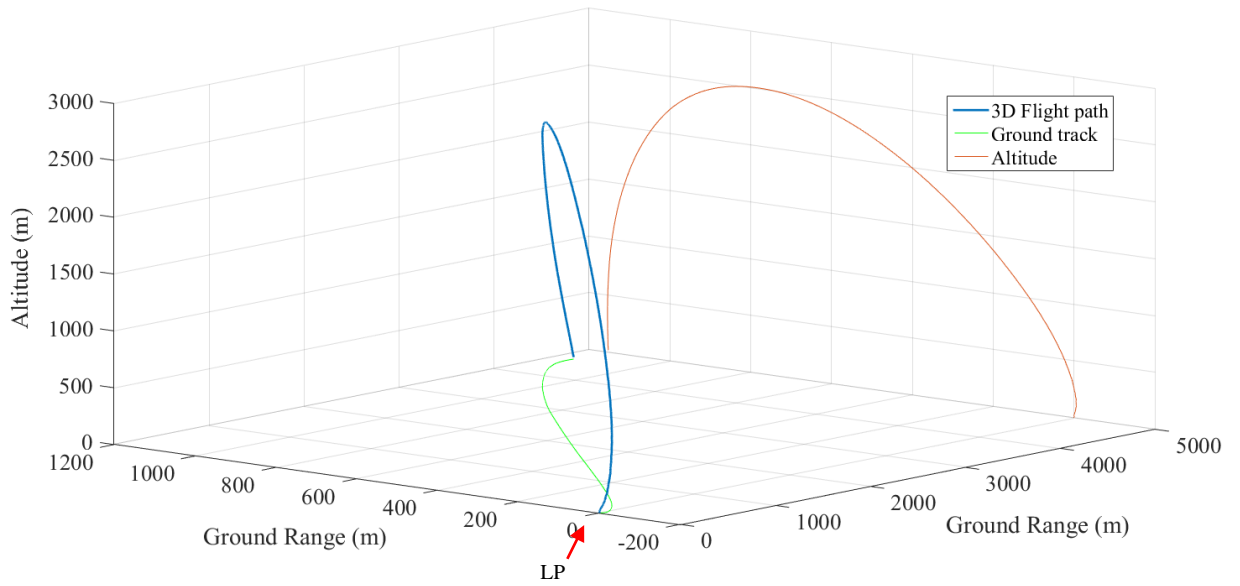


Figure 2.6: P1A flight path and trajectory

Table 2.3: P1A flight events

Time (s)	Event
T - 6	Ignition signal sent to pyrotechnic igniters
T - 2	MOV opened to 25%
T - 0	MOV fully opened; Lift-off
T + 10.9	Depletion of liquid nitrous oxide (liquid burn-out)
T + 18	Motor burn-out
T + 27.2	2.5 km apogee
T + 29	Drogue deployment and tether failure
T + 55	Impact

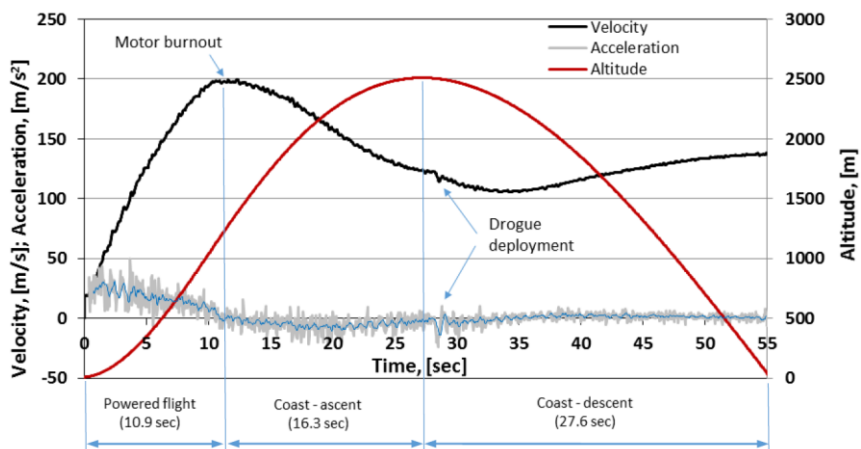


Figure 2.7: Flight dynamics of P1A (Genevieve, et al., 2015)

2.3. P1B design evolution

2.3.1. P1A cost and mass analysis

If P1B is to be launched on an ongoing basis the cost of production must be kept low. Analysing the cost and mass characteristics of P1A highlighted key areas that must be given attention in the new vehicle. For example, an area of concern was the increased P1A vehicle mass and cost that resulted from an overly conservative design with higher safety margins. The P1B vehicle must be designed with more realistic safety margins to decrease vehicle weight and expenditure (Balmogim, et al., 2015). Figure 2.8 illustrates the relative cost and mass distribution of the P1A vehicle. Fuel and oxidiser were not considered in these distributions. It can be seen that the vehicle mass and cost are sensitive to the airframe, oxidiser tank and combustion chamber components and these were of particular importance in cost-reduction efforts for P1B.

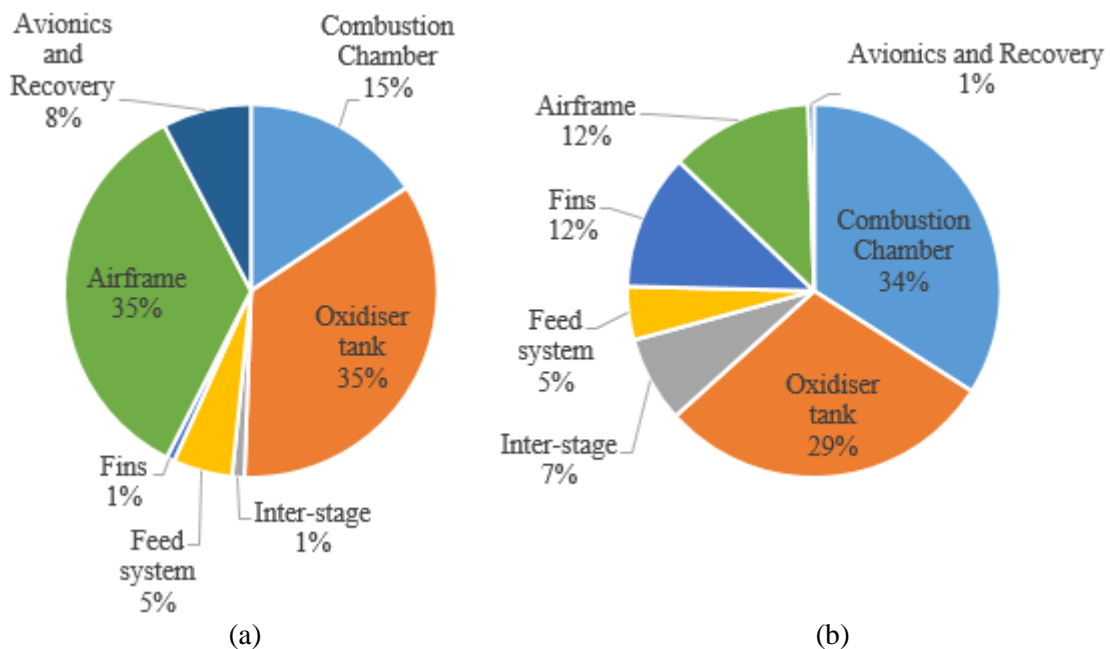


Figure 2.8: Relative cost (a) and mass (b) of P1A

2.3.2. Oxidiser tank

The 1.6 m long oxidiser tank was machined from two solid aluminium 6082-T6 billets to have an outer diameter of 200 mm. These were welded together with bulkheads on either end. A similar manufacturing process was used on the combustion chamber. The tank walls in weld areas were thickened to counteract the reduction in material strength due to the heat affected zone (Figure 2.9). This caused the tank to be inefficient due to the increased mass. The heat affected zone in aluminium welding causes localised stresses which deform the bulk material. This is illustrated in Figure 2.10 where bulging of the tank can be seen. A method of alleviating residual stresses is

to heat treat the component (Heston, 2009) but this is a costly process, especially for large components. For this reason it was decided to avoid aluminium welding for the P1B vehicle.

Sponsored aluminium 6061-T6 tubing was used for P1B to reduce the cost of manufacture for the P1A oxidiser tank. This tubing had an outer diameter of 164 mm, an inner diameter of 153 mm and a length of 2.4 m. The tubing dimensions limited and set the size constraints of the P1B oxidiser tank and combustion chamber, thus setting the calibre of P1B to 164 mm.

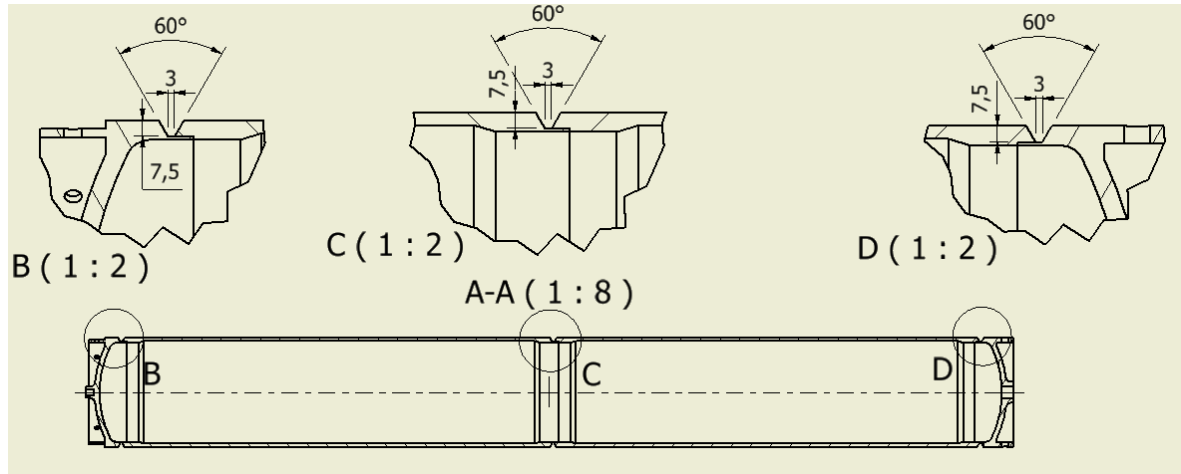


Figure 2.9: P1A oxidiser tank showing increased wall thickness (Chowdhury, 2012)



Figure 2.10: P1A interstage connecting the oxidiser tank to the combustion chamber (Balmogim, et al., 2015)

2.3.3. Airframe manufacture

The upper airframe of P1A consisted of sliding CFRP tubes that formed part of the parachute deployment system which contributed significantly to the cost of the airframe. The sliding of the

2 mm thick carbon fibre sections over each other posed a challenge to the manufacturing process and was outsourced. Extra layers of fibre were added and then machined away to attain a satisfactory sliding fit between sections. Figure 2.11 illustrates the parachute separation joints with the drogue being deployed first.

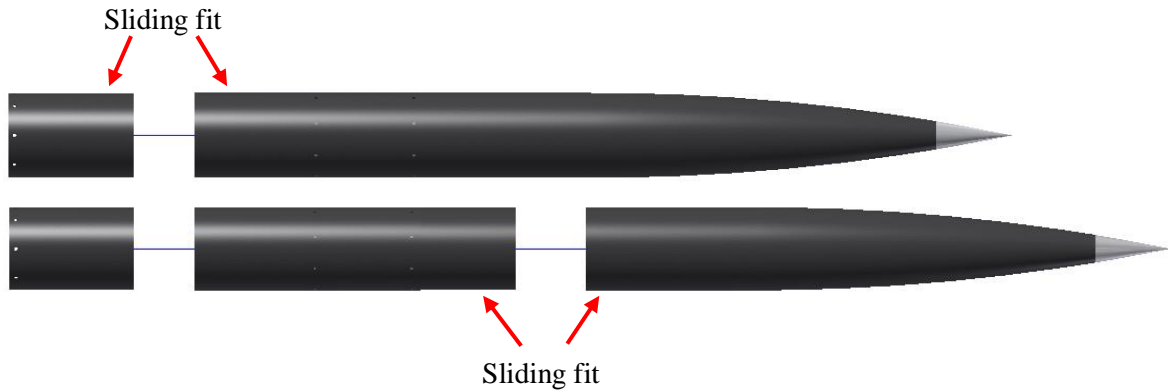


Figure 2.11: P1A upper airframe showing parachute separation, (top) drogue deployment, (bottom) main deployment

The manufacturing process for the upper airframe involved wrapping layers of resin pre-impregnated carbon fibre around a steel mandrel with the layup being compacted between each layer (Figure 2.12(a) and (b)). An out-of-autoclave technique of using heat shrink tape was used (Figure 2.12(c)). As the name suggests, the tape shrinks as it is heated thus providing positive pressure on the layup. This compacted the layers of fibre and ensured a high fibre volume fraction after curing. The layup was then machined to specified tolerances (Figure 2.12(d)). This process was found to be effective however it was time consuming and expensive and so to reduce costs for P1B, it was decided to move away from sliding fits on composite components and rather utilise fibre glass over carbon fibre.



(a)

(b)

Figure 2.12: (a) Fibre layup, (b) layer compaction with packaging tape



(c)

(d)

Figure 2.12 (cont.): (c) layup enclosed in heat shrink tape before oven curing, (d) cured layup being machined

2.3.4. Recovery system

Video evidence (Appendix D.2) from the tracking cameras showed a successful separation and drogue parachute deployment at apogee (Figure 2.13). Separation was achieved by puncturing carbon dioxide canisters with a pyrotechnic propelled piston. Unfortunately, the failure of the shock cord constraining the drogue parachute to the vehicle resulted in the destruction of the booster. Shearing of the shock cord was attributed to larger than expected aerodynamic loading on the drogue as a consequence of the flatter trajectory, with the rocket experiencing high lateral velocities (Genevieve, et al., 2015). The sheared kevlar shock cord is shown in Figure 2.14. A more reliable and resilient recovery system was needed for P1B. A higher launch angle would reduce the rocket's lateral speed at apogee and thus decrease aerodynamic loading on the parachutes. It must be noted that for safety concerns, the test range does not permit a launch angle of 90° without the installation of a flight certified self-destruct mechanism.

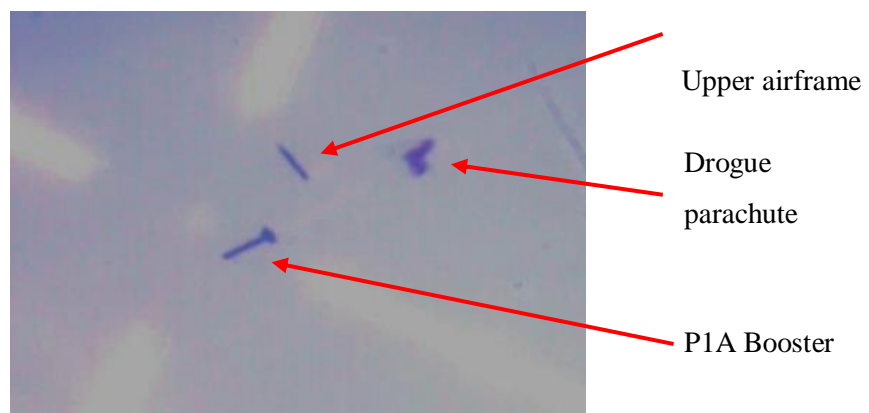


Figure 2.13: Drogue parachute deployment (Balmogim, et al., 2015)



Figure 2.13: Retrieval of shock cord from impact site

2.3.5. Nozzle failure

One of the main reasons for P1A's reduced apogee was the failure of the nozzle during launch. High speed footage showed the nozzle's graphite divergent section being ejected from the combustion chamber (Figure 2.15(b)) a few moments after ignition. The hot gases then caused the boat tail to be lost (Figure 2.15(c)). The exact reason for the nozzle failure was unknown, but it was speculated that this was a product of a hard start during ignition and a high stress concentration between the nozzle and nozzle retainer (Balmogim, et al., 2015) as depicted in Figure 2.16. The intentional gap between the graphite nozzle and stainless steel retainer was to allow for material expansion, but graphite is stronger in compression than tension (NASA, 1975) and so the failure was most likely caused as the graphite was loaded in the area of the stress concentration. This failure served as motivation for the rigorous design approach followed in this study for the P1B nozzle.

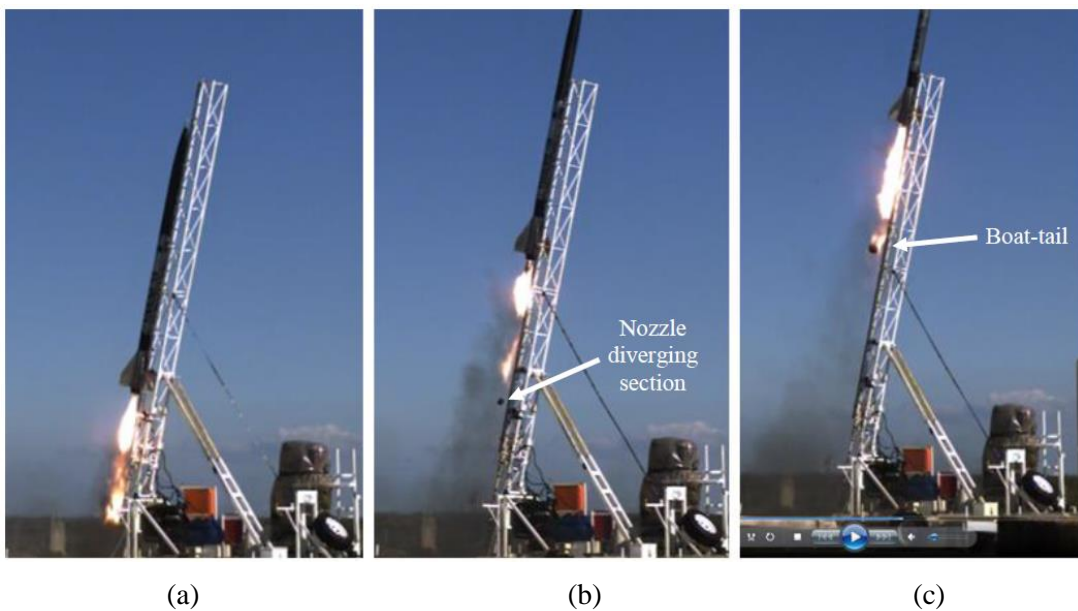


Figure 2.14: (a) Ignition and rocket movement, (b) nozzle failure, (c) boat tail ejection (Genevieve, et al., 2015)

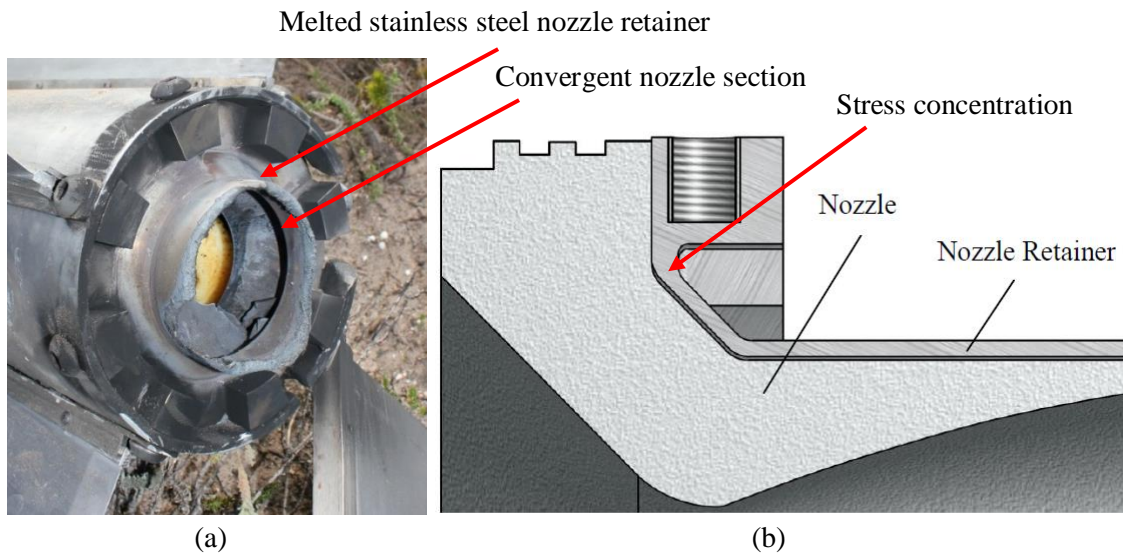


Figure 2.15: (a) Nozzle failure and remains of nozzle retainer showing burn through, (b) clearance between nozzle and nozzle retainer (adapted from Genevieve (2013))

2.3.5. GSE improvements

Vent system

Nitrous oxide under-fuelling was a significant contributor to the reduced P1A total impulse. To overcome this issue, a venting system became a necessary addition to the existing GSE and allowance for this was also to be made on the P1B vehicle. A vent system allows for control over the pressure differential between the supply and flight tanks and prevents the pressure equalising between the tanks as seen with P1A. Although the MLP has a pneumatic pump, this cannot overcome the build-up in nitrous oxide pressure beyond a certain point in the fuelling process. An additional valve and valve control system was therefore installed on the GSE, as well as a quick disconnect fitting to detach the vent line from the GSE to the rocket prior to launch.

Data acquisition

As mentioned in section 2.2.2, the oxidiser mass flow rate to the combustion chamber of P1A was unknown. A simple and cost-effective method to quantify the mass flow rate was required to accurately determine motor performance. This would allow for further analysis and optimisation of the propulsion system. The low sampling rate evident in Figure 2.3 was also addressed in this study to satisfy the Nyquist theorem which requires the sampling rate to be at least twice the operating frequency.

2.4. Summary

The design and operational shortcomings of P1A were used to inform the design of the P1B vehicle. The first hybrid rocket was designed to carry a 1 kg payload to a 10 km apogee and to achieve this the propulsion system was intended to generate a peak thrust of 4250 N over a 20 s liquid nitrous oxide burn period. Due to under-fuelling and lower combustion efficiency, the peak thrust was reduced to 3250 N during a ground-based hot fire test. Although the intended objectives of the P1A hybrid rocket were not achieved during the flight test, significant knowledge was gained. An analysis showed that the main areas of concern were the oxidiser tank, airframe manufacturing, recovery, nozzle design and alterations to the ground support equipment. The requirements and design criteria for P1B were thus established as follows:

1. A minimum safety factor of 1.5 should be used in the design of P1B in an attempt to reduce mass and cost.
2. Extruded aluminium tubing is preferred for the oxidiser tank and combustion chamber, setting the rocket outer diameter to 164 mm and tank length to 2.4 m.
3. Sliding composite tubing should be avoided and cheaper materials must be considered.
4. A more robust and reliable recovery system is required. Careful attention must be given to the selection of components to ensure structural integrity.
5. Intensive nozzle design and analysis is needed to avoid the failure that was experienced during the P1A launch. Nozzles are not to be re-used as in the case of P1A.
6. Design and implementation of a vent system is needed to fuel the flight vehicle to correct levels.
7. Development of a mass flow rate measurement system is necessary to ensure correct motor operation.

3. Phoenix-1B Hybrid Propulsion System Design

3.1. Introduction

This chapter briefly discusses the operation of hybrid rocket motors and the formulation of the fuel regression rate relationships. Procedural operation of the HYROPS software that was developed by Genevieve (2013) and Chowdhury (2012) is shown. This computational tool is extensively used throughout the dissertation. A study was conducted to establish the benefits and disadvantages of aluminised fuel and this showed that metallic additives increase the performance of a hybrid rocket motor while also reducing vehicle size and mass. However, aluminised fuel grains pose a challenge for nozzle design, which is addressed in Chapter 5, because of the raised combustion temperature and nozzle erosion. Using the HYROPS tool together with hybrid rocket theory and results from the aluminised fuel grain study, the design of the P1B hybrid rocket motor is developed and presented. The design specifications are used in Chapters 4, 5 and 6 to generate CAD models and conduct performance analyses.

3.2. Hybrid rocket internal ballistics

The firing of igniters inside the motor chamber initiates a chain reaction that starts the combustion process and ultimately generates thrust. During igniter firing, the generated heat vaporises the fuel and decomposes the incoming oxidiser. Igniter heat also supplies the activation energy to start the combustion reaction between the gaseous fuel and oxidiser. Upon successful fuel and oxidiser ignition, the injected oxidiser sets up a diffusion boundary layer on the fuel surface (Figure 3.1). Combustion is sustained until either the fuel depletes or oxidiser flow is halted. Gaseous fuel and oxidiser diffuse into the flame zone from the fuel rich zone below and oxidiser rich zone above. Vaporisation heat is supplied by the flame zone itself as shown in Figure 3.2.

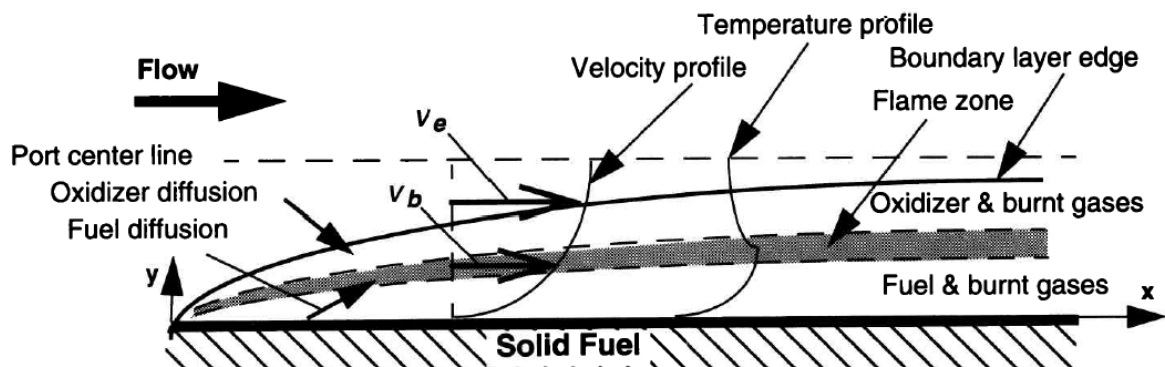


Figure 3.1: Diffusion layer combustion in a hybrid motor (Humble and Altman, 1995)

where \dot{Q} is the rate of heat transfer, k_g is the thermal conductivity of the gas in the flame zone, $\partial T/\partial y$ is the temperature gradient in the radial direction, α is the gas thermal diffusivity, ε_g is the emissivity of the flame sheet, σ is the Stefan-Boltzmann constant, T_f is the temperature of fuel grain, k_f is the fuel thermal conductivity, ρ_f is the fuel density, \dot{r} is the regression rate, h_g is the heat of fuel vaporization, ε_s is the emissivity of the fuel surface and T_s is the fuel grain surface temperature. Note that y is positive in the direction from the grain surface to the port centreline.

Radiation heat transfer can be neglected for non-metallised fuel grains (Zilliac and Karageyoglu, 2006), therefore the convective heat transfer into the fuel surface is equal to the conducted heat that causes phase change. The heat transfer for a classical hybrid motor is reduced to:

$$\dot{Q}_s = k_g \left. \frac{\partial T}{\partial y} \right|_{y=0^+} = \rho_f \dot{r} h_g \quad (3.3)$$

A shortcoming of this approach is that it does not account for the blocking effect whereby the vaporised fuel below the flame zone causes some resistance to the energy flow from the flame zone back to the fuel. Marxman et al. (1963) theorised an improved classical model that accounts for the diffusion flame with the boundary layer, the effects of conductive and convective heat transfer to the fuel and the blocking effect. The instantaneous local fuel regression rate is given by:

$$\dot{r} = \frac{0.036G}{\rho_f} \left(\frac{Gx}{\mu} \right)^{-0.2} \left(\frac{u_\infty}{u_c} \frac{\Delta h}{h_v} \right)^{0.23} \quad (3.4)$$

where G is the instantaneous local oxidiser mass flux, x is the distance along the port axis, u_∞/u_c is the velocity ratio of the gas in the main stream to velocity at the flame, $\Delta h/h_v$ is the ratio of the total enthalpy difference between the flame and fuel surface to the effective fuel heat of vaporisation, ρ_f is the fuel density and μ is the viscosity of the free stream (Zilliac and Karageyoglu, 2006). The product of the velocity and enthalpy ratios equates to the blowing factor (β) which represents the blocking effect (Sutton and Biblarz, 2001), yielding:

$$\dot{r} = \frac{0.036G^{0.8}}{\rho_f} \left(\frac{\mu}{x} \right)^{0.2} (\beta)^{0.23} \quad (3.5)$$

The model described in Equation (3.4) was developed for a slab fuel grain that was submerged in an oxidiser flow. This was not practical as hybrid rocket motors utilise cylindrical fuel grains and

so it was adjusted to contain coefficients and exponents that are derived from lab-scale testing. This augmented regression rate law is now standard practice in hybrid rocket development (Zilliack and Karageyoglu, 2006). The spatially and temporally averaged regression rate law is given by:

$$\bar{r} = a\bar{G}_{ox}^n \bar{x}^m \quad (3.6)$$

The coefficient ‘ a ’ and exponents ‘ n ’ and ‘ m ’ are propellant-dependent constants that are experimentally determined typically during lab-scale testing. Since it is easier to measure the oxidiser mass flow rate than the total mass flux, the equation is expressed as an average regression rate. Measurement of the mass flux is achieved by measuring the oxidiser mass flow rate and dividing it by the port cross sectional area. It must be noted that this relationship assumes that the regression rate is independent of the combustion pressure. Thus regression rate and consequently the fuel mass flow rate are dependent solely on the oxidiser mass flow rate. Generally the ballistic coefficient, m , is neglected as the regression rate is considered invariant with the fuel grain length and therefore constant. The functional form of the regression rate is then given as:

$$\bar{r} = a\bar{G}_{ox}^n \quad (3.7)$$

During lab-scale testing the regression rate and mass flow rate are measured. Plotting these data on a log-log graph with $\log \bar{r}$ on the y -axis and $\log G_{ox}$ on the x -axis, the ballistic coefficient and exponent can be calculated for a given propellant combination. The ballistic coefficient, a , represents the regression rate at unit oxidiser mass flux, that is the y -intercept. The ballistic exponent, n , is dependent of the on the propellant combination and is given by the gradient of the curve. Table 3.1 shows the ballistic coefficients for a few hybrid rocket propellant combinations and the calculated regression rate at an average oxidiser mass flux of 1000 kg/s.m².

Table 3.1: Ballistic coefficients and regression rate at an oxidiser mass flux of 1000 kg/s.m²

Fuel	Oxidiser	a	n	\bar{r} (mm/s)	Reference
Paraffin wax	LOX	0.117	0.62	8.48	(Karabeyoglu, 2012)
Hydroxyl-terminated polybutadiene	LOX	0.030	0.68	3.34	
High-density polyethylene	LOX	0.023	0.62	1.70	
Paraffin wax	N ₂ O	0.155	0.50	4.90	

Table 3.1 (cont.): Ballistic coefficients and regression rate at an oxidiser mass flux of 1000 kg/s.m²

40% aluminised paraffin wax	N ₂ O	0.175	0.50	5.53	(McCormick, et al., 2005)
High-density polyethylene	N ₂ O	0.104	0.35	1.17	(Lohner, et al., 2006)
Hydroxyl-terminated polybutadiene	N ₂ O	0.198	0.32	1.81	

The non-classical regression rate theory incorporates both the classical gasification process and the droplet entrainment mechanism. This applies to non-classical fuels such as paraffin wax and solid pentane that have a higher regression rate than classical fuels. An example of a classical grain is Hydroxyl-terminated polybutadiene (HTPB). The regression rate for a non-classical fuel grain is then given by the addition of the evaporative regression rate and entrainment regression rate due to the gasification and droplet entrainment mass transfer mechanisms respectively (Equation (3.8)) (Karabeyoglu, et al., 2002). The entrainment mechanism is depicted in Figure 3.3.

$$\dot{r} = \dot{r}_{entrained} + \dot{r}_v \quad (3.8)$$

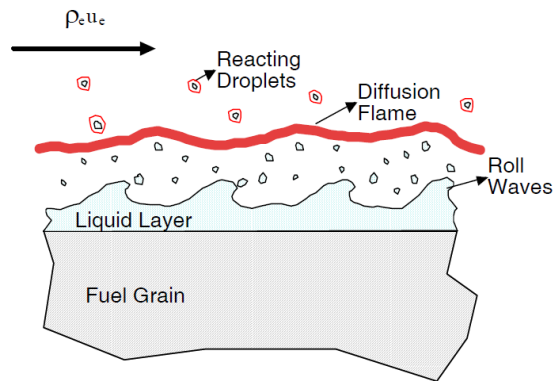


Figure 3.3: Entrainment mechanism in non-classical fuel grains showing roll waves (Karabeyoglu, 2012)

The propellant combinations for hybrid rocket motors are generally characterised by employing the empirical form of the Marxman equation (Equation 3.7) incorporating data derived from slab motor testing. For example, the regression rate of pure paraffin and nitrous oxide is given by:

$$\dot{r} = 0.155 \cdot G_{ox}^{0.5} \quad (3.9)$$

where \dot{r} and G_{ox} have the units of mm/s and kg/s.m², respectively. Hybrid rocket motor performance is commonly characterised by this form of the Marxman equation, which was used here in the design of the P1B hybrid motor.

The thrust, F , generated in a rocket is given by Equation (3.10) and consists of the momentum transferred from the high speed ejection of propellant and the pressure gradient across the nozzle exit. In a hybrid rocket motor the propellant mass flow rate (\dot{m}_{tot}) is the summation of the oxidiser (\dot{m}_{ox}) and fuel flow rates (\dot{m}_f) (Equation (3.11)). The fuel mass flow is generated during the burning process on the exposed grain surface area (A_b) in the port (Equation (3.12)). The amount of fuel liberated from the grain is governed by the regression rate which is in turn dependent on the oxidiser mass flow rate (Equation (3.13)). Equations (3.10) to (3.13) illustrate the direct dependence of thrust on regression rate, indicating the significance of this parameter in the design of a hybrid rocket motor.

$$F = \dot{m}_{tot}u_e + (p_e - p_a)A_e \quad (3.10)$$

$$\dot{m}_{tot} = \dot{m}_{ox} + \dot{m}_f \quad (3.11)$$

$$\dot{m}_f = \rho_f A_b \dot{r} \quad (3.12)$$

$$\dot{r} = aG_{ox}^n = a \left(\frac{4 \dot{m}_{ox}}{\pi D_p^2} \right)^n \quad (3.13)$$

3.3 Design and simulation programs

The hybrid rocket performance simulator (HYROPS) is a software tool developed for the Phoenix HSRP to aid in the design and analysis of hybrid rockets. This program consists of the Hybrid Rocket Performance Code (HRPC) and a 6 DOF flight dynamics simulator. The program model is shown in Figure 3.4. HRPC focuses primarily on motor design and performance whereas the dynamics simulator focuses on trajectory and flight dynamics modelling. These functions are used in the iterative design and performance analysis of the P1B vehicle such that the intended apogee is reached. HYROPS also has the ability to produce impact footprints with its Monte Carlo probability analysis which is a requirement for flight testing at test facilities such as the Overberg Test Range (OTR). The test range evaluates the results of this analysis to ensure the safety of personnel and equipment within and around the test range.

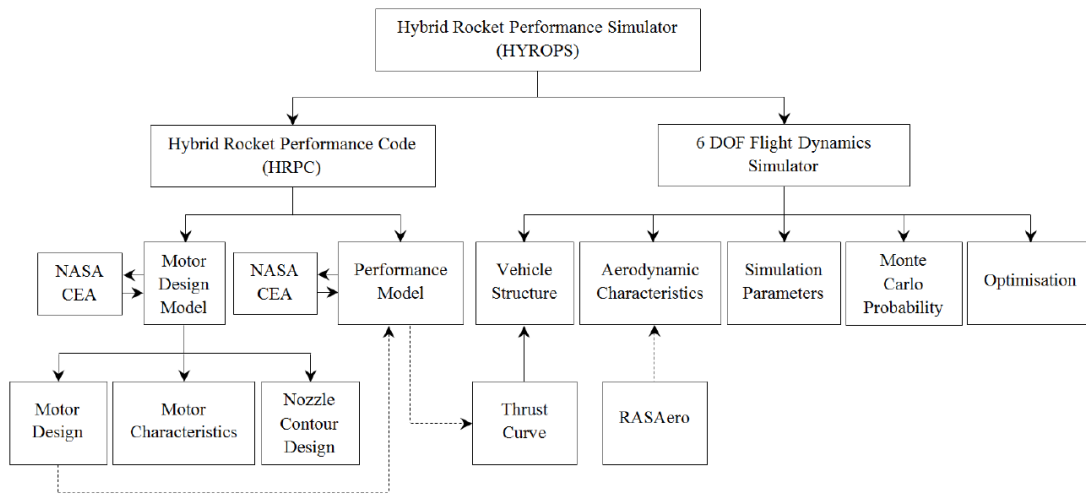


Figure 3.4: Hierarchy model of HYROPS (Leverone, 2013).

3.3.1. Hybrid rocket performance code

HRPC comprises of two models namely the motor design model and the performance model. Both of these make extensive use of the NASA CEA thermochemistry program (Gordon and McBride, 1994) and its rocket application module. Genevieve (2013) gives a comprehensive description of this code.

The HRPC motor design model provides motor dimensions and characteristics from steady state calculations. This model is further broken into three sub-models. Figure 3.5 illustrates the inputs and outputs of each sub model which can be executed separately. The suggested order of execution of the sub-models to completely characterise a hybrid motor is (2), (1) and then (3). The motor characteristics model outputs a wide range of operating parameters for varying O/F ratio and combustion chamber pressure. These are presented graphically to allow for optimum specifications to be selected and fed into sub-model (1). The motor design model yields fuel grain and nozzle dimensions which are fed into sub-model (3) for nozzle contour design and specifications.

Once the motor design has been fully characterised, the specifications are transferred to the performance model shown in Figure 3.6. This model conducts a comprehensive transient analysis on the motor design. A 4th-order Runge-Kutta (RK4) method is employed to solve the transient differential equations that govern hybrid rocket operation. A database of thermochemistry properties is first generated by repeatedly querying NASA CEA with a different O/F ratio and combustion pressure on each run. A look-up table is then used by the numerical solver to simulate a motor firing for which an oxidiser feed method must be selected. A list of oxidiser feed options

are provided in Figure 3.6. The blowdown model was employed for all simulations in this dissertation as this represents the oxidiser tank pressure decay during operation and the flow method that is used on P1B.

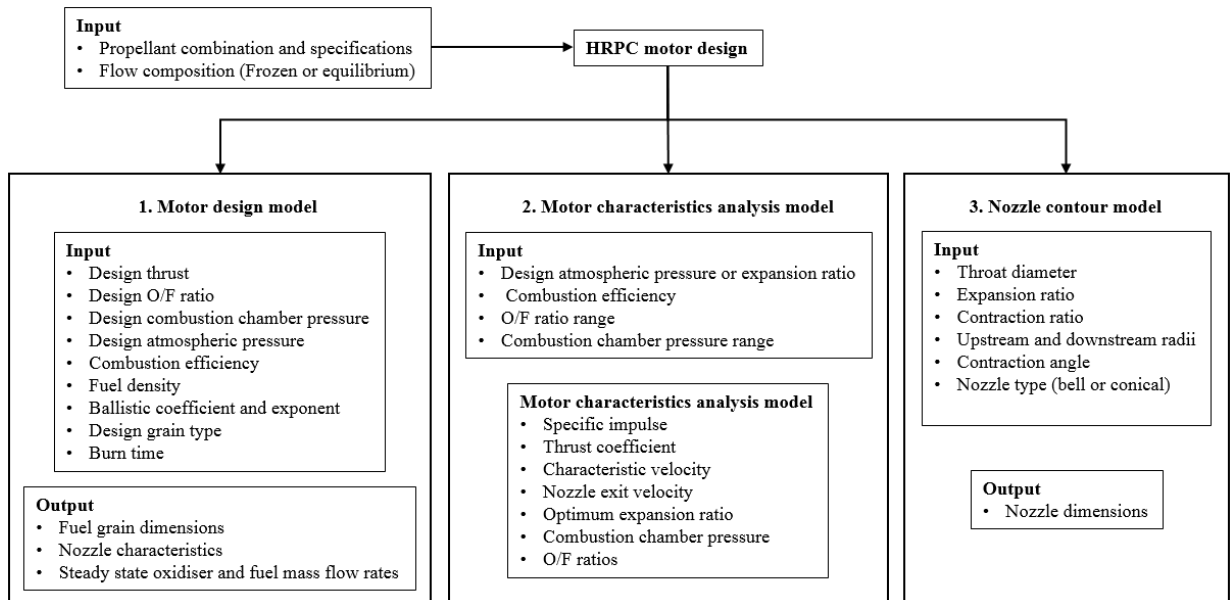


Figure 3.5: HRPC motor design

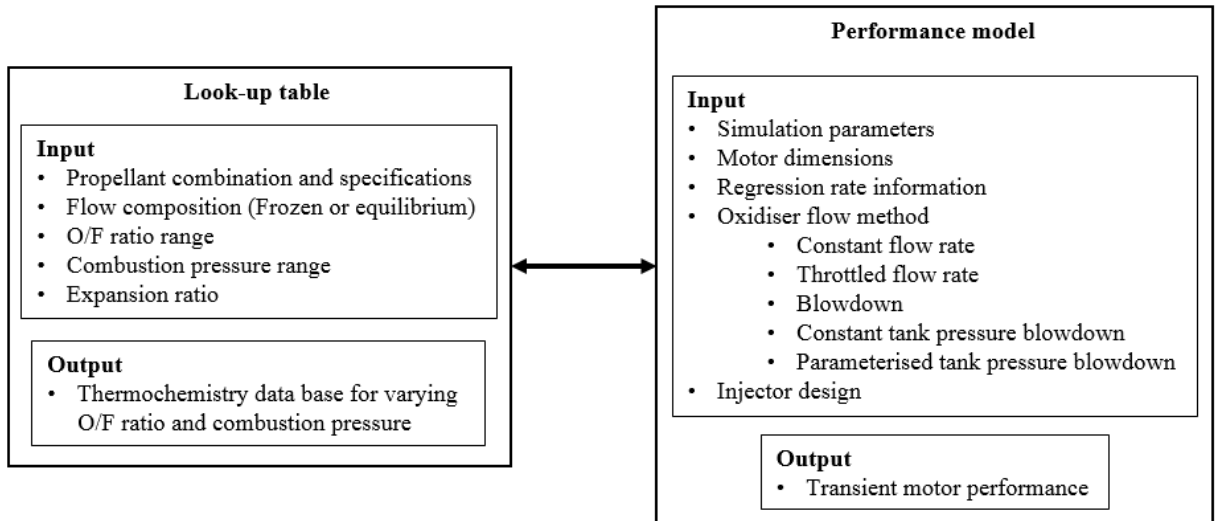


Figure 3.6: Hybrid rocket performance simulator

3.3.2. 6 DOF flight dynamics simulator

The HYROPS flight dynamics simulator has the capability to simulate and display rocket flight trajectories. Therefore the use of this tool in conjunction with HRPC can enable the optimisation of a hybrid rocket design. The program also utilises the RK4 numerical solver for the kinematic

and Newtonian equations of motion to predict rocket flight path and dynamics. Options are available to include wind variation and parachute deployment. A unique feature of the program is the Monte Carlo probability analysis that permits variations in certain parameters and simulates multiple trajectories. The process is repeated autonomously to generate a statistical impact footprint which is a crucial safety requirement when launching high altitude rockets. The program also analyses the rocket's stability during flight, from which adjustments can then be made to the design to ensure that the location of the centre of pressure along the rocket axis is between one and two calibres behind the centre of mass. Figure 3.7 shows the start-up screen and associated controls for vehicle design, simulation parameters, wind parameters, launch parameters and Monte Carlo analysis. Chowdhury (2012) provides a detailed description and development of the flight simulator.

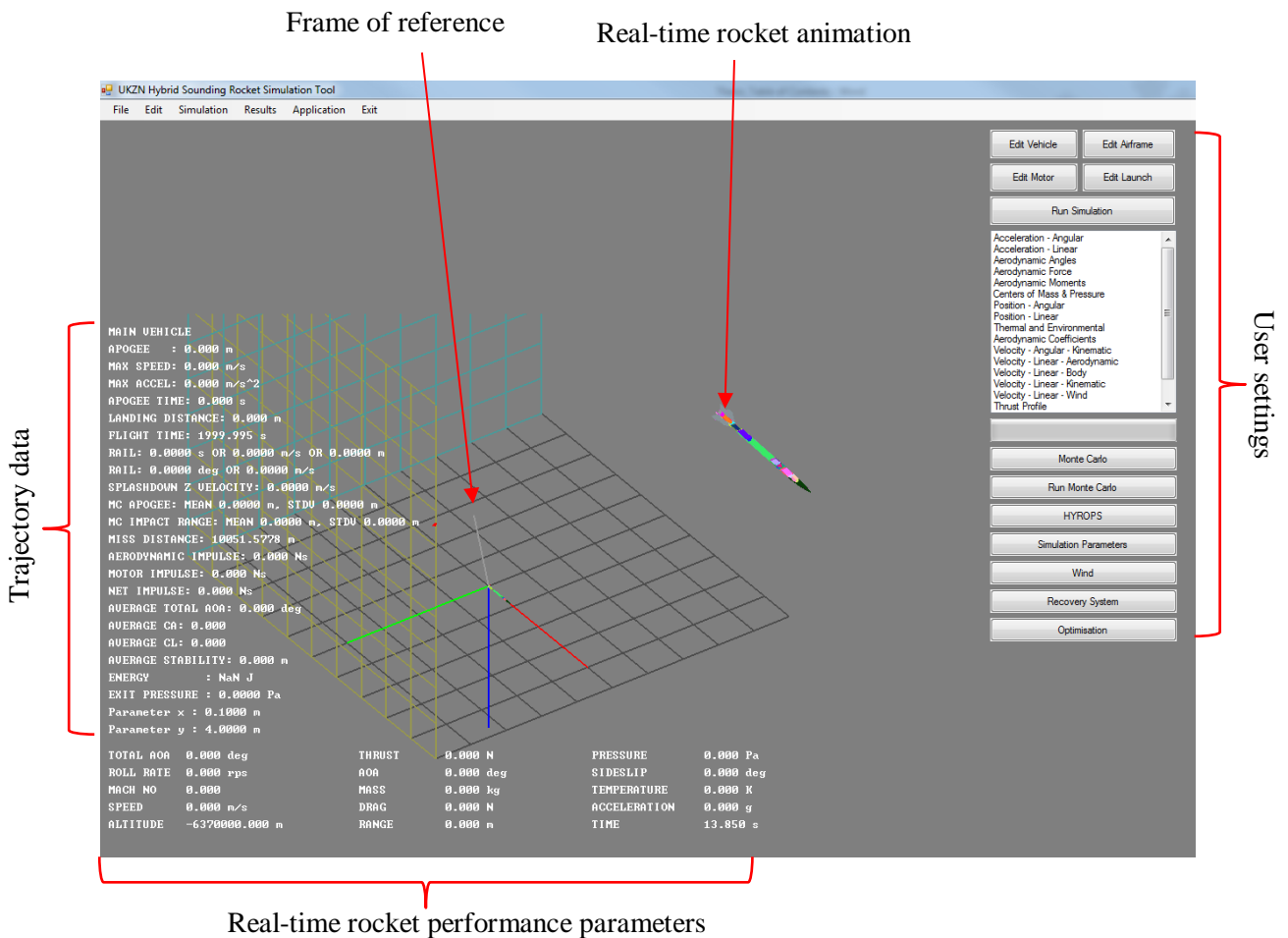


Figure 3.7: Start up GUI of HYROPS

3.4. Aluminium loading effects study

3.4.1. Aim and methodology of study

Aluminising paraffin wax in hybrid rockets decreases the oxidiser to fuel ratio and increases the fuel regression rate, however flame temperature rises with aluminium loading. Metalising a fuel grain increases radiative heat transfer across the diffusion boundary layer, vaporising more fuel and increasing regression rate, as seen in Equation (3.1). This part of the study investigates the effects of varying the aluminium loading from 10% to 50% (by mass) on motor design, performance characteristics and the evolution of aluminium oxide (alumina).

The methodology adopted here is described in Figure 3.8. P1A was designed to have a total impulse of 75 kNs and was set as the basis of the investigation so as to provide a quantitative comparison between analysis results and the P1A vehicle. Burn time in a hybrid rocket is predominantly determined by the outer diameter of the fuel grain therefore an initial assumption of 12 s was made for aluminised fuel, which, together with the total impulse, yields a design thrust of 6250 N. A port diameter of 60 mm was chosen based on a ratio of outer diameter (OD) to port diameter of between two and three (Karp, 2012). A physical constraint set the maximum OD of the grain to 147 mm. For comparison purposes a baseline fuel grain mass was found for a pure paraffin wax motor and kept constant. The burn time was established using the fuel mass flow rate from HRPC and the baseline fuel grain mass. Due to the lack of information on the regression rate coefficients and densities for the different aluminium loadings, linear interpolation was used between the pure wax data and 40% aluminium (by mass) data. Pure paraffin wax data were retrieved from Genevieve (2013) and 40% aluminised wax data was obtained from McCormick et al. (2005), with the results being shown in Figure 3.9. An assumption was made to keep the ballistic exponent, n , at a constant value of 0.5. This was presumed to be acceptable due paraffin wax being the predominant fuel and nitrous oxide being the oxidiser in all cases.

Combustion information and rocket performance metrics were calculated at various O/F ratios for different aluminium loadings using HRPC and NASA CEA. The optimal O/F ratio was chosen based on peak characteristic velocity (C^*), which is a measure of combustion chamber performance. C^* is defined by:

$$C^* = \frac{P_0 A_t}{\dot{m}_{tot}} \quad (3.14)$$

where P_0 is the combustion chamber pressure, A_t is the nozzle throat cross sectional area and \dot{m}_{tot} is the total propellant mass flow rate. The corresponding peak chamber temperature was then found from the optimal O/F ratio and data from HRPC and NASA CEA. Lower combustion efficiency is a problem with hybrid rockets therefore the C^* value from NASA CEA was adjusted in HRPC to take into account an efficiency of 90% (Dyer et al., 2007). The mass of the oxidiser system is the sum of the masses of the nitrous oxide and the oxidiser tank including 10% ullage and two bulkheads, weighing 1 kg each. Utilizing the optimal O/F ratio and the constant fuel grain mass, the mass of oxidiser required was calculated. The corresponding tank length and mass were then found. The results of this analysis are given in the following section.

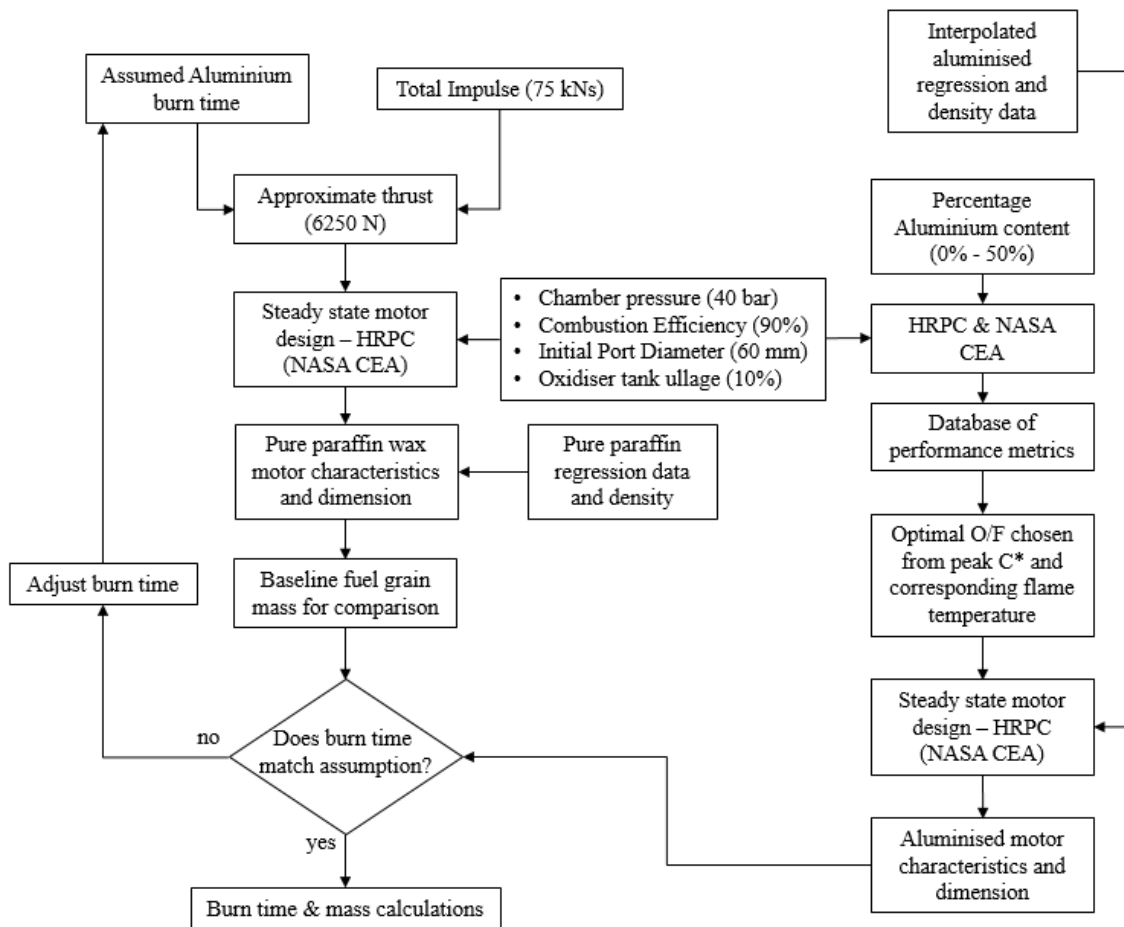


Figure 3.8: Methodology for aluminised fuel grain study

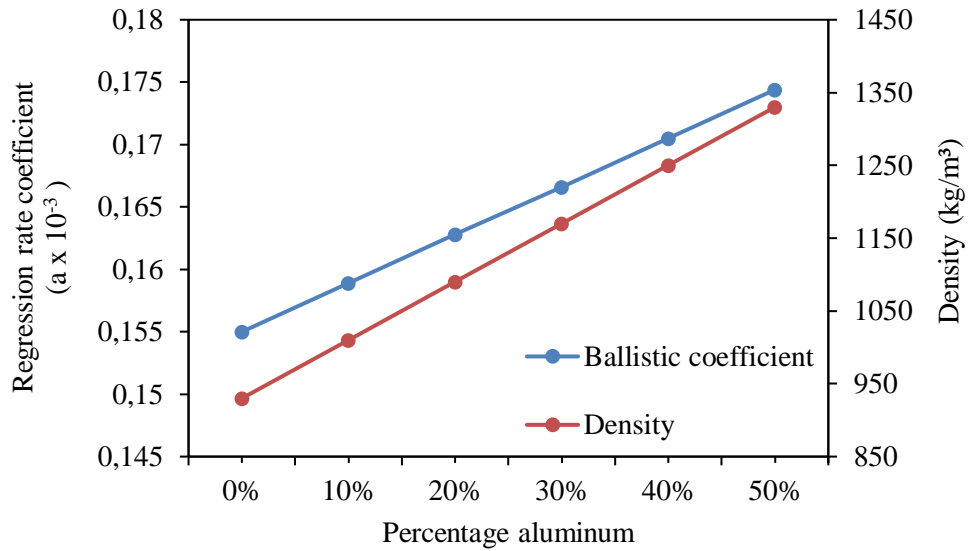


Figure 3.9: Interpolated regression rate coefficient and density data

3.4.2. Effect of metallisation on hybrid motor design and performance

Optimal O/F ratio values were established from the peak characteristic velocity curves shown in Figure 3.10. Tables 3.2 to 3.4 show the effect of aluminium loading on performance metrics, booster mass and booster length respectively. As seen in Figure 3.10 the optimal O/F ratio decreases with increasing aluminium loading. There is also an increase in C^* with increasing aluminium loading, but it is not a significant change. The critical difference is the reduction in the O/F ratio which results in a higher overall propellant density and a smaller propulsion system. This can be shown explicitly by looking at the density specific impulse (Gordon, 1962) shown in Figure 3.11. Density specific impulse is calculated according to Equation (3.15) and is defined as the product of the fuel density (ρ_f) and specific impulse (I_{sp}) of the hybrid motor.

$$I_{density} = I_{sp} \cdot \rho_f \quad (3.15)$$

A common trait of hybrid rocket motors is the O/F shift, where the O/F ratio decreases during operation causing combustion to become fuel rich. This manifests as a movement away from peak C^* , traversing the curves in Figure 3.10 to the left, and thus impeding motor performance during operation.

Burn time decreases with increasing aluminium loading due to the increased fuel mass flow rate for the same fuel grain mass as seen in Table 3.2. The mass of the oxidiser decreases due to the decreased O/F ratio and this in turn decreases the length and mass of the oxidiser tank. As a whole, the oxidiser system mass decreases significantly with increasing aluminium loading. Comparing

these results to that of P1A, it can be seen in Figure 3.12 that the length and mass of the vehicle decreases from 3.03 m for pure paraffin (similar to that of P1A) to 1.51 m for a 50% aluminised fuel grain.

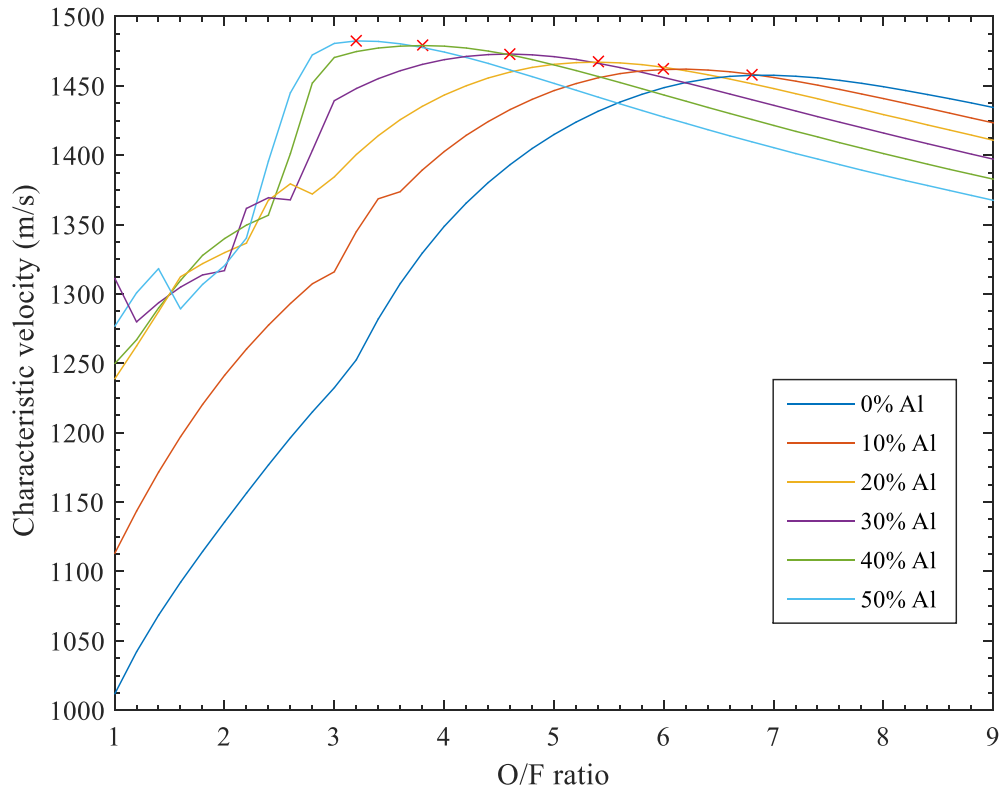


Figure 3.10: C^* variation with O/F ratio for different aluminium loadings

Table 3.2: Effect of aluminium loading on motor performance

Aluminium loading by mass (%)	Opt O/F	C^* HRPC (m/s)	Specific impulse (s)	Temp. at optimal C^* (K)	Total fuel flow rate (kg/s)	Density specific impulse ($\times 10^5$) (kg.s/m ³)	Burn time (s)
0	6.8	1457.59	225.13	3310.3	0.363	2.09	13.78
10	6	1461.72	226.14	3352.6	0.403	2.28	12.42
20	5.4	1467.09	227.88	3427.9	0.437	2.48	11.45
30	4.6	1472.95	229.26	3496.4	0.496	2.68	10.08
40	3.8	1479.05	230.72	3572.4	0.575	2.88	8.69
50	3.2	1482.38	232.09	3674.7	0.654	3.09	7.65

Table 3.3: Effect of aluminium loading on booster mass

Aluminium loading by mass (%)	Grain mass (kg)	Mass of combustion chamber casing (kg)	Mass of ox (kg)	Mass of ox tank (kg)	Mass of ox system (kg)	Mass of chamber (kg)	Booster mass (kg)	Decrease in Ox system from pure wax (kg)
0	5	2.06	34	19.59	53.59	7.06	60.65	0.00
10	5	1.90	30	17.28	47.28	6.90	54.18	6.30
20	5	1.76	27	15.55	42.55	6.76	49.31	11.03
30	5	1.64	23	13.25	36.25	6.64	42.89	17.34
40	5	1.54	19	10.95	29.95	6.54	36.48	23.64
50	5	1.44	16	9.22	25.22	6.44	31.66	28.37

Table 3.4: Effect of aluminium loading on booster dimensions

Aluminium loading by mass (%)	Throat diameter (mm)	Fuel grain length (m)	Tank length, Incl. 10% ullage (m)	Length of booster (m)	Decrease in tank length from pure wax (m)
0	36.24	0.380	2.65	3.03	0.00
10	36.21	0.350	2.34	2.69	0.31
20	36.13	0.324	2.10	2.43	0.55
30	36.1	0.302	1.79	2.09	0.86
40	36.06	0.283	1.48	1.76	1.17
50	36	0.266	1.25	1.51	1.40

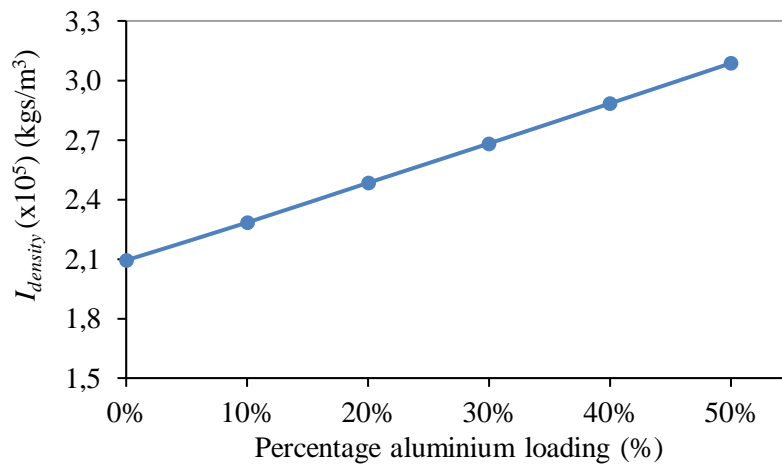


Figure 3.11: Increase in density specific impulse with increasing aluminium loading

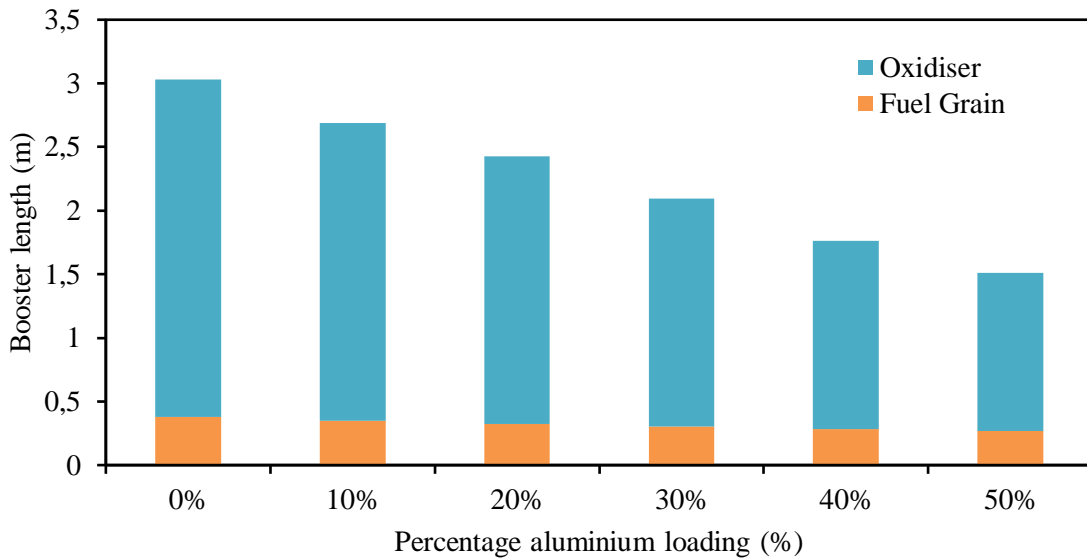


Figure 3.12: Booster length reduction with increasing aluminium loading (Balmogim, et al., 2015)

3.4.3. Effect on nozzle

Three main factors influence nozzle erosion, namely, oxidisation due to heterogeneous chemical reactions, mechanical impingement, and melting of nozzle material (NASA, 1975). The main concern for this study is mechanical impingement. Alumina particles are dense ($\sim 3950 \text{ kg/m}^3$) and thus particle impingement is the main contributor of mechanical erosion in aluminised rocket motors. An investigation was undertaken to compare the amount of alumina produced in the nozzle for the different aluminium loadings, paying specific attention to phase. Figure 3.13 shows a graph of flame temperature versus O/F ratio, where the temperature corresponding to optimal O/F is denoted with an 'x'. As the aluminium loading is increased the flame temperature increases significantly. It is noted that the flame temperature is significantly higher than the melting temperature of alumina ($\sim 2345 \text{ K}$), even with a decrease in temperature during the burn.

Increasing the aluminium loading will increase the amount of alumina produced and this will increase the erosion at the throat. Liquid particle erosion is not as significant as solid particle erosion (Thakre, et al., 2013). Figures 3.14 and 3.15 show the mole fraction of liquid phase alumina and solid phase alumina respectively in the nozzle. It should be noted that this analysis is based on the assumption of complete combustion of the aluminium before the nozzle. It is seen that there is primarily liquid phase alumina in the convergent section of the nozzle, due to the high flame temperature as described in Figure 3.13. As the expanding exhaust gas cools in the nozzle (Figure 3.16), solid alumina particles start to form in the divergent section. This can be

seen as the mole fraction of the liquid phase decreases and that of the solid phase increases through the divergent section. In the case of 50% aluminium, liquid phase alumina exists throughout the nozzle with a relatively small production of solid alumina particles in the divergent section compared to 30% and 40% aluminium loading. This is due to the significantly higher flame temperature. Since nitrous oxide is delivered to the combustion chamber via a blowdown process, the oxidiser tank pressure decreases with time and this also decreases the combustion chamber pressure. As nozzle throat erosion is heavily dependent on combustion chamber pressure, throat erosion should theoretically decrease as the chamber pressure declines.

The second cause of nozzle erosion is the chemical reactions between the exhaust gas and nozzle material. Oxygen-containing combustion products such as water, hydroxyl groups and carbon dioxide, among others, oxidise the nozzle material in the high temperature environment. With this in mind, an investigation was undertaken to quantify the amount of oxidising species in the gas flow. Again, this analysis assumes complete aluminium combustion. Figures 3.17 (a) to (e) show the relative molar fraction of the predominate oxidising species in the nozzle for varying aluminium content. For comparison, the alumina molar fraction is also depicted (AL₂O₃ (a) and AL₂O₃ (L) refer to solid and liquid alumina respectively).

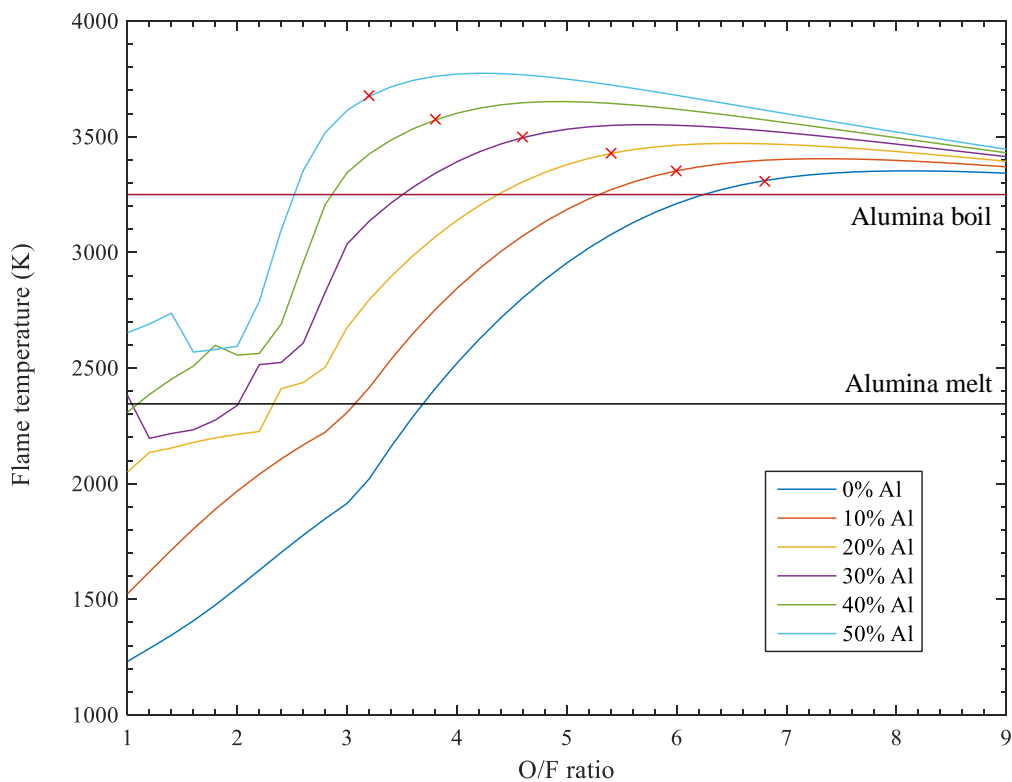


Figure 3.13: Combustion temperature variation for different aluminium loadings

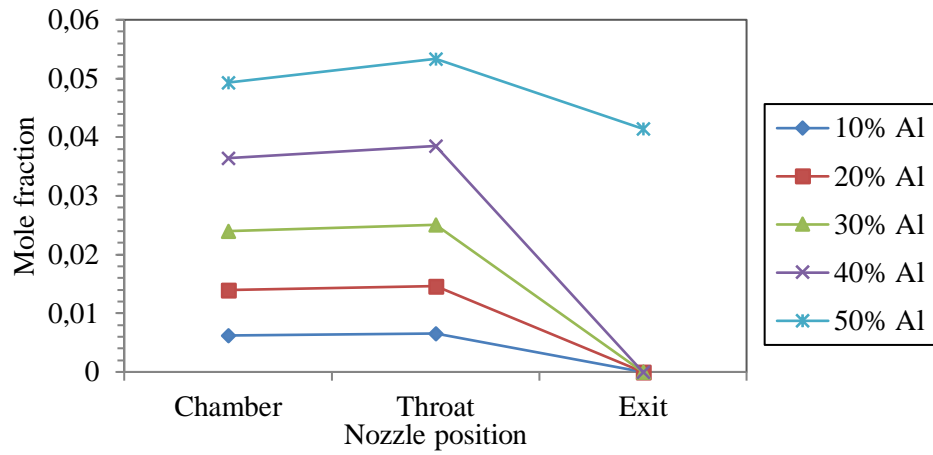


Figure 3.14: Mole Fraction of liquid phase alumina in nozzle

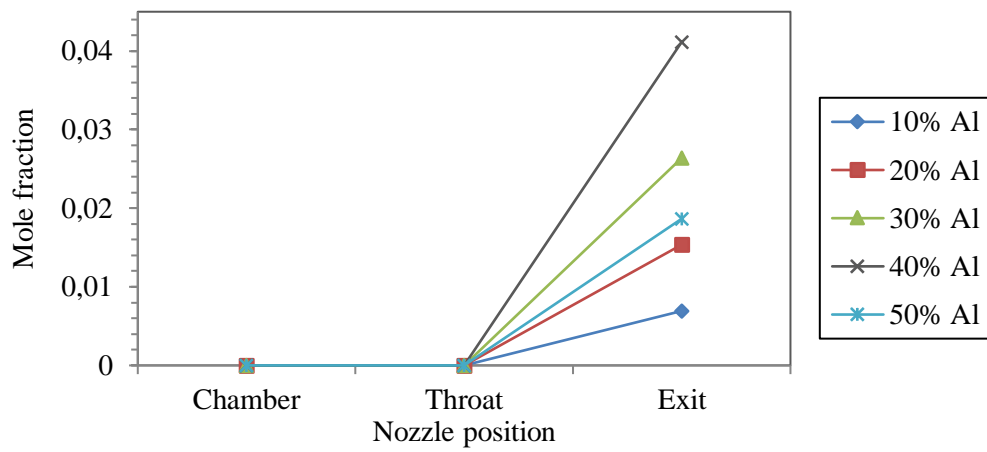


Figure 3.15: Mole Fraction of solid phase alumina in nozzle

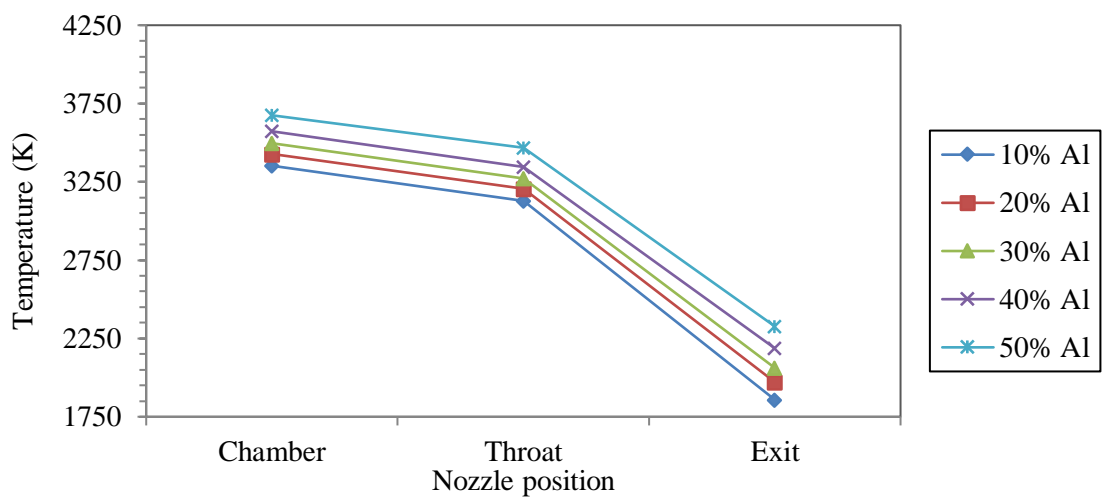


Figure 3.16: Temperature distribution in nozzle

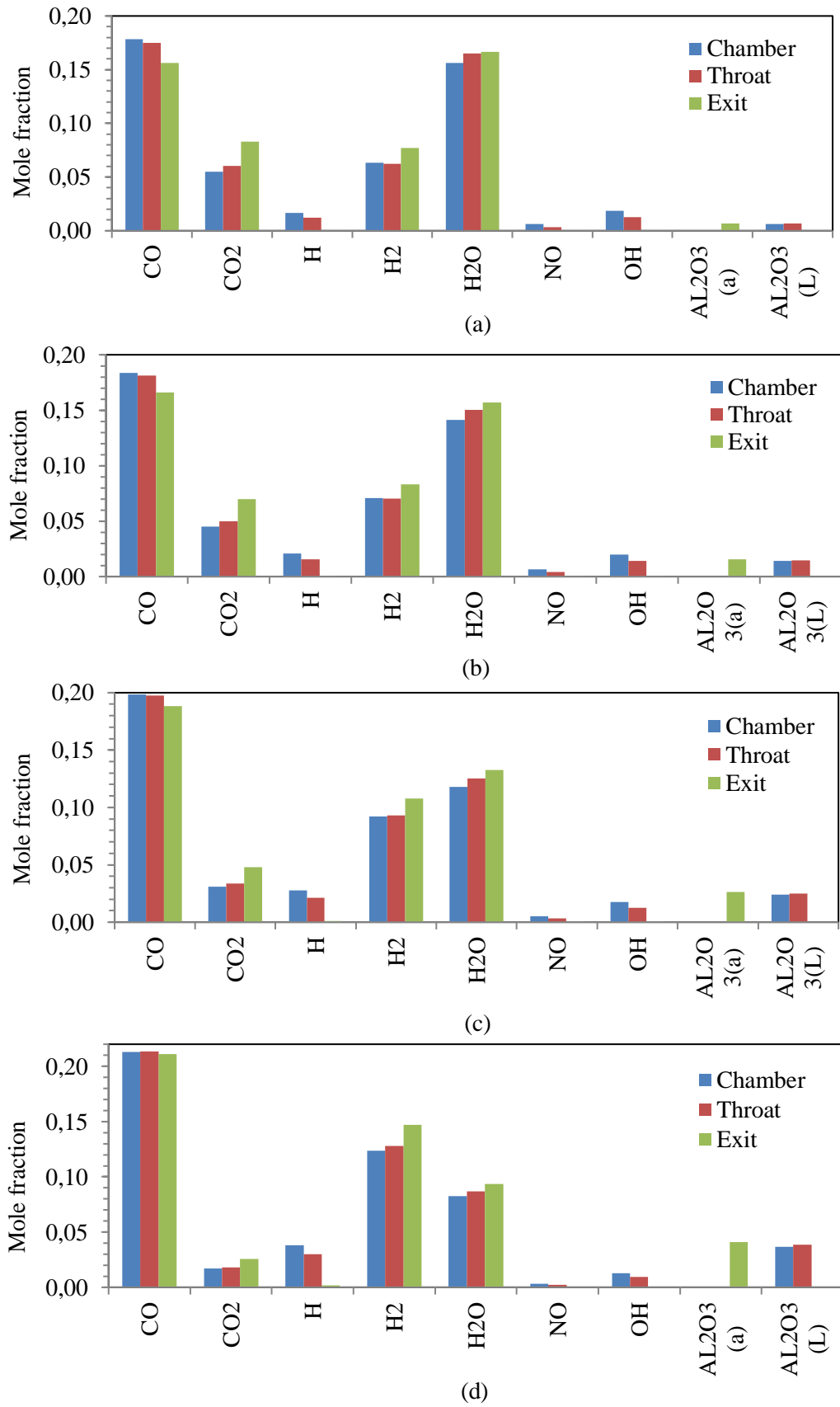


Figure 3.17: Oxidising species for (a) 10%, (b) 20%, (c) 30%, (d) 40%

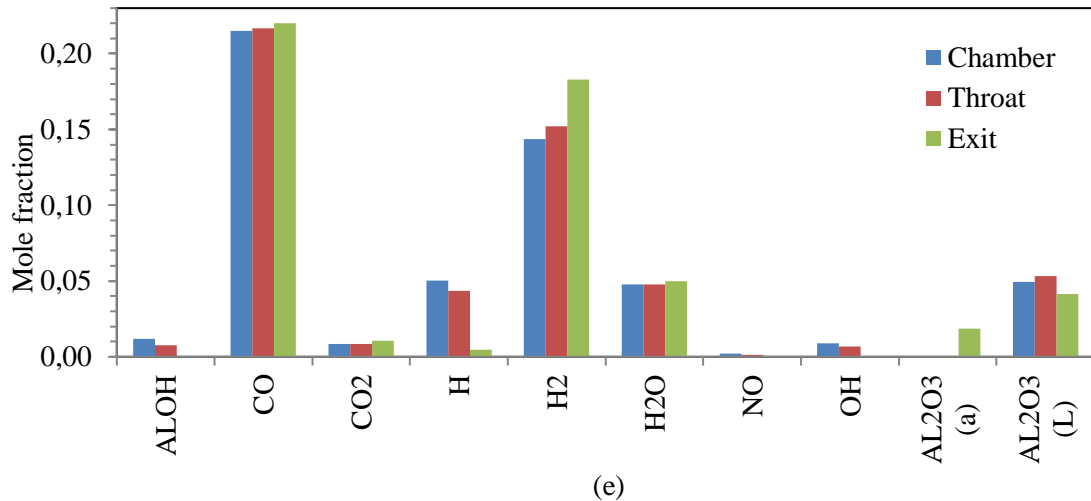


Figure 3.17 (cont.): (e) 50% aluminium loading

3.5. P1B system level design

3.5.1. Design methodology

If P1B is to be modular, it must be adaptable to varying propellant combinations, specifically aluminised and non-aluminised fuel grains. As in the case of P1A, P1B will hold 30 kg of nitrous oxide. The outer diameter of the fuel grain is constrained by the aluminium tubing, therefore for the same oxidiser mass, the fuel grain must be lengthened for increasing aluminium loading due to the higher regression rate. Increasing fuel grain length in turn increases the thrust due to the higher mass flow rates. However, the limited fuel diameter causes the burn time to reduce with increasing aluminium content as seen in Table 3.2. Being the first P1B rocket, this work concentrates on the design of a pure paraffin wax fuelled motor, but this will also serve as a baseline for future aluminised rockets. For this reason, the design of the P1B propulsion system is similar to that of P1A.

Figure 3.18 shows the design methodology used in the development of P1B specifications. The method consists of two iteration and optimisation loops. One loop optimises the propulsion system to attain the desired apogee while the second loop optimises the aerodynamic design of the vehicle to obtain a light weight and stable rocket. This dissertation focuses primarily on the propulsion system, however, in order to validate the propulsion design, a trajectory simulation of the vehicle is also required. This in turn necessitates the design and generation of an aerodynamics model to be used in the flight simulator. Using the procedure laid out in Figure 3.18 together with procedures in Figures 3.5 and 3.6, a complete propulsion system design was generated. Initial design assumptions were based on the P1A design specifications given in Table 2.1.

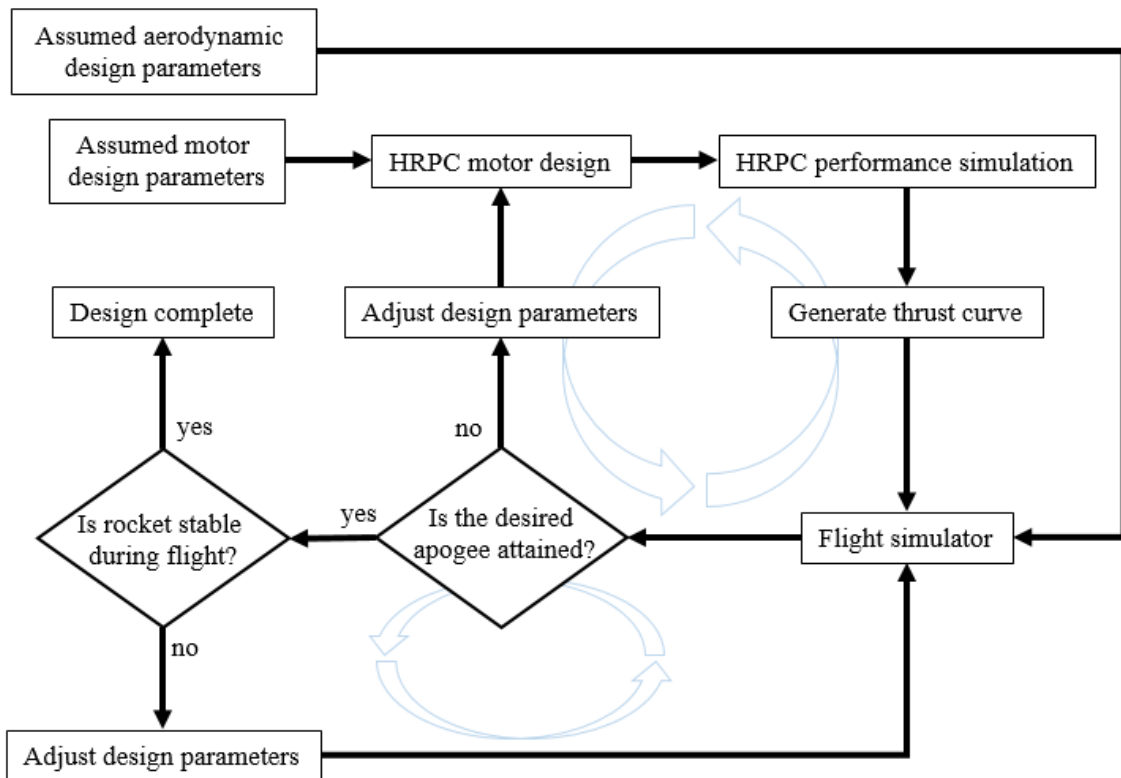


Figure 3.18: P1B design methodology

3.5.2. P1B specifications

In order to determine the optimal O/F ratio of the paraffin wax and nitrous oxide fuel combination of P1B, sub-model (2) of HRPC was employed. Analysing the characteristic velocity output, the peak O/F ratio was determined to be 6.8 as shown in Figure 3.19. This information together with the design thrust and combustion pressure data, was entered into sub-model (1). Table 3.5 summarises the steady state design specifications of P1B and Table 3.6 gives the nozzle specifications after entering data from sub-model (2) into sub-model (3). The nomenclature in Table 3.6 is coherent with Figure 3.20, where the bell and conical nozzle profiles are shown. After generating a thermochemistry database of the paraffin and nitrous oxide propellant combination, design specifications were entered into the hybrid motor performance simulator. The expected transient thrust, oxidiser tank pressure and combustion pressure for the P1B hybrid rocket are shown in Figure 3.21. The expected combustion temperature time trace is shown in Figure 3.22 and is used in the designing of the P1B nozzle. A time-average summary of selected parameters is shown in Table 3.7.

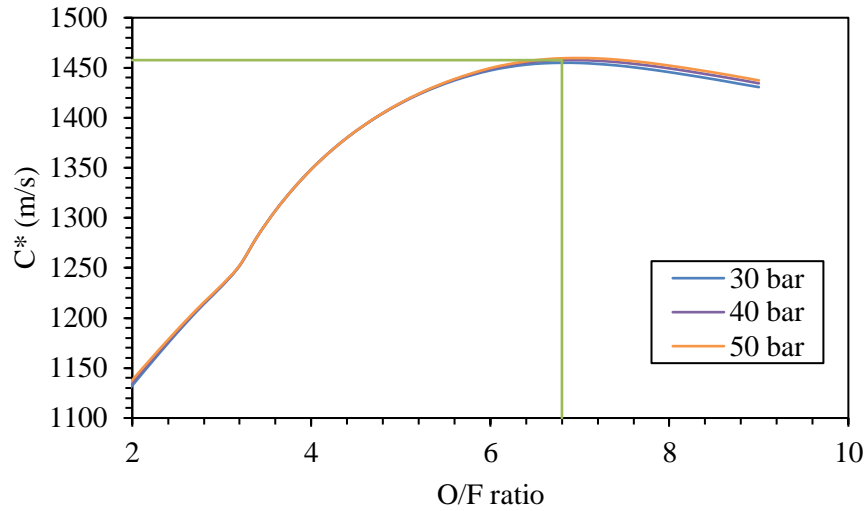


Figure 3.19: Characteristic velocity VS O/F ratio for varying combustion pressure

Table 3.5: P1B steady state design specifications

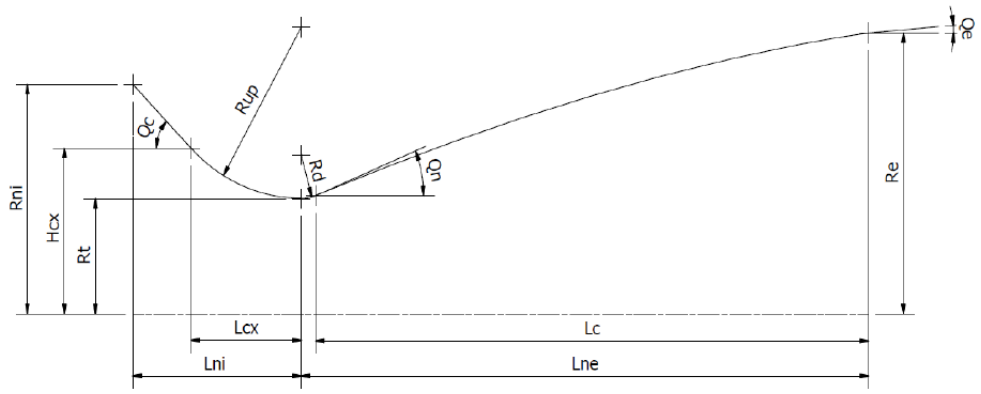
Parameter	Specification	Units
Design thrust	5000	N
Design O/F ratio	6.8	
Design chamber pressure	40	bar
Design atmospheric pressure	101325	Pa
Combustion efficiency	90	%
Burn time	18	s
1st critical pressure ratio	0.9936	
2nd critical pressure ratio	0.2330	
3rd critical pressure ratio	0.0253	
Characteristic velocity	1619.54	m/s
Thrust coefficient	1.5152	
Optimum nozzle expansion ratio	6.38	
Nozzle throat area	8.25×10^{-4}	m^2
Nozzle exit area	4.71×10^{-3}	m^2
Nozzle throat diameter	0.032	m
Nozzle exit diameter	0.077	m
Oxidiser mass flow rate per port	1.974	kg/s
Total fuel mass flow rate	0.290	kg/s
Fuel mass flow rate per port	0.290	kg/s

Table 3.5(cont.): P1B steady state design specifications

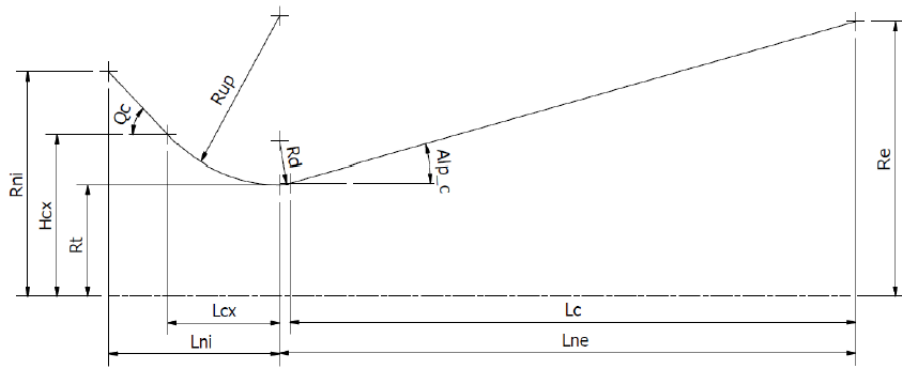
Total mass flow rate	2.264	kg/s
Nozzle mass flow rate	2.264	kg/s
Grain length	0.404	m
Grain diameter	0.148	m
Initial grain volume	5.80×10^3	m^3
Final grain volume	1.87×10^4	m^3
Initial grain mass	5.40	kg
Fuel density	930	kg/m^3
Grain type	Cylindrical port	
Number of ports	1	
Initial port diameter	0.06	m
Final port diameter	0.146	m

Table 3.6: Nozzle design specifications

Parameter	Property	Specification	Units
Nozzle contraction ratio		8	
Nozzle contraction angle	Qc	45	°
Ratio of upstream to throat radius	Rup/Rt	1.5	
Ratio of downstream to throat radius	Rd/Rt	0.382	
Nozzle Type		Bell-Shaped	
Nozzle parabola inlet angle	Qn	20.75	°
Nozzle parabola exit angle	Qe	7.5	°
Nozzle fractional length	Lf	1	
Nozzle half cone angle	Alp_c	15	°
Chamber radius	Rni	0.0458	m
Nozzle upstream radius	Rup	0.0243	m
Nozzle downstream radius	Rd	0.0061	m
Nozzle length from inlet to throat plane	Lni	0.0397	m
Length from contraction angle position to throat plane	Lcx	0.0172	m
Radius of contraction angle position to throat plane	Hcx	0.023	m
Nozzle total length from throat to exit plane	Lne	0.0932	m
Nozzle parabolic bell length	Lc	0.091	m



(a)



(b)

Figure 3.20: HRPC nozzle nomenclature, (a) bell nozzle, (b) conical nozzle (Genevieve, 2013)

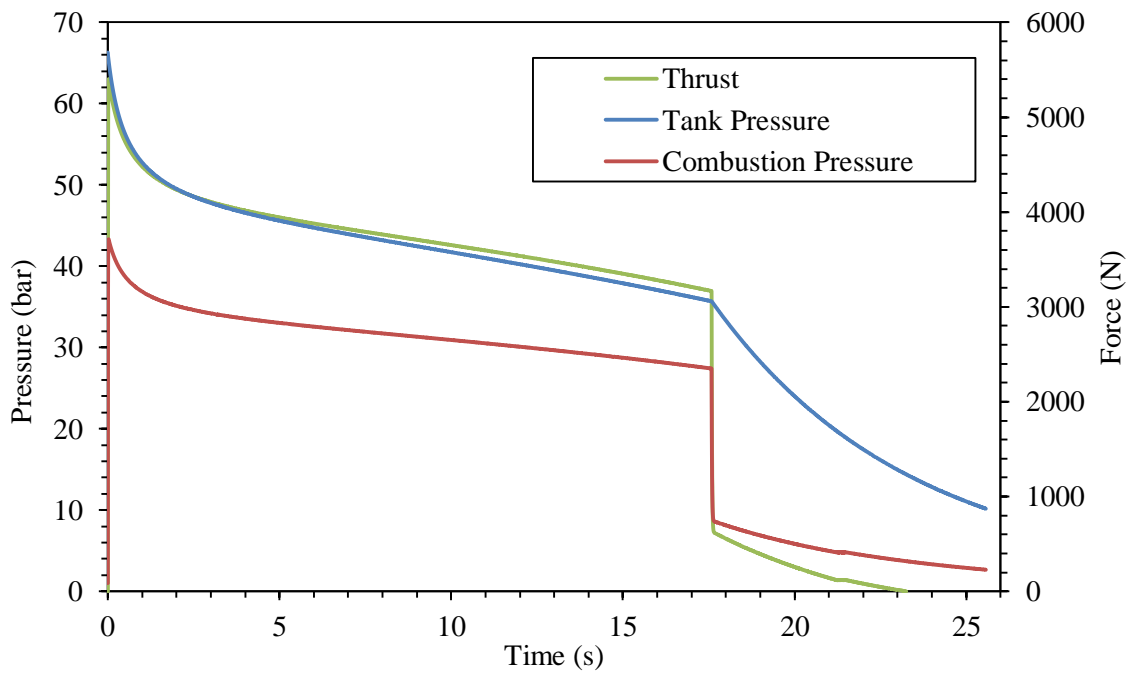


Figure 3.21: Theoretical PIB pressure and thrust time traces

Table 3.7: Time-averaged performance parameters for P1B

Parameter	Specification	Units
Oxidiser mass flow rate	1.14	kg/s
Fuel mass flow rate	0.21	kg/s
Total mass flow rate	1.35	kg/s
Nozzle mass flow rate	1.35	kg/s
Oxidiser mass flux per port	155.52	kg/s.m ²
Fuel regression rate	0.0017	m/s
Chamber O/F ratio	4.88	
Chamber Pressure	2340374.86	Pa
Nozzle exit pressure	64028.36	Pa
Nozzle exit velocity	2017.29	m/s
Nozzle exhaust velocity	1730.65	m/s
Characteristic velocity	1370.81	m/s
Thrust	2690.92	N
Vacuum thrust	3224.74	N
Momentum thrust	2887.46	N
Specific impulse	176.42	s
Vacuum specific impulse	252.46	s
Total impulse	68801.48	Ns

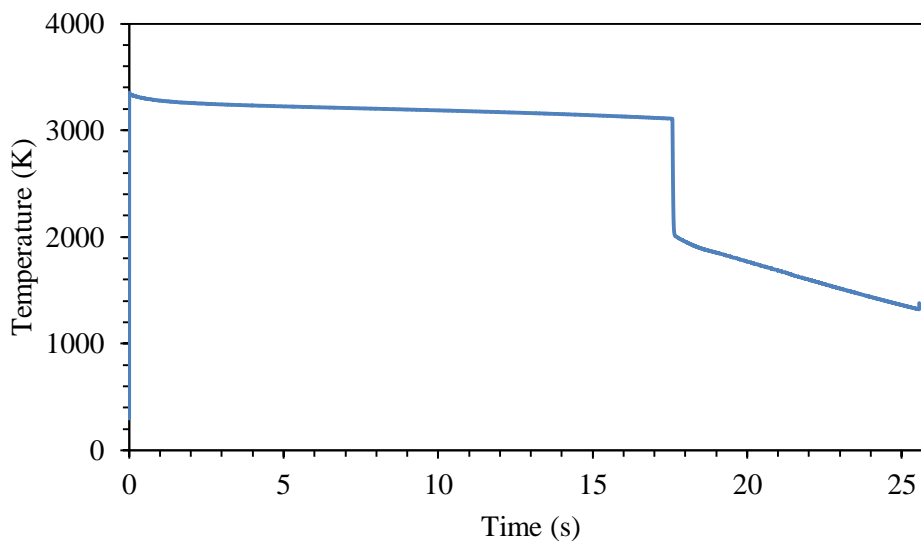


Figure 3.22: Combustion temperature time trace

3.6. Summary

The fuel regression rate is a fundamental parameter in the development of a hybrid rocket motor. The link between the model and experimental data was discussed in this chapter, and an empirical regression rate model characterised by the ballistic coefficient and exponent was presented. The procedural use of the HYROPS software was described. An investigation was conducted concerning the effects of aluminium loading on hybrid rocket design and nozzle design using HRPC and NASA CEA. This fed directly into the nozzle thermo-structural design described in Chapter 5. It was shown that the density specific impulse increases with increasing aluminium content and this in turn reduces the rocket mass, increasing performance. The process used to design the P1B hybrid motor was described and final design specifications were defined for use in Chapters 4, 5 and 6. The pure paraffin wax / nitrous oxide motor produces a peak thrust and combustion pressure of 5000 N and 40 bars respectively. The fuel grain has a port diameter (inner diameter) of 60 mm, an outer diameter of 148 mm and a length of 404 mm.

4. Phoenix-1B Propulsion System Component Design

4.1. Introduction

This chapter describes the structural components of the P1B propulsion system required to provide for the performance specifications in Chapter 3, with the exception of the nozzle which is discussed in Chapter 5. A method is presented for measuring oxidiser mass flow rate in real time and improved bulkhead retention methods are described for avoiding welding of components, as discussed in Chapter 2. Two methods are reviewed. Oxidiser tank and combustion chamber FEA results are discussed, including pressure testing results that confirm the structural integrity of the chosen manufacturing method for the P1B vehicle.

4.2. Instrumentation and feed system

In order to fuel the vehicle's tank with the intended amount of nitrous oxide, a vent system was incorporated on the rocket. This posed the challenge of monitoring the amount of nitrous oxide in the flight tank during propellant loading. An existing load cell installed on the launch gantry was previously used to measure the changing rocket mass, but only during static testing. An inexpensive method of monitoring the loaded nitrous oxide mass during flight test fuelling was therefore required. The solution consists of pressure and temperature sensors installed on the top (fore) and bottom (aft) ends of the flight tank to measure the hydrostatic pressure and therefore the mass of nitrous oxide loaded. The method also provides mass flow rate by measuring the time rate of change of hydrostatic pressure during static testing and flight, thus overcoming one of the shortfalls of P1A.

A layout of the N₂O monitoring system is shown in Figure 4.1. One of the goals of the P1B flight test will be to record motor and vehicle performance data during flight. Literature on in-flight monitoring of hybrid rocket performance is scarce, however, the method developed here to could provide this data to correlate the motor performance from ground testing to flight testing. The N₂O monitoring system works by measuring the height (h) of the liquid nitrous oxide level in the tank as given by Equations (4.1) and (4.2). Due to the self-pressurising nature of N₂O the vapour pressure (P_v) reading must be deducted from the higher pressure measurement given by the sensor located aft of the tank (P_l), this difference is the hydrostatic pressure. Since nitrous oxide has a relatively high compressibility, the liquid density (ρ_l) is dependent on the fluid temperature (T_l) and can be found using the temperature sensors together with Equation (4.3). This equation is an empirical correlation between the density of the fluid and the temperature, where the coefficients $C1$ to $C4$ are given in Table 4.1. Once the height of the liquid level is calculated the associated

mass of nitrous oxide can be found using Equation (4.4), however, P1B will not be launched from a 90° launch angle which means that the gravity (g) dependent hydrostatic force must be adjusted to compensate for varying launch gantry angles (θ) (Equation (4.5)). Combining Equations (4.5) and (4.6) the instantaneous nitrous oxide mass (m_{N_2O}) can be calculated using the inner diameter (D) of the oxidiser tank. To validate this method of oxidiser measurement, the calculated mass will be compared to the change in mass of both the MLP supply tanks and flight vehicle mass during fuelling in ground tests. It is noted that during flight, the vehicle will experience high acceleration forces, skewing the hydrostatic pressure measurement. The onboard inertial magnetic unit will measure this acceleration and will be used to compensate for the gravitational acceleration.

The feed system length of P1B was kept to a minimum to reduce overall rocket length, with only the ball valve and connectors being positioned between the tank and combustion chamber. The length of the feedline plays a factor in low frequency combustion instabilities and is discussed in Chapter 6.

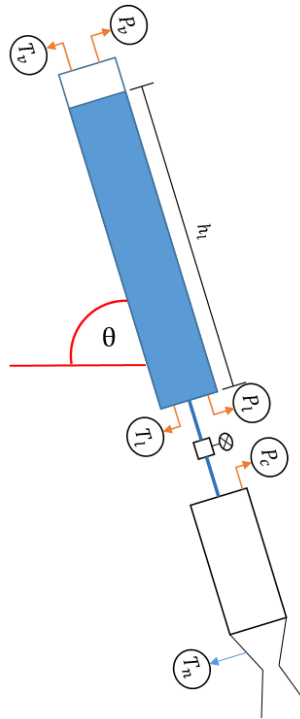


Figure 4.1: Schematic of propulsion system with sensors

$$\text{Hydrostatic pressure} = P = \rho g h \quad (4.1)$$

$$h = \frac{P_l - P_v}{\rho_L g} \quad (4.2)$$

$$\rho_l = \frac{C1}{C2\left(1+\frac{T_l}{C3}\right)^{C4}} MW \quad (4.3)$$

$$m_{N_2O} = \rho_L Vol = \rho_L Ah = \frac{\pi\rho_L D^2 h}{4} \quad (4.4)$$

$$h_l = \frac{P_l - P_v}{\rho_L g \sin\theta} \quad (4.5)$$

$$m_{N_2O} = \frac{\pi D^2 (P_L - P_v)}{4g \sin\theta} \quad (4.6)$$

Table 4.1: Density coefficients for nitrous oxide (Green and Perry, 2008)

C1	2.781
C2	0.27244
C3	309.57
C4	0.2882
Molecular weight (<i>MW</i>)	44.013 g/mol

4.3. Bulkhead retention methods

An alternate bulkhead retention method was needed for P1B to mitigate the negative effects of aluminium welding seen on P1A (Figure 2.10). This section describes two approaches: the first is a spiral locking ring and the second is the standard bolted design. The use of the locking ring potentially makes assembly and manufacturing easier over the bolted method but can be difficult to implement in thin-wall aluminium tubes. Both methods allow the bulkheads to be removed and re-installed while O-rings form a high pressure seal in both cases. A design was deemed acceptable if it was able to withstand 1.5 times the P1B operating tank pressure of 65 bar.

4.3.1. Spiral locking ring

The retaining ring is manufactured by drawing wire through a rectangular die, pressing it flat and then winding it on its edge to produce a spiral ring. Installation requires a groove to be machined on the internal surface of the tubing. Figure 4.2 illustrates a cross sectional view of a pressure vessel design that was used for analysis, FEA and hydrostatic pressure testing in this study. The MIL-DTL-27426C standard (United States Military, 1998) and Smalley design handbook (Smalley, 2015) for retainer ring design were used to determine the viability of the design. The tube inner diameter and bulkhead diameter were both 153 mm. The bulkheads on either end of the test article were designed with sufficient strength to avoid bulkhead failure.

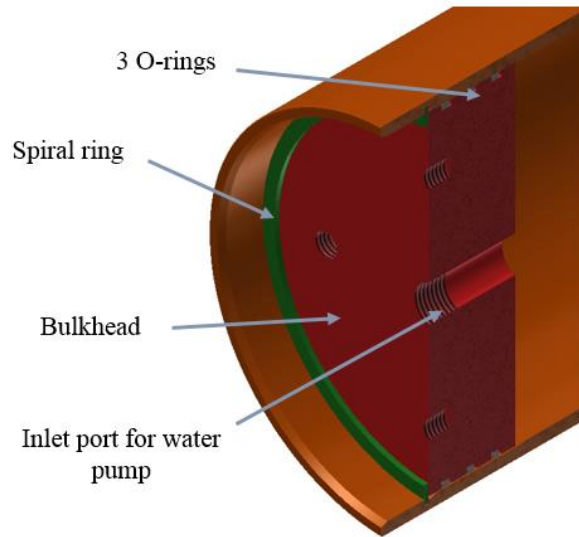


Figure 4.2: Cross section of retaining ring design (Balmogim, et al., 2015)

Analytical calculations were completed on the ring shear and groove deformation. There are two modes of failure with this design: one is the shearing of the ring and the other is the yielding of the groove material. The allowable load based on the ring shearing (F) is given by:

$$F = \frac{D T S_s \pi}{SF} \quad 4.7$$

The allowable load based on groove deformation is given by:

$$F = \frac{D d S_y \pi}{SF} \quad 4.8$$

where D is the tube inner diameter, d is the groove depth, S_y is the yield strength of tube, S_s is the shear strength of the ring material and T is the ring thickness. A standard sized ring was selected from carbon steel with an inner diameter of 155 mm, outer diameter of 164 and a thickness of 2.18 mm. The material properties for carbon steel and aluminium 6061-T6 are shown in Tables 4.2 and 4.3 respectively. It can be seen in Table 4.4 that the design is limited by the aluminium groove which has a safety factor that is higher than the required value of 1.5.

Table 4.2: Carbon steel material properties (Smalley , 2015)

Property	Units	Specification
SAE code		1060-1075
Tensile strength	MPa	1248
Shear strength	MPa	710
Modulus of elasticity	GPa	206.8

Table 4.3: Aluminium 6061-T6 material properties (MatWeb, 2016)

Property	Units	Specification
Density	kg/m ³	2700
Ultimate tensile strength	MPa	310
Tensile strength, yield	MPa	276
Modulus of Elasticity	GPa	68.9
Ultimate compression strength	MPa	607
Compression strength, yield	MPa	386
Poissons ratio		0.33
Shear Modulus	GPa	26
Shear Strength	MPa	207
Coefficient of linear expansion	m/mK	23.6
Specific heat capacity	J/gK	0.896
Thermal conductivity	W/mK	167

Table 4.4: Analytical results of spiral retaining ring design

Parameter	Unit	Value
Pressure	bar	65
Force on flat head bulkhead	kN	124.24
Allowable force based on ring shear	kN	758.56
Allowable force based on groove deformation	kN	229.95
Safety factor on ring shear		6.11
Safety factor on groove deformation		1.85

Structural analysis

A 2D axisymmetric structural assembly analysis was compiled on the spiral locking ring design using ANSYS Workbench™. A pressure load of 65 bar was applied on the internal surface of the test specimen. The symmetric model and loading conditions allowed for only one end of the pressure vessel to be analysed. A frictionless constraint was applied to the shell wall in the symmetry plane, allowing for lateral but no axial movement. Friction contacts were applied to all mating surfaces. The Von Mises stresses seen in Figure 4.3 are exceptionally high with a pressure loading of 65 bars. This was due to the sharp corners of the model. Regions of higher stress can be seen in Figure 4.4(b) with a 276 MPa limit applied. This showed that the design was acceptable in theory.

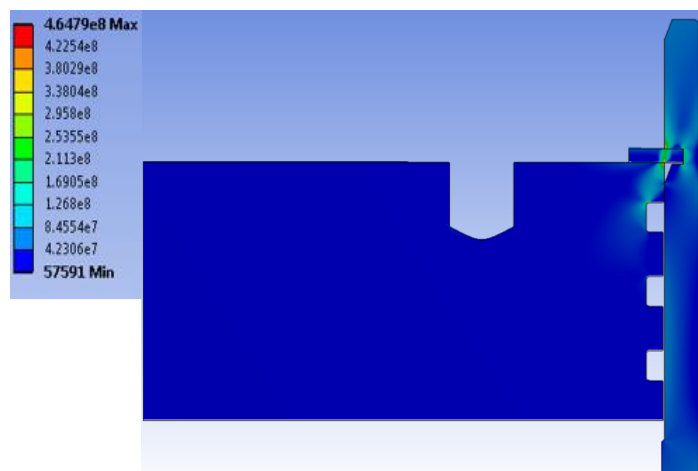


Figure 4.3: Von Mises stresses of retainer ring design for internal pressure of 65 bar.

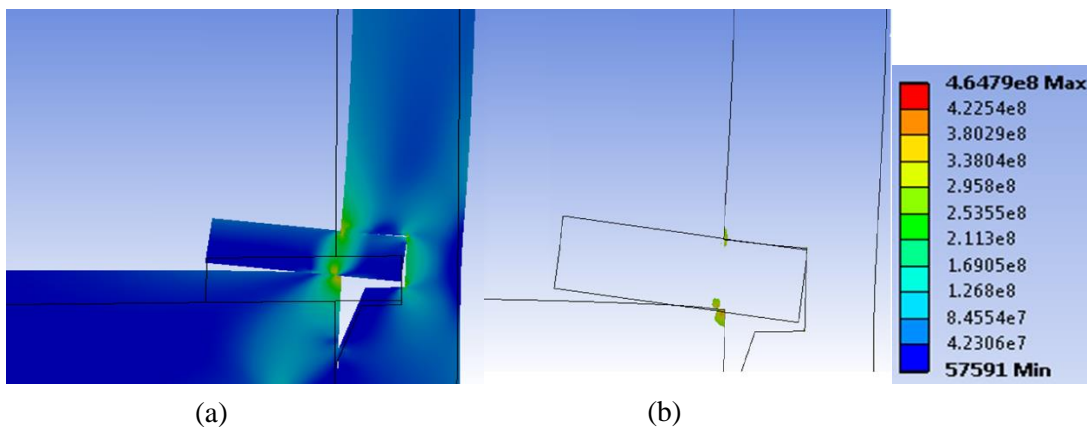


Figure 4.4: Von Mises stress with 10x scaled deformation (a) close up spiral ring region, (b) Iso-capped surface showing stresses higher than 276 MPa

Hydrostatic pressure testing

A hydrostatic pressure test was conducted up to failure in order to validate the spiral retaining ring design. The burst pressure occurred at 150 bar and although this suggested that the design met the 98 bar safety minimum, some axial movement of the ring and bulkhead was noticed. Movement initially started around the 80 bar pressure level. Figure 4.5 shows the deformation of the ductile aluminium shell due to the crushing force of the bulkhead on the relatively rigid spiral retainer ring. Burst failure ultimately occurred due to the high tensile stresses on the reduced wall thickness in the retainer groove (Balmogim, et al., 2015). To avoid imparting undue stresses on the feed system that would be connected to the bulkhead, a bolted design was thus considered preferable for the P1B pressure vessels.

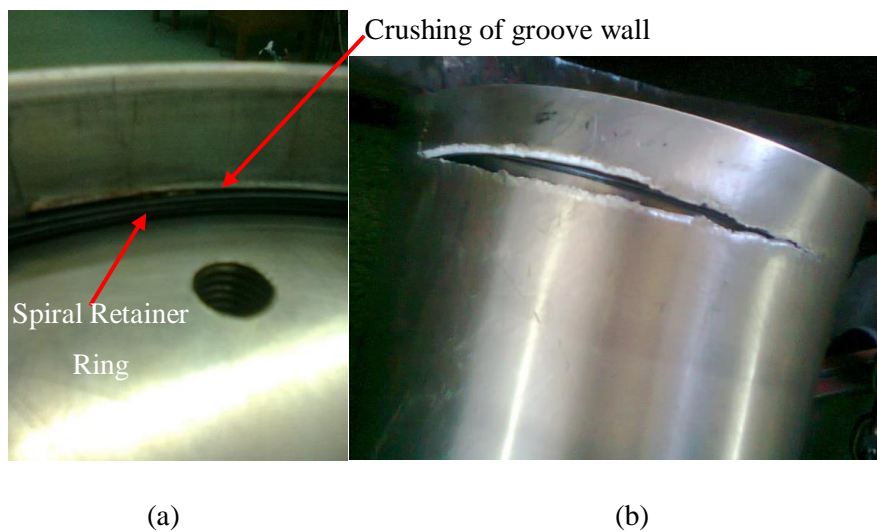


Figure 4.5: (a) Tube deformation and ring movement; (b) Pressure vessel failure at 150 bars (Balmogim, et al., 2015)

4.3.1. Bolted bulkheads

Radially bolting the bulkhead through the shell wall is a common method of bulkhead retention, and also ensures easy assembly and disassembly. Stress calculations and analyses initially assumed the use of SAE grade 9.8 button head bolts but for increased safety, it was decided to use stronger and corrosion resistant stainless steel grade 304 button head bolts. The limiting factor of this design was the aluminium shell wall. In reducing the bearing load on the tank wall, the number and sizing of the button head bolts were found to be twenty four and M8 respectively.

A 3D cyclic-symmetry FEA assembly model of the bolted bulkhead design was developed and analysed. An assembly analysis allowed for a less rigid constraint in the vicinity of the bolted region of the shell. The FEA model is shown in Figure 4.6. ANSYS Workbench™ has the

capability to model bolt threads using contacts instead of modelling the actual thread geometry and this does not require the thread interfaces to be designed and meshed. Frictional constraints were applied to all contact regions. Thread geometry modifications were applied to the frictional contact between the thread regions of the bolt and bulkhead. The associated pitch and thread specifications related to an M8 bolt were then set. As with the axisymmetric analysis for the spiral ring, a frictionless constraint was applied to the tank wall as illustrated in Figure 4.6. A pressure of 65 bars was applied to all internal surfaces. Figure 4.7 gives the Von Mises stress results of this analysis.

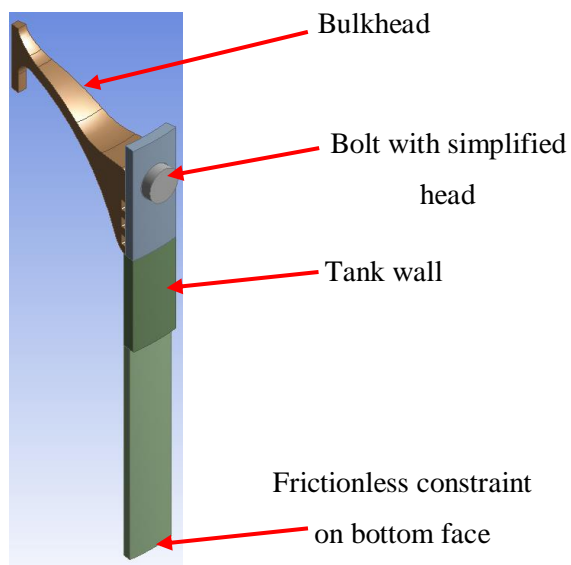


Figure 4.6: Bolted bulkhead FEA model

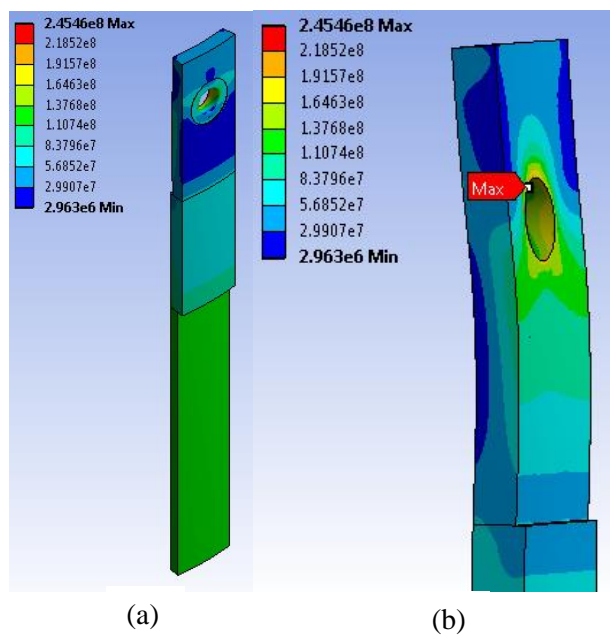


Figure 4.7: (a) Von Mises stress on shell, (b) Close-up of high stress area (deformation scaled up 20x)

During operation, the pressure contained in the vessel imparts a force on the bulkhead causing the radial bolts to bend around the hole in the shell. Since each bolt is relatively rigid compared to the aluminium shell, a bending moment occurs which elongates the hole until failure occurs between neighbouring holes, as seen in Figure 4.7(b). Bolt pretension of 6 kN was applied to the bolt prior to pressure loading to simulate bolt torqueing during assembly. This strengthens the joint. Excessive bolt loading will crush the tube wall and strip the aluminium bulkhead threads. Figure 4.8 illustrates the peak stress of the joint with various bolt pretensions. A pretension of 6 to 6.5 kN correlates to a torque setting 10 to 11 Nm which results in a minimum stress of 245MPa. Again, these stresses are only seen on the sharp edge of the hole with the rest of the model experiencing stresses lower than 184 MPa, indicating a 1.5 safety factor on yield.

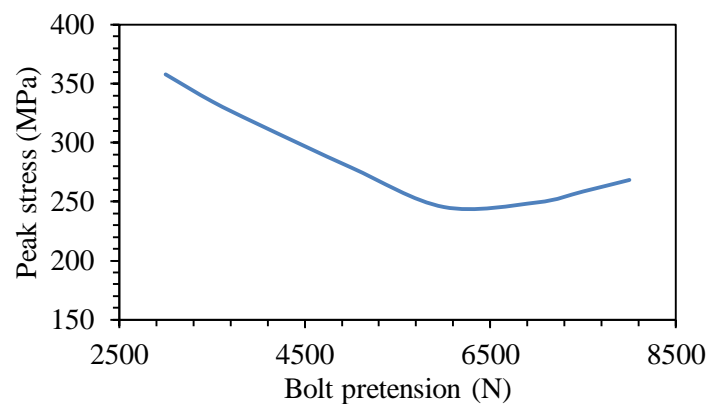


Figure 4.8: Bolt-pretension study

4.4. P1B pressure vessel

4.4.1. Oxidiser and combustion chamber shell

The tank shell was constructed from a section of aluminium 6061-T6 tubing, with each tube having a standard length of 2.4 m and an outer and inner diameter of 164 mm and 153 mm respectively. Upon measurement it was found that the tubes exhibited ovality, exceeding the allowable limit of the O-rings. This also complicated the machining process but the correct tolerances were nevertheless achieved. The standard hoop and longitudinal stresses for a cylindrical pressure vessel were calculated using equations (4.9) and (4.10) and safety factors of 3.05 and 6.1 were obtained respectively for the bulk tube at 65bar of pressure. The sealing surfaces were machined to a diameter of 155 mm and a depth of 52mm. This reduced safety factors for the hoop and longitudinal stresses to 2.47 and 4.93 respectively. The resulting safety factors suggest that the shells are heavier than needed but due to the ovality and the complexities around machining slender aluminium components, it was decided not to remove excess material. The

reduced wall thickness and associated stresses are visible in Figure 4.7. In the equations (4.9) and (4.10), P is the internal pressure, r is the radius and t is the wall thickness of the vessel.

$$\sigma_{hoop} = \frac{Pr}{t} \quad (4.9)$$

$$\sigma_{longitudinal} = \frac{Pr}{2t} \quad (4.10)$$

4.4.2. Bulkheads

The bulkheads close off each end of the oxidiser tank and allow for mounting of the injector at the fore end of the combustion chamber, as depicted in Figure 4.9. They also allow for all fluidic and structural connections. A finite element analysis conducted on the aluminium 6082-T6 fore, aft and injector bulkheads is discussed in this section. As per Chapter 2, aluminium welding was to be avoided, therefore bosses were incorporated in each bulkhead design, even though this increased cost.



Figure 4.9: P1B propulsion system illustrating location of bulkheads

The constraints in the single-part FEA analyses for the three bulkheads were similar with the exception of the injector bulkhead having 20 threaded holes instead of 24 as per in the oxidiser tank bulkheads. The applied pressure was 80 bar for the fore and aft bulkheads and 60 bar for the injector bulkhead. These higher-than-expected operating pressures were applied so that the results would be comparable to those from the hydrostatic testing. The boundary condition applied in the analyses consisted of a frictionless support on the circumferential surface, to model the presence of the aluminium tube. A cylindrical constraint was applied to the bottom half of all the bolt holes. Analysis results are discussed in this section with stresses being lower than the yield strength of aluminium.

Analytical stress calculations for the hemispherical bulkheads (similar to Equations (4.9) and (4.10)) resulted in a common minimum wall thickness of 2 mm. For practicality and machinability, the thickness was increased to 4 mm for the fore and aft bulkheads while the injector bulkhead thickness was increased further to a conservative 6 mm so as to accommodate

the higher operating temperatures caused by the proximity to the combustion chamber. Figure 4.10 shows the machined coupler mount that could be used to connect the combustion chamber to the oxidiser tank via a coupler tube (Figure 4.9) and studs (Figures 4.11, 4.13 and 4.14). The hole pattern that is seen on the mount, aligns to the studs that are consistent on all bulkheads. These are used as structural connections between vehicle sections and aid in the installation and removal of the bulkheads with the use of a manufactured bulkhead tool. A tube section was bolted to the coupler mount on the aft and injector bulkheads. The studs on the fore bulkhead can also be used as parachute anchor points if the recovery of the booster is required.



Figure 4.10: Coupler mount

Fore bulkhead

The fore pressure tank bulkhead contains the oxidiser vapour pressure and temperature sensors and a part of the vent system. Figure 4.11(left) illustrates the design with attached sensors and quick-connect. FEA results are shown in Figure 4.11(right) for an internal pressure loading of 65 bar and it can be seen that bulk of the component does not experience significant stress. The maximum stress seen is due to a sharp corner in the threaded hole. An area of high stress is the hemispherical section which experiences a stress of 73.13 MPa and correlates to a safety factor of 3.77.

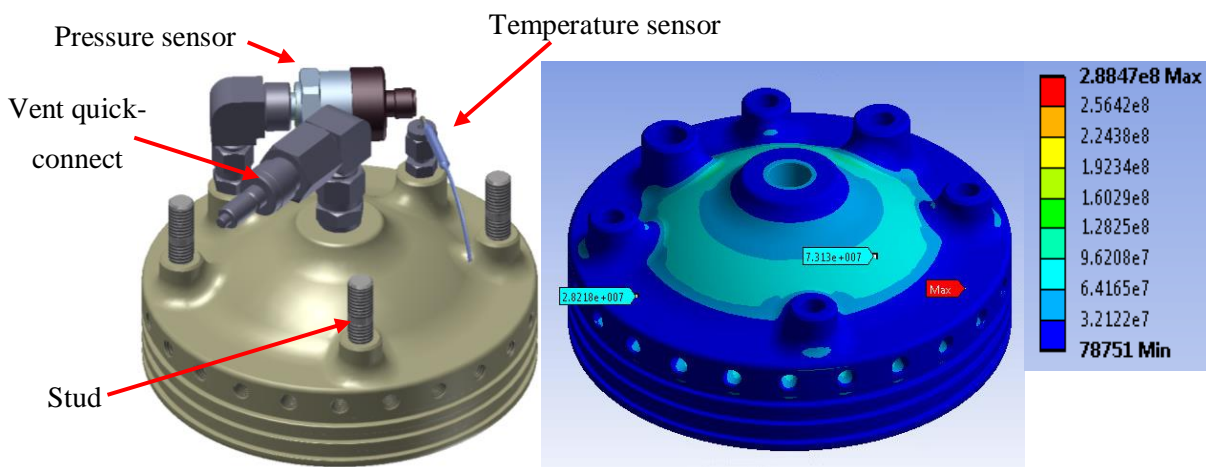


Figure 4.11: (Left) fore bulkhead assembly, (right) Von Mises stresses in Pascal

As seen in Figure 4.11, the fore bulkhead contains the vent quick-connect which connects the tank to the vent system on the GSE, as shown in Figure 4.12. The system also consists of a ball valve that is actuated with a servo motor via a gear set and a pressure (P) and temperature (T) sensor. The automated ball valve allows for the vent line to be fully opened or closed, or opened to an intermediary angle. During propellant loading, the vent valve is opened which releases the pressure in the flight tank, thus driving in more nitrous oxide due to the greater pressure differential. The valve is controlled remotely as with the rest of the GSE and is opened to a specified angle depending on the pressure in the flight tank. It was decided to open the valve when 30 to 35 bar of pressure was reached within the oxidiser tank, as this ensures a sufficient driving pressure differential. Lowering the tank pressure further means a greater pressure differential, but the temperature decreases with the lowering pressure which may cause the o-rings to harden and lose their ability to seal around the bulkheads. The fore bulkhead features a temperature and pressure sensor; another set of sensors was installed on the vent system for redundancy. The quick-connect is retracted with a pneumatic piston, in a similar fashion to the propellant fuelling quick-disconnect located on the aft bulkhead.

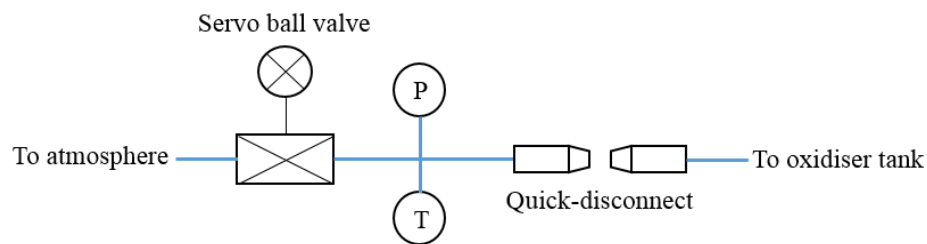


Figure 4.12: Schematic of vent system

Aft bulkhead

The aft bulkhead contains the liquid pressure and temperature sensors, the fuelling quick-disconnect and the connection for the MOV. Figure 4.13(left) illustrates the design with attached sensors and quick-connect. Similar to the FEA of the fore bulkhead, the analysis results for an internal pressure of 65 bar (Figure 4.13(right)) are skewed due to a sharp corner in the bolt hole but the stress seen on the bulk of the component is not significant. A high stress of 81.76 MPa is seen between a boss and the hemispherical section which corresponds to a safety factor of 3.38. Even though the fore and aft bulkheads are simulated to contain the same pressure, the additional boss on the aft bulkhead decreases the safety factor.

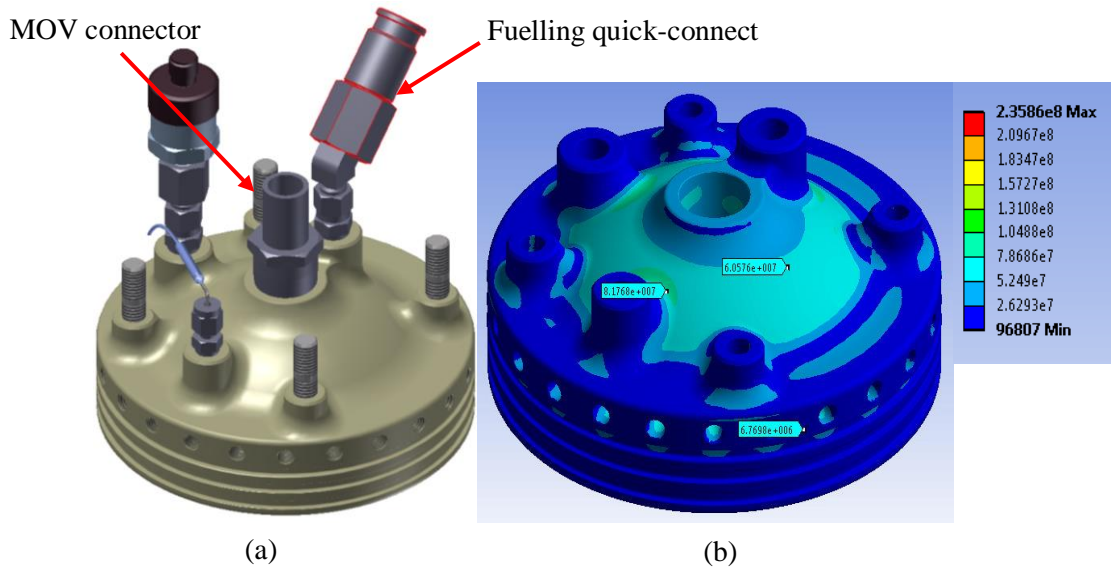


Figure 4.13: (Left) aft bulkhead assembly and (right) Von Mises stresses in Pascal

Injector bulkhead

The injector bulkhead contains the combustion pressure sensor connector and the connection for the MOV and can be seen in Figure 4.14(left). The design combustion pressure is 40 bar, however, to account for combustion instabilities that may develop, the maximum expected operating pressure (MEOP) is 60 bar. FEA results are shown in Figure 4.14(right) for the MEOP case with the maximum stress on the hemispherical section being 113.9 MPa. The higher stresses seen here, compared to the other bulkheads, is due to the flat surface on the inside of the bulkhead which is used in the fastening of the injector plate. The oxidiser tank bulkheads have a uniform hemispherical shape on the internal surface. However, the safety factor of this design is 2.42 which is significantly higher than the allowed value of 1.5.

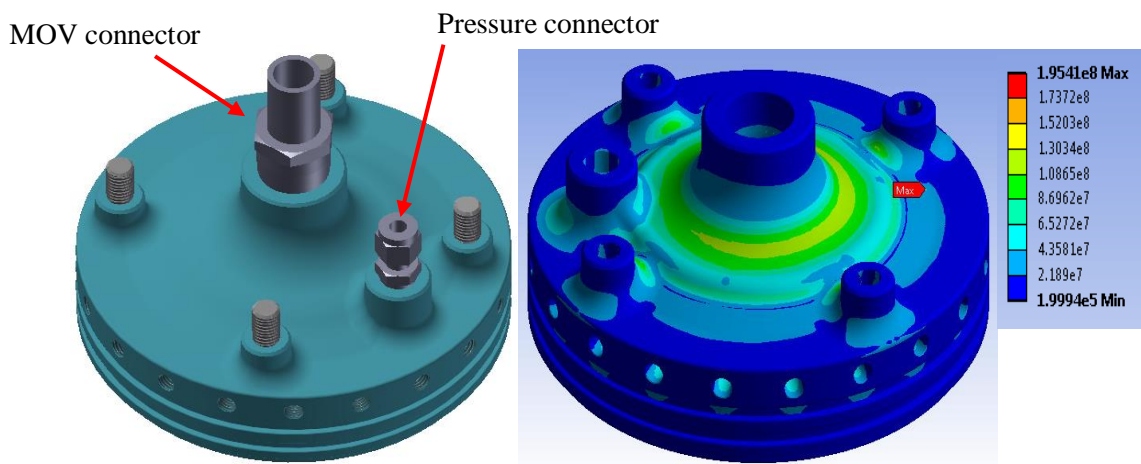


Figure 4.14: (Left) injector bulkhead assembly and (right) Von Mises stresses in Pascal

4.4.3. Manufacturing and pressure testing

The manufactured fore, aft and injector bulkheads are seen in Figure 4.15(a) to (c). The oxidiser tank and the combustion chamber were pressure tested to 80 bars and 60 bars respectively using nitrogen gas. The test procedure consisted of incrementally increasing the pressure and then holding steady for one minute between increments. The pressure was then held at 80 or 60 bar for 5 minutes. Soapy water was sprayed around all connections to ensure no gas leakage. A flat bulkhead replaced the nozzle in the combustion chamber for pressure testing. Figure 4.16 shows the test set up for the two vessels.



(a)

(b)



(c)

Figure 4.15: (a) Fore bulkhead assembly, (b) aft bulkhead assembly, (c) injector bulkhead assembly

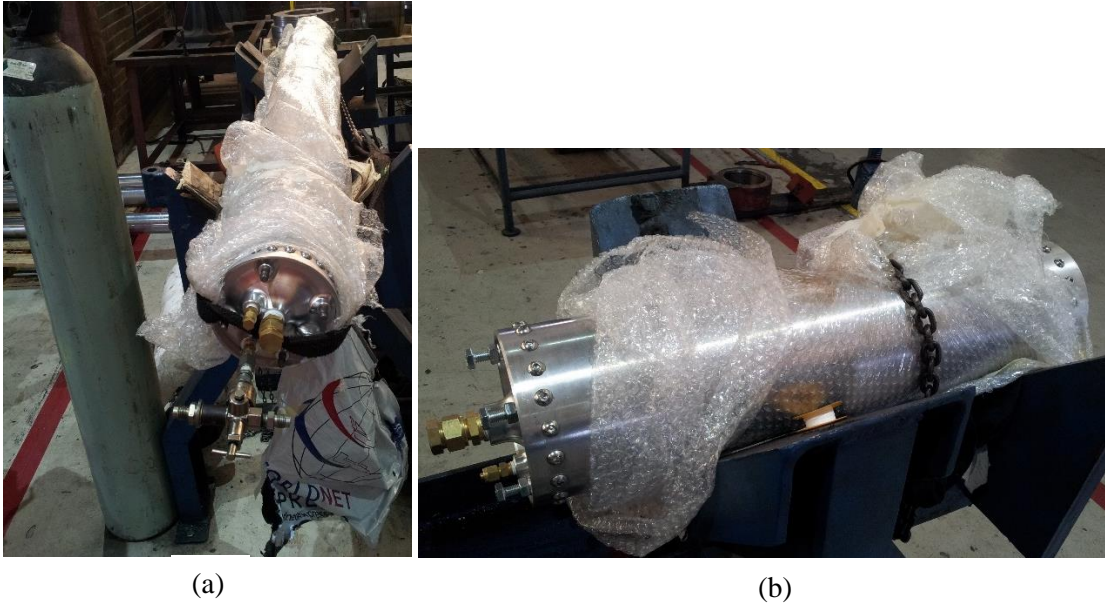


Figure 4.16: Pressure testing setup of (a) oxidiser tank and (b) combustion chamber

4.6. Summary

A method of measuring oxidiser mass flow rate from the hybrid rocket flight tank to the motor has been described. This utilises data from the hydrostatic pressure sensors located at the fore and aft positions of the vessel. Both spiral ring and bolted bulkhead retention methods were investigated for closing off the tank. The spiral ring design was manufactured and hydrostatically tested to failure at 150 bars. A bolted design was chosen to avoid undue stresses on the feed system. Design, analysis and pressure testing showed that the safety factor of the designs were adequate. The higher safety factors seen in Table 4.5 were due to practicality in handling and manufacturing the components. In the case of the combustion chamber vessel, the design pressure was 40 bar but to account for combustion instabilities, the maximum expected operating pressure was set at 60 bar.

Table 4.5: Safety factors the oxidiser and combustion chamber vessels

Component	Pressure (bar)	Safety factor
Oxidiser tank shell	65	3.05
Fore bulkhead	65	3.77
Aft bulkhead	65	3.38
Chamber shell	60	3.31
Injector bulkhead	60	2.42

5. Phoenix-1B Nozzle Design and Analysis

5.1. Introduction

P1A suffered substantial nozzle failure during launch and this was one of the main contributing factors to the vehicle not reaching its predicted altitude. This chapter describes the design and analysis of a new composite nozzle required to avoid structural failure while withstanding the higher temperature and pressure loadings experienced due to metallised fuel grains. The P1B nozzle design accommodates a worst-case thermal load consistent with a 40% aluminised fuel grain as per the discussion in Chapter 3. The final nozzle was manufacture to the author's design specifications by Rheinmetall Denel Munition (RDM). The author acknowledges the provision of technical advice by RDM.

5.2. Design of rocket nozzles

5.2.1. Background

The main function of a rocket nozzle is to convert the thermal energy of the combusted fuel and oxidiser into kinetic energy as efficiently as possible, obtaining high exhaust velocities along the thrust axis. An optimised nozzle design is one that is balanced between weight, performance, manufacturability and cost. It can be shown that the thrust (F) generated by a rocket motor has the form (Wirsig, 1996):

$$F = A_t P_0 \gamma R \left\{ \frac{2T_t T_0}{\gamma - 1} \left(\frac{2}{\gamma + 1} \right)^{\frac{1}{\gamma - 1}} \left[1 - \left(\frac{P_e}{P_0} \right)^{\frac{\gamma - 1}{\gamma}} \right] \right\}^{1/2} + (P_e - P_a) A_e \quad (5.1)$$

where A_t is the nozzle throat area, P_0 and T_0 are the combustion chamber pressure and temperature respectively which is approximated to the stagnation properties, γ is the specific heat ratio of the combusted gas, R is the universal gas constant, T_t is the gas temperature in the nozzle throat, P_e is the pressure at the exit plane of the nozzle, P_a is the ambient atmospheric pressure and A_e is the nozzle exit area. The coefficient of thrust is defined as:

$$C_f = \frac{F}{A_t P_0} \quad (5.2)$$

Combining Equations 5.1 and 5.2 results in:

$$C_f = \left\{ \frac{2\gamma^2}{\gamma - 1} \left(\frac{2}{\gamma + 1} \right)^{\frac{\gamma + 1}{\gamma - 1}} \left[1 - \left(\frac{P_e}{P_0} \right)^{\frac{\gamma - 1}{\gamma}} \right] \right\}^{\frac{1}{2}} + \frac{(P_e - P_a) A_e}{P_0 A_t} \quad (5.3)$$

which shows that the thrust coefficient depends predominantly on the nozzle characteristics with the exception of γ , which in turn illustrates the direct dependency of nozzle design on rocket performance.

There are three main regions of interest when designing a De-Laval nozzle namely the entrance/convergent, throat and exit/divergent sections. The subsonic flow in the entrance of the nozzle is insensitive to the shape, however the proper design of the divergent nozzle section is critical. There are a variety of nozzle types with conical and bell shaped being the most common. Conical nozzles are easier to manufacture but suffer divergence losses due to the flow dispersion at the exit. Bell shaped nozzles of the same length as the conical type have a higher efficiency as the flow is nearly axial at exit but they are complex in design and manufacturing.

The most accurate and optimal method to design a bell shaped nozzle divergent section is the method of characteristics. This method considers the expansion waves in the exit section and finds the minimum length such that there is uniform parallel flow in the exit plane. In this work the approximation method proposed by Rao (1958) was used which is simpler than the method of characteristics and is generally used in low-powered rockets.

The HRPC nozzle model used in this work applies the approximate optimisation approach (Genevieve, 2013). The method approximates the contour with a parabolic function, given by the rotated parabolic segment equation:

$$y' = Px' + Q + \sqrt{Sx' + T} \quad (5.4)$$

Here, y' and x' (Figure 5.1) are the co-ordinates of the local position of interest and P , Q , S and T are coefficients. Rao (1958) suggested the following ratios for the upstream (Equation (5.5)) and downstream (Equation (5.6)) radii at the throat (Figure 5.1).

$$R_1 = 1.5R_t \quad (5.5)$$

$$R_1 = 0.382R_t \quad (5.6)$$

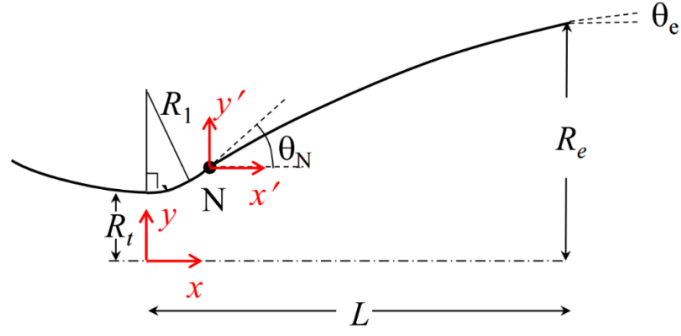


Figure 5.1: Approximate optimization approach (Seitzman, 2012)

The coefficients P , Q , S and T are solved with the application of four boundary conditions (Figure 5.1):

1. At N : $x'_N = y'_N = 0$
2. At exit: $x'_e = x_e - x_N = L - x_N = L - R_1 \sin \theta_N$;
 $y'_e = y_e - y_N = \sqrt{\varepsilon} R_t - y_N = \sqrt{\varepsilon} R_t - [R_t + R_1(1 - \cos \theta_N)]$
3. At N : θ_N is selected from the graph in Figure 5.2
4. At exit: θ_e is selected from the graph in Figure 5.2

These conditions yield:

$$T = Q^2 \quad (5.7)$$

$$Q = S/2(\tan \theta_N - P) \quad (5.8)$$

$$S = (y'_e - P x'_e)^2 (\tan \theta_N - P) / x'_e \tan \theta_N - y'_e \quad (5.9)$$

$$P = \frac{y'_e \tan \theta_N + y'_e \tan \theta_e - 2 x'_e \tan \theta_e \tan \theta_N}{2 y'_e - x'_e \tan \theta_N - x'_e \tan \theta_e} \quad (5.10)$$

The initial and final parabolic angles are found using Figure 5.2 with the expansion area ratio, ε , and the assumed reduction in nozzle length from a conical type at 15° half angle as given by Equation (5.11). Choosing of percentage length reduction is at the designer's discretion, based on the divergence losses. Inserting the calculated coefficients in Equation (5.4) results in a parabolic expression defining the divergent section contour.

$$L = f(\%) \left[\frac{R_t(\sqrt{\varepsilon} - 1) + R_1(\sec 15^\circ - 1)}{\tan 15^\circ} \right] \quad (5.11)$$

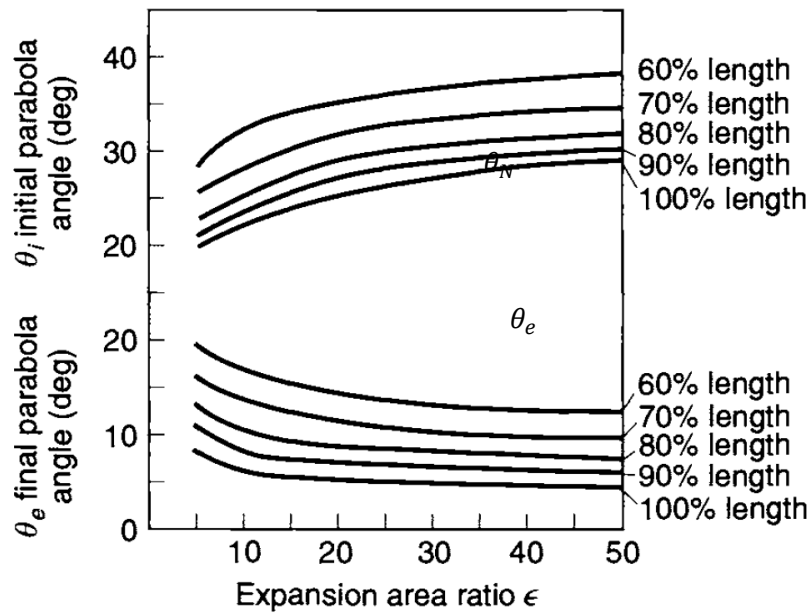


Figure 5.2: Nozzle design angles (adapted from Sutton and Biblarz (2001))

5.2.2. Design methodology

Nozzle design is a dynamic and iterative process requiring the optimisation of aerodynamics, thermal performance and structural design. At the same time mass must be minimised to maximise rocket performance. Figure 5.3 illustrates the procedure used in this study to design the P1B rocket nozzle. The flow chart was modified from standard design process by NASA (1975), shown in Appendix A. Design optimisation was carried out on the thermal insulation and structural components to ensure a lightweight and structurally integral nozzle. To include some form of modularity, the nozzle design was completed for the worst thermal loading case, this being a 40% aluminised fuel grain. The resulting nozzle design can also be used with fuel grains containing a lower aluminium content. The aerodynamic contour would, however, require amendment due to the lower mass flow rates, and minor performance losses associated with an over-expanding nozzle would have to be accepted.

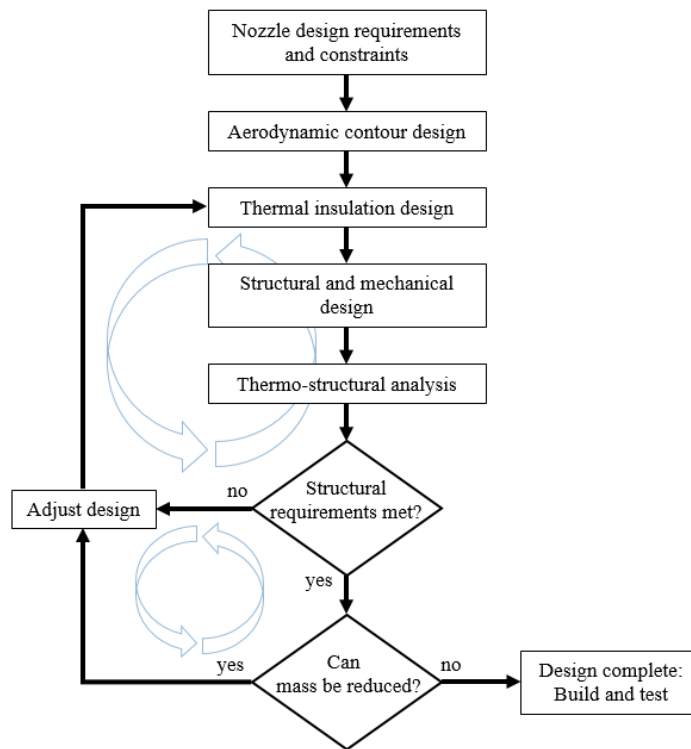


Figure 5.3: Nozzle design methodology used for P1B

5.2.3. Design requirements and constraints

This section describes the selected design criteria from the different variations seen in the NASA (1975) monograph on solid rocket motor nozzles and was based on performance and cost. These constraints were used in the development of the thermal and structural designs. Materials available for the nozzle were silica phenolic, graphite/molybdenum and EN19 steel. Nozzle sections were bonded with room temperature vulcanising silicone (RTV).

Entrance/convergent section

An external entrance was specified for the P1B nozzle to avoid the complexities and high costs associated with submerged nozzles which also suffer from specific impulse losses. Submerged nozzles consist of the throat starting within combustion chamber (shorter overall length), whereas, external nozzles are identified with the classic convergent/divergent profile. External nozzles require an entrance section so as to allow for smooth flow transition to supersonic flow in the throat. The contraction ratio between nozzle and chamber is determined by the chamber diameter. The inlet half-angle of the convergent cone varies from 1° to 75° with 45° being the standard. Steeper inlets are prone to increased insulation erosion especially at higher chamber pressures (NASA, 1975).

Throat

The throat geometry must provide a smooth transition from subsonic to supersonic flow. This requires the use of an upstream circular arc tangent and a downstream circular arc at the geometric throat (Equations (5.5) and (5.6)). A finite cylindrical length at the throat aids in nozzle alignment, machining and erosion mitigation. This cylindrical section must have a length that is half the throat radius or greater (NASA, 1975).

Exit/divergent section

The divergent section of the nozzle must maximise performance without additional length, mass and cost. A contoured divergent section was selected as this is shown to have a 0.5% to 1% improvement in delivered specific impulse over a conical exit (NASA, 1975).

Structure

A design allowance must be made such that the nozzle can be bolted radially to the combustion chamber with O-rings providing a leak-tight seal. This is similar to the bulkhead retention method for the oxidiser tank and injector bulkheads described in Chapter 4 (NASA, 1975).

5.2.4. Nozzle erosion

Nozzle erosion is a complex issue affected by many factors such as propellant composition, motor operating conditions, duration of firing, nozzle geometry and material properties, transport of reacting species, homogeneous reactions in the gas phase and heterogeneous reactions at the nozzle surface (Thakre, 2008). Figure 5.4 illustrates the various erosion-causing mechanisms. As a nozzle throat erodes the expansion ratio changes thus reducing the nozzle's efficiency and consequently reducing rocket performance. These effects have a greater impact in smaller nozzles. Figure 5.4 also illustrates the physiochemical processes that occur within the nozzle and which contribute to nozzle erosion.

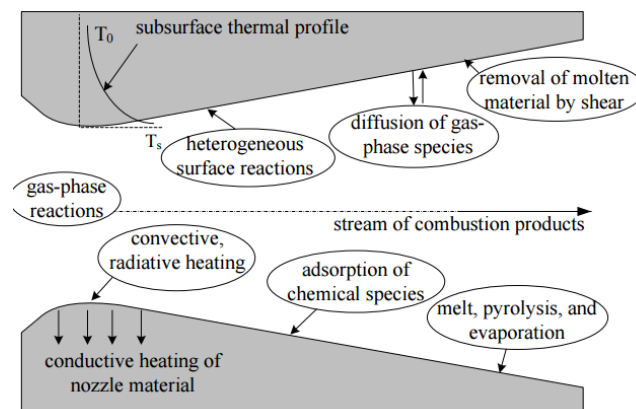


Figure 5.4: Physiochemical processes in a nozzle causing erosion (Thakre, 2008)

5.2.5. Design assumptions

A nozzle must be designed to accommodate real operating conditions and the losses. A list of such losses as adapted from Hrbud (2008) and Seitzman (2012) includes:

- Stagnation pressure loss in the chamber resulting from non-isentropic flow, including heat and mass transfer and friction.
- Divergence and non-uniformity of the exhaust gas caused by two-dimensional flow.
- Boundary layer and wall friction arising from viscous flow effect drag and shock interactions.
- Slip due to multi-phase flow. Liquid and solid particles have higher densities and therefore lower velocities. Interaction between gas and particles slows down the gas due to momentum transfer.
- Transient flow losses.
- Nozzle flow chemical kinetics. As the gas cools in the nozzle the unstable molecules that have a high positive heat of formation re-associate.
- Throat erosion causes a reduction in expansion ratio.
- The impact of real gas properties.
- Non-optimal expansion such as over- and under-expanding flow.

Accommodating all of the above effects in the design of the P1B nozzle was not possible, therefore the following assumptions were adopted:

- The combusted gas is homogenous and adheres to ideal gas law and is isentropic.
- There is no heat transfer between the gas and nozzle to reduce gas thermal energy during expansion.
- There are no friction or viscous boundary layer losses.
- No shocks occur within the nozzle.
- The gas composition is uniform throughout the nozzle.
- Flow is axial and one dimensional with thermo-physical properties being constant across a plane normal to the flow.
- Complete chemical equilibrium in the combustion chamber, resulting in frozen flow in the nozzle, whereby the gas composition is assumed constant during expansion, whereas in equilibrium flow, the gas composition changes during flow expansion.

5.3. Thermo-structural methodology

ANSYS Workbench™ was employed to conduct the one-way coupled thermal-to-structural analysis of the nozzle with the methodology that was employed shown in Figure 5.5. A one-way coupled analysis was conducted as minimal deformation was assumed and this was verified with simulation results. MATLAB™ code (Appendix B) was written to discretise the nozzle contour into stations and determine the thermal and structural variations, temporally and spatially at each station during the motor burn. The transient loadings were then fed into the transient thermal tool of ANSYS™ where the temporally varying thermal gradients throughout the nozzle were found. Transferring this information and mapping each time step to the varying pressure loading into the transient static analysis tool of ANSYS™, resulted in the stress distributions in the structure. Initial axisymmetric analyses were conducted for quick turnaround thus allowing for an iterative process to optimise the thermal design. A three dimensional cyclic symmetry analysis with assembly to the combustion chamber casing was then conducted to verify the design.

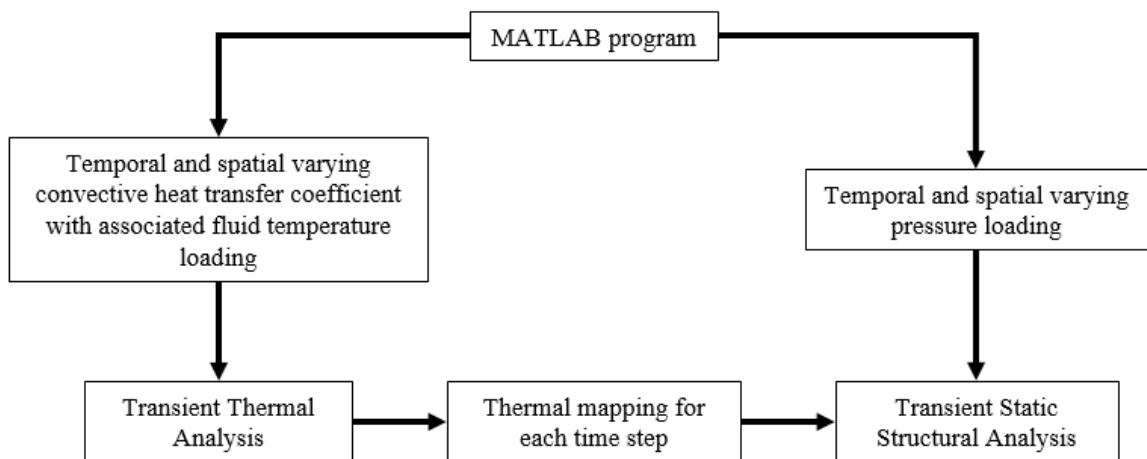


Figure 5.5: Thermo-structural methodology

5.4. Nozzle loading

5.4.1 Aluminised fuel motor specifications

The design specifications of the 40% aluminised paraffin wax fuel grain and nozzle are shown in Tables 5.1 and 5.2. These specifications were used to complete the nozzle design to withstand the excessively high temperatures experienced in aluminised fuel grains. Table 5.3 shows the time-averaged motor performance for the 40% aluminised paraffin wax fuel grain operating with nitrous oxide. Figures 5.6 and 5.7 show the thrust, pressure and temperature time histories from the simulation of the aluminised motor. As seen in Figure 5.7, the temperature of the combusted fuel and oxidiser is initially 3600 K and gradually decreases due to the O/F shift.

Table 5.1: 40% aluminised fuel grain and nozzle specifications

Parameter	Specification	Units
Design thrust	6250	N
Design O/F ratio	3.8	
Design chamber pressure	40	bar
Design atmospheric pressure	101325	Pa
Combustion efficiency	90	%
Burn time	15	s
1st critical pressure ratio	0.9947	
2nd critical pressure ratio	0.2185	
3rd critical pressure Ratio	0.0253	
Characteristic velocity	1643.388	m/s
Thrust coefficient	1.530	
Nozzle throat area	0.0010	m ²
Nozzle exit area	0.0064	m ²
Nozzle exit diameter	0.0901	m
Total oxidiser mass flow rate	2.19	kg/s
Total fuel mass flow rate	0.58	kg/s
Nozzle mass flow rate	2.76	kg/s
Grain length	0.515	m
Grain diameter	0.146	m
Initial grain volume	7.14x10 ³	m ³
Final grain volume	2.3x10 ⁴	m ³
Initial grain mass	8.92	kg
Final grain mass	0.293	kg
Fuel density	1250	kg/m ³
Grain type	Cylindrical Ports	
Number of ports	1	
Initial port diameter	0.06	m

Table 5.2: Nozzle specifications for 40% aluminised fuel grain, nomenclature correlates to Figure 3.20

Parameter	Nomenclature	Specification	Units
Nozzle throat diameter	D_t	0.036	m
Nozzle expansion ratio	ExpRat	6.25	
Nozzle contraction ratio	ConRat	8	
Nozzle contraction angle	Q_c	45	°
Ratio of upstream to throat radius	R_{up}/R_t	1.5	
Ratio of downstream to throat radius	R_d/R_t	0.382	
Nozzle Type	Bell-Shaped Nozzle		
Nozzle parabola inlet angle	Q_n	20.75	°
Nozzle parabola exit angle	Q_e	7.5	°
Nozzle fractional length	L_f	1	
Nozzle half cone angle	Alp_c	15	°
Chamber radius	R_{ni}	0.0510	m
Nozzle throat radius	R_t	0.0180	m
Nozzle exit radius	R_e	0.0451	m
Nozzle upstream radius	R_{up}	0.0270	m
Nozzle downstream radius	R_d	0.0069	m
Nozzle length from inlet to throat plane	L_{ni}	0.0442	m
Length from contraction angle position to throat plane	L_{cx}	0.0191	m
Radius of contraction angle position to throat plane	H_{cx}	0.0259	m
Nozzle total length from throat to exit plane	L_{ne}	0.1018	m
Nozzle parabolic bell length	L_c	0.0994	m

Table 5.3: Time-averaged motor performance parameters for a 40% aluminised paraffin fuel grain

Parameter	Specification	Units
Oxidiser Mass Flow Rate	1.25	kg/s
Fuel Mass Flow Rate	0.41	kg/s
Total Mass Flow Rate	1.65	kg/s
Nozzle Mass Flow Rate	1.65	kg/s
Oxidiser Mass Flux Per Port	169.99	kg/(s.m ²)

Table 5.3 (cont.): Time-averaged motor performance parameters for a 40% aluminised paraffin fuel grain

Fuel Regression Rate	0.002	m/s
Chamber O/F Ratio	2.72	
Chamber Pressure	2377410.81	Pa
Nozzle Exit Pressure	66619.28	Pa
Nozzle Exit Velocity	2241.31	m/s
Nozzle Exhaust Velocity	1814.38	m/s
Characteristic Velocity	1429.93	m/s
Thrust	3414.04	N
Vacuum Thrust	4058.64	N
Momentum Thrust	3634.90	N
Specific Impulse	184.95	s
Vacuum Specific Impulse	253.29	s
Total Impulse	73965.16	Ns

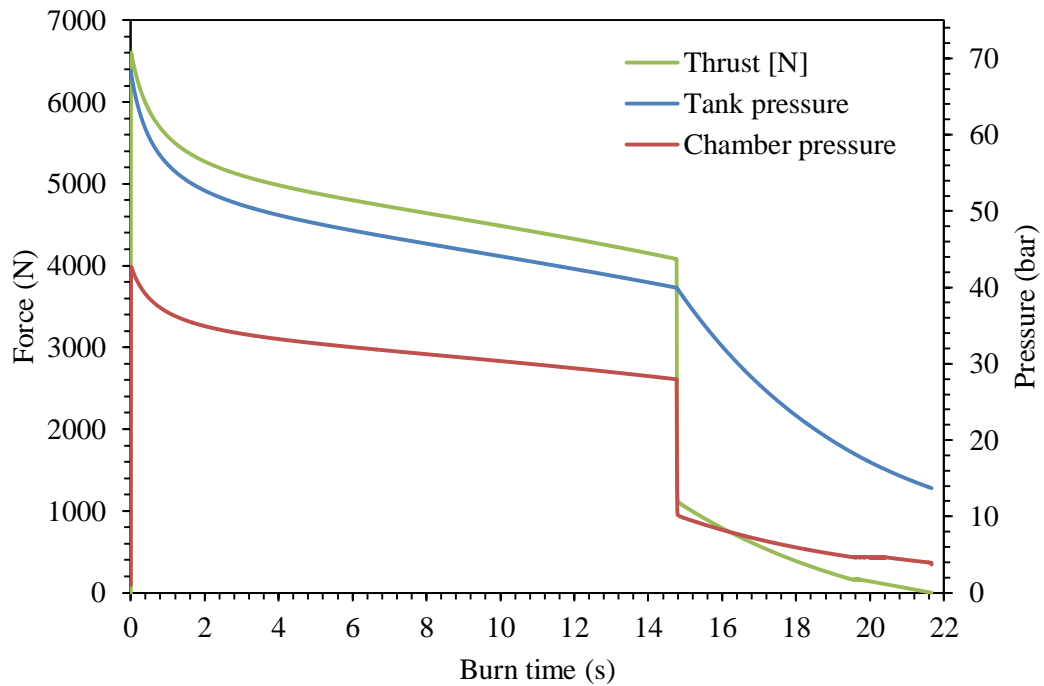


Figure 5.6: Pressure and thrust time traces for 40% aluminised fuel

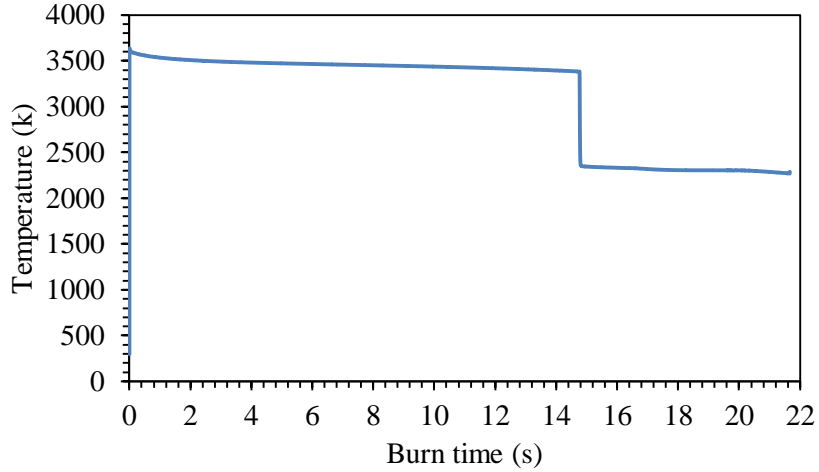


Figure 5.7: Combustion temperature for 40% aluminised fuel grain

5.4.2. Thermal loading

The principle modes of heat transfer to the nozzle walls are convection and radiation. Of these, convection heat transfer dominates with radiation only being considered for particle laden flows. It is known that the aluminised fuel will produce particles in the gas flow and the assumption is made that the gas is homogeneous. Before gases can transfer heat to the wall, the heat energy must pass through the viscous boundary layer against the nozzle wall. The basic correlation for this forced convective heat transfer is expressed as:

$$\dot{q} = h_g(T_{aw} - T_{wg}) \quad (5.10)$$

where \dot{q} is the heat flux transferred across the stagnant gas film per unit surface area, per unit time, h_g is the gas side heat transfer coefficient, and T_{aw} and T_{wg} are the temperatures of the adiabatic wall and hot gas side wall respectively. The adiabatic wall temperature at a given location may be obtained from:

$$T_{aw} = T_0 \left[\frac{1 + r \left(\frac{\gamma - 1}{2} \right) M_x^2}{1 + \left(\frac{\gamma - 1}{2} \right) M_x^2} \right] \quad (5.11)$$

where T_0 is the combustion or stagnation temperature and M_x is the local Mach number along the nozzle flow contour. The local recovery factor, r , represents the ratio of the frictional temperature increase to the increase caused by the adiabatic compression. It may be determined by:

$$r = (\text{Pr})^{0.5} \rightarrow \text{laminar flow} \quad (5.12)$$

$$r = (\text{Pr})^{0.33} \rightarrow \text{turbulent flow} \quad (5.13)$$

A well-known correlation for determining the convective heat transfer coefficient, h_g , across the turbulent boundary layer in a rocket nozzle is the Bartz correlation (Bartz, 1957). Bartz (1965) provides a comprehensive discussion on the formulation of the heat transfer correlation, however, a brief description is provided in this study.

The boundary layer in a rocket nozzle is greatly affected by the turbulent combustion process, the local gas composition and temperature. Combustion gas mass flux greatly influences the convective heat transfer coefficient, a rough approximation of which can be given by:

$$h_g \approx (\rho' U_\infty)^{0.8} \quad (5.14)$$

where ρ' and U_∞ are the free stream local gas density and velocity respectively. Bartz expanded on this approximation by solving the integral momentum and integral energy equations which were based on the definitions of boundary layer displacement, momentum and energy thickness. The integral momentum equation is given by:

$$\frac{d\theta}{dx} = \frac{C_f}{2} - \theta \left[\frac{1 + \frac{\delta^*}{\theta}}{u} \frac{du}{dx} + \frac{1}{\rho u} \frac{d(\rho u)}{dx} + \frac{1}{r} \frac{dr}{dx} \right] \quad (5.15)$$

where $d\theta/dx$ is the change in the momentum boundary layer thickness along the nozzle's axis, with x being the axial distance along the nozzle, C_f is the skin friction based on the wall shear stress, δ^* is the boundary layer displacement thickness, u is the gas the velocity, ρ is the combusted gas density and r is the radius in the nozzle. The integral energy equation is given by:

$$\frac{d\phi}{dx} = C_h \left(\frac{T_{aw} - T_w}{T_o - T_w} \right) - \phi \left[\frac{1}{\rho u} \frac{d(\rho u)}{dx} + \frac{1}{r} \frac{dr}{dx} - \frac{1}{T_o - T_w} \frac{dT_w}{dx} \right] \quad (5.16)$$

where $d\phi/dx$ is the change in the boundary layer energy thickness along the nozzle's axis, C_h is the Stanton number and T_w is the local nozzle wall temperature. The Stanton number is defined as the ratio of the heat transferred into gas to the thermal capacity of the gas and is one of four correlations that was used in determining the Bartz equation. The other correlations are the Nusselt number, Reynolds number and Prandtl number. The Nusselt number (Nu) is defined as the ratio of the convective to conductive heat transfer across a plane normal to the boundary layer.

The ratio of the fluid inertial forces to viscous forces is given by the Reynolds number (Re) and the Prandtl number (Pr) is the ratio of the viscous/momentum diffusion rate to the thermal diffusion rate. These dimensionless numbers are given by:

$$C_h = \frac{q_w}{\rho u C_p (T_{aw} - T_w)} \quad (5.17)$$

$$Nu = \frac{h_g D}{k} \quad (5.18)$$

$$Re = \frac{\rho' U D}{\mu} \quad (5.19)$$

$$Pr = \frac{\mu C_p}{k} \quad (5.20)$$

where q_w is the heat transferred into the gas from the nozzle wall, D is the hydraulic diameter, k is the gas thermal conductivity, μ is the viscosity and C_p is the specific heat at constant pressure. The correlation for these dimensionless numbers for the calculation of the convective heat transfer coefficient is given by:

$$Nu = C Re^{0.8} Pr^{0.34} \quad (5.21)$$

Using the integral method, the shear stresses on the nozzle wall were approximated with a flat plate skin friction formula and the $1/7^{\text{th}}$ power law boundary layer profile. The Bartz equation gives an estimate of the heat transfer coefficient as a function of the local gas temperature and Mach number and is given by:

$$h_g = \left[\frac{0.026}{D_t^{0.2}} \left(\frac{\mu^{0.2} C_p}{Pr^{0.6}} \right)_0 \left(\frac{P_0 g}{C^*} \right) \left(\frac{D_t}{R} \right)^{0.1} \right] \left(\frac{A_t}{A_x} \right)^{0.9} \sigma \quad (5.22)$$

where R is the nozzle radius curvature at the throat, σ is the correction factor for fluid property variations across the turbulent compressible boundary layer and A_x is the local cross section area along the nozzle axis. The correction factor can be established in terms of the nozzle stagnation temperature, local gas-side wall temperature and local Mach number:

$$\sigma = \left[\frac{1}{2} \frac{T_{wg}}{T_0} \left(1 + \frac{\gamma - 1}{2} M_x^2 \right) + \frac{1}{2} \right]^{-0.68} \left[1 + \frac{\gamma - 1}{2} M_x^2 \right]^{-0.12} \quad (5.23)$$

Isentropic and potential flow relations were used to approximate the temperature of the combusted gas along the nozzle wall as it depends on the heat transfer to the nozzle wall. The Prandtl number and viscosity can be calculated with the following relations (Bartz, 1957):

$$\text{Pr} = \frac{4\gamma}{9\gamma - 5} \quad (5.24)$$

$$\mu = (46.6 \times 10^{-10}) MW^{0.5} T^{0.6} \quad (5.25)$$

During the derivation, Bartz made assumptions that were later adopted by Smith (1970) and summarised as follows:

- The gas flow is axisymmetric and steady with only the pressure gradient and skin friction forces acting on the gas.
- The flow is isentropic (reversible and adiabatic).
- The gas through the nozzle is perfect with a constant Prandtl number.
- The skin-friction coefficient and Stanton number are as they would have been on a flat plate at the same nozzle free-stream conditions, wall temperature and momentum thickness.
- The Stanton number for equal momentum and energy thickness was related to the skin-friction coefficient by the von Karman's form of Reynolds analogy which relates the turbulent momentum to the heat transfer.
- The heat transfer has no effect on the skin-friction which is the same as for the adiabatic flow.

A difference exists between the theoretical and experimental convective heat transfer coefficients due to the initial assumptions for analytical calculations. The calculated convective heat transfer coefficient can be lower than the actual value if the following conditions exist:

- Substantial components of the combusted gas are strong radiators (radiation dominated heat transfer).
- There is substantial dissociation with subsequent recombination of molecules in the exhaust stream near the wall.
- There are strong, high frequency flow instabilities. This is related to combustion instabilities.

Alternatively, calculated values can be higher than actual values if:

- Combustion reactions do not reach completion in the combustion chamber or if homogenous and heterogeneous reactions occur in the nozzle.
- Combustion gases deposit solids on the nozzle wall that act as insulators such as slag and charring.
- Boundary layer cooling is used.

In rapidly accelerating compressible flows, the boundary layer thickness may decrease in the flow direction, reaching a minimum at the throat. Evaluation of the Bartz equation also requires the area ratio relationship and isentropic flow equations:

$$\frac{A_x}{A^*} = \frac{1}{M_x} \sqrt{\left[\frac{2}{\gamma + 1} \left(1 + \frac{\gamma - 1}{2} M_x^2 \right) \right]^{\frac{\gamma + 1}{\gamma - 1}}} \quad (5.26)$$

$$T_x = T_0 \left(1 + \frac{\gamma - 1}{2} M_x^2 \right)^{-1} \quad (5.27)$$

The role of the Bartz equation in the thermo-structural analysis carried out for this study is illustrated in the modelling flow chart given in Figure 5.8.

5.4.2. Structural loading

The structural loading on the rocket nozzle is mainly due to the pressure distribution of the expanding gases within the nozzle. This is assuming that there are no side loads imparted due to off-axis thrust and thrust misalignment. The pressure distribution is given by the isentropic flow equation:

$$\frac{P_0}{P_x} = \left[1 + \frac{\gamma - 1}{2} M_x^2 \right]^{\frac{\gamma}{\gamma - 1}} \quad (5.28)$$

5.4.3. Temporal and spatial modelling

Computing the Bartz equation as well as the free stream flow properties via compressible isentropic flow equations at each point or ‘station’ in the nozzle results in a spatial variation of convective heat transfer, temperature and pressure as seen in Figures 5.8 and 5.9 respectively. A constant specific heat ratio is assumed through the nozzle but not over time. Changes in combustion chamber gas properties and O/F ratio during the burn are retrieved from the HRPC performance simulation. Information is read at chosen time increments depending on time steps

needed for the thermo-structural analysis. Inputting O/F ratio, chamber pressure and combustion temperature into NASA CEA results in the output of transport properties such as the gas viscosity, Prandtl number and pressure specific heat. Temporal variations are achieved by evaluating this process for each time step. The spatial and temporal calculations are assessed in a MATLAB™ program, whose logic flow is depicted in Figure 5.10. Modifications to the nozzle geometry, including the throat diameter and cylindrical section, are made possible by discretising the CAD-derived contour. Each file that is generated from the code represents one time step. Results from this code can be seen in section 5.5. These files are then transferred into the ANSYS™ thermal and structural tools to conduct the transient thermo-structural analysis.

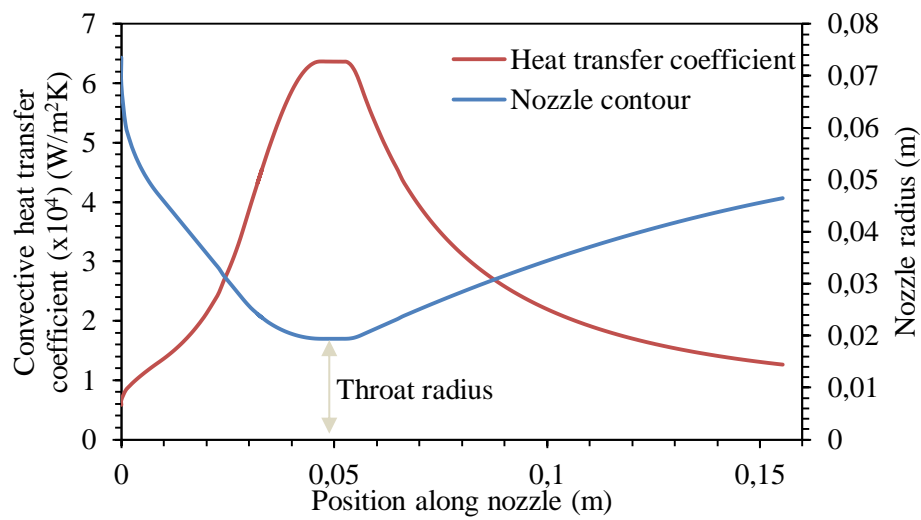


Figure 5.8: Convective heat transfer coefficient along nozzle contour at instantaneous 40 bar chamber pressure

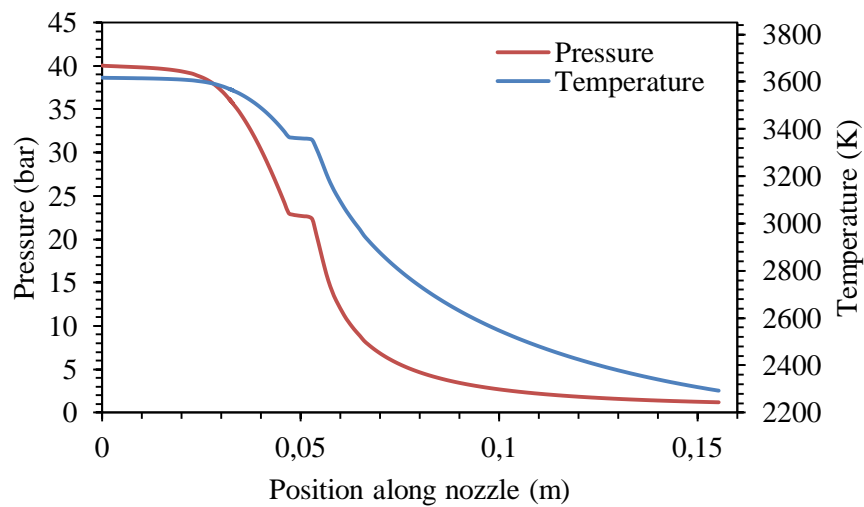


Figure 5.9: Pressure and temperature variation along nozzle contour at instantaneous 40 bar chamber pressure

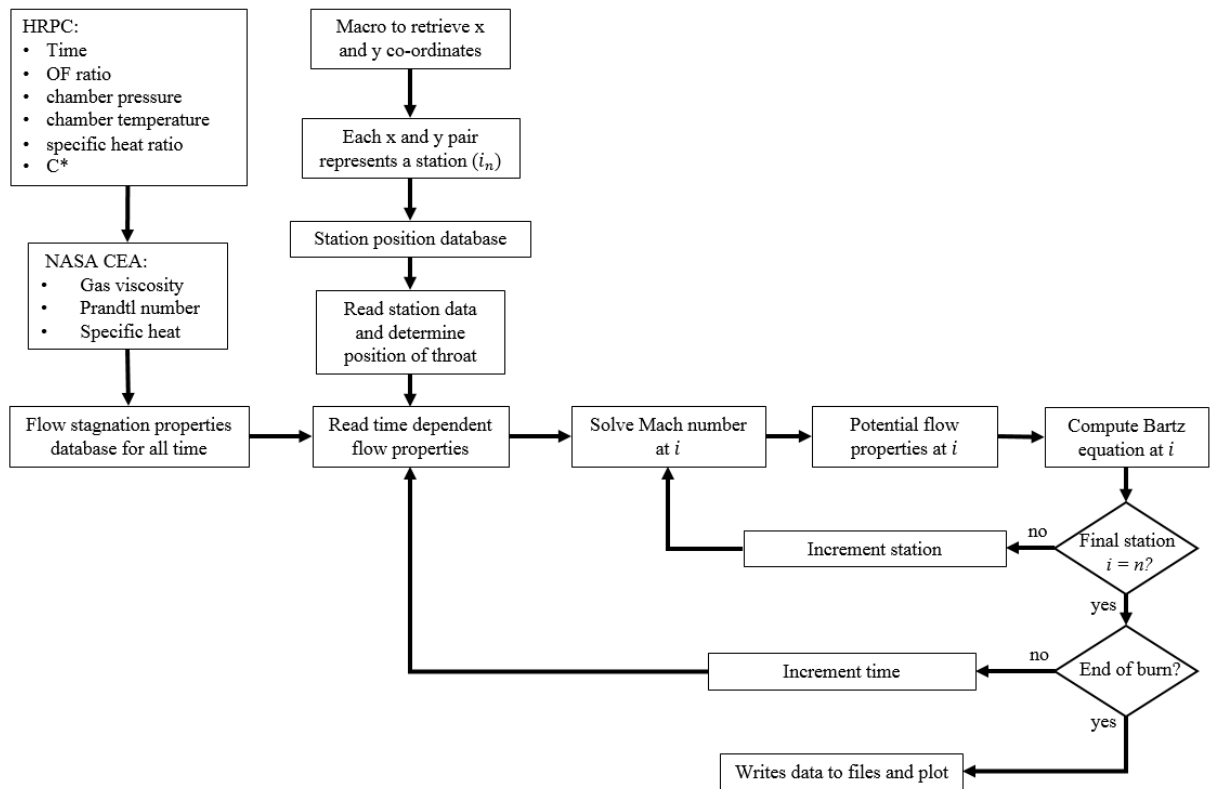


Figure 5.10 : Temporal and spatial modelling methodology

5.5. Thermo-structural analysis

5.5.1. 40% Aluminised fuel grain nozzle design

The final design of the nozzle for an aluminised fuel grain is shown in Figure 5.11. The nozzle consists of five components namely, the convergent section, divergent section, throat, structure and retaining ring. The convergent and divergent sections were made from tape-wrapped silica phenolic composites. Graphite was selected for the throat due to the high gas temperatures and EN19 steel was used for the structure and retaining ring. M6 bolts are used to fasten the retaining ring to the structure. This assembly forms a mechanical constraint for the divergent section. During fabrication, all components of the nozzle were bonded with RTV silicone. Allowance for a 0.2mm bond gap was made between components to ensure sufficient adhesion. The tapering of the outer graphite throat surface forms a mechanical locking mechanism restraining the throat in place while the use of dimples (Figure 5.12) between the structure and convergent section, and between the divergent and convergent sections, allow for mechanical locking. They also increase the gas path length and the convergent section bond area. The nozzle is bolted to the combustion chamber with twenty M8 bolts and sealing is achieved with two O-rings. The temporal and spatial variations in loading are seen in Figures 5.13 to 5.15, where the station number represents the

discrete points along the nozzle axis. The sharp change in the loadings at 15 s corresponds to the depletion of liquid nitrous oxide.

In the case of the 40% aluminised motor, 15 s of burn were simulated, corresponding to liquid depletion. The heat transfer from gaseous nitrous oxide combustion with the fuel is significantly lower than that of liquid injection, as shown in Figures 5.13 to 5.15. One second increments were chosen which resulted in fifteen files being transferred to ANSYS™.

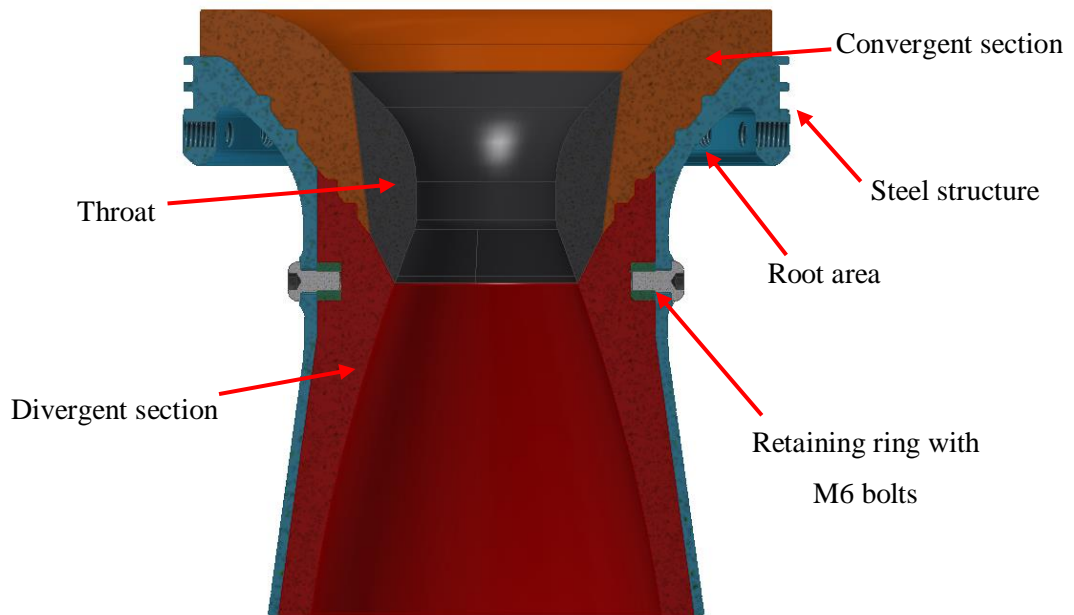


Figure 5.11: Cross section of the final nozzle design for 40% aluminised fuel grain motor

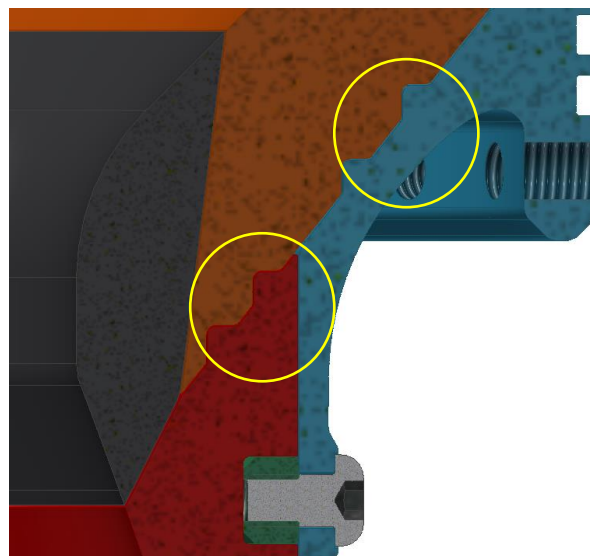


Figure 5.12: Close-up of nozzle showing dimples

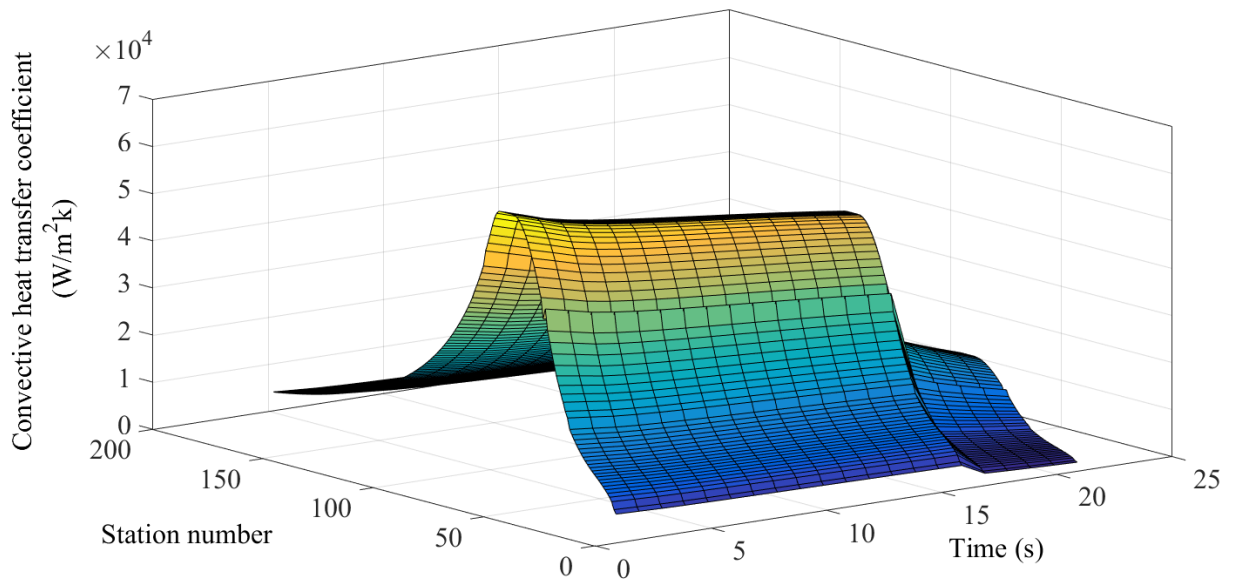


Figure 5.13: Spatial and temporal convective heat transfer coefficient distribution through the nozzle for a 40% aluminised grain.

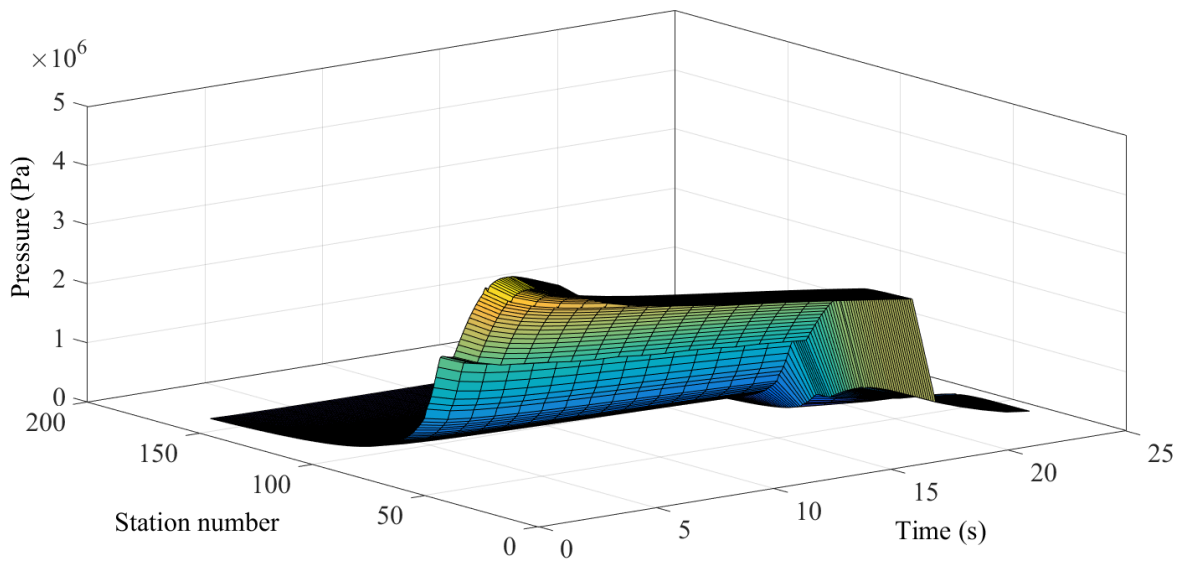


Figure 5.14: Spatial and temporal pressure distribution through the nozzle for a 40% aluminised grain.

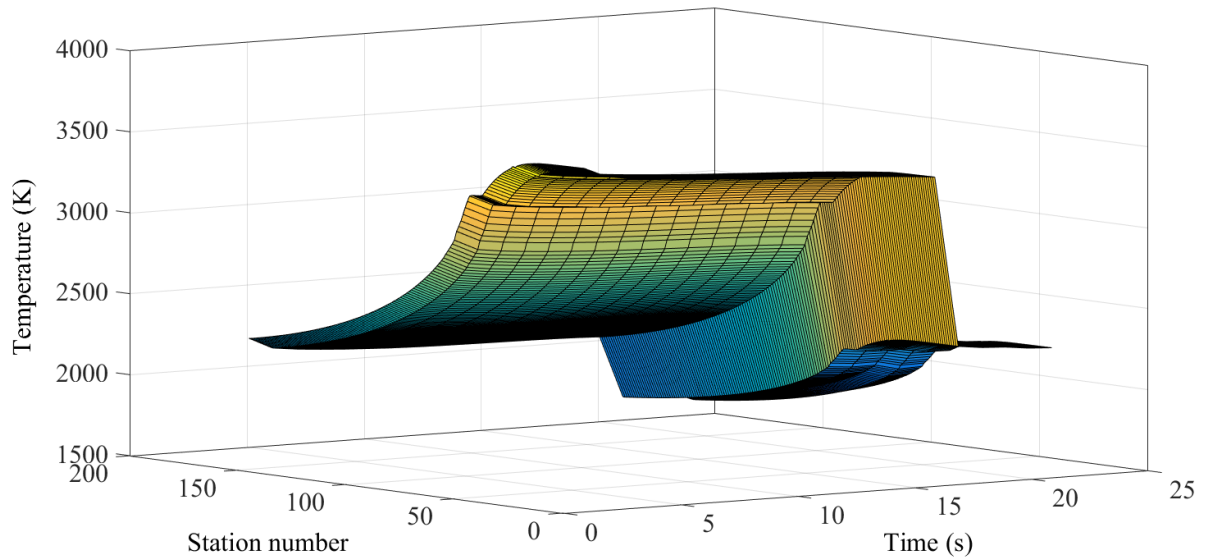


Figure 5.15: Spatial and temporal temperature distribution through the nozzle for a 40% aluminised grain.

5.5.2. 2D axisymmetric analysis

The temperature distribution at the end of the burn for the 40% aluminised nozzle is shown in Figure 5.16. Insulation was designed to ensure that the steel structure did not exceed high temperatures in structurally sensitive areas such as at the root area (Figure 5.11). This component has to endure the full pressure loading and thermal stresses induced by the expanding insulation. Design of the insulation, graphite throat and structure was carried out with the flow contour in mind and the thicknesses were found iteratively. For this 2D case, a bonded constraint was applied to the bolted regions as well as the insulation and graphite throat. A friction constraint was applied between the nozzle structure and aluminium combustion chamber with a frictionless constraint being applied on the combustion chamber casing to only allow radial movement. The 2D nature of the design allowed for extremely fine mesh generation and, instead of conducting mesh independence studies, the mesh analyser provided by ANSYS™ was used to monitor and adjust mesh settings. This was done for both the 2D and 3D cases. A mesh size of 0.35 mm was used in the axisymmetric analysis which resulted in 223902 nodes and 71693 elements. The mesh was refined at the interface between components to properly capture the thermal gradients.

The effect of the RTV adhesive was considered as part of the study. A thermal resistance corresponding to that of the adhesive was set between bonded interfaces. Thermal modelling results can be seen in Figure 5.17. The maximum temperature on the structure as well as the depth of thermal penetration is lower in the RTV case.

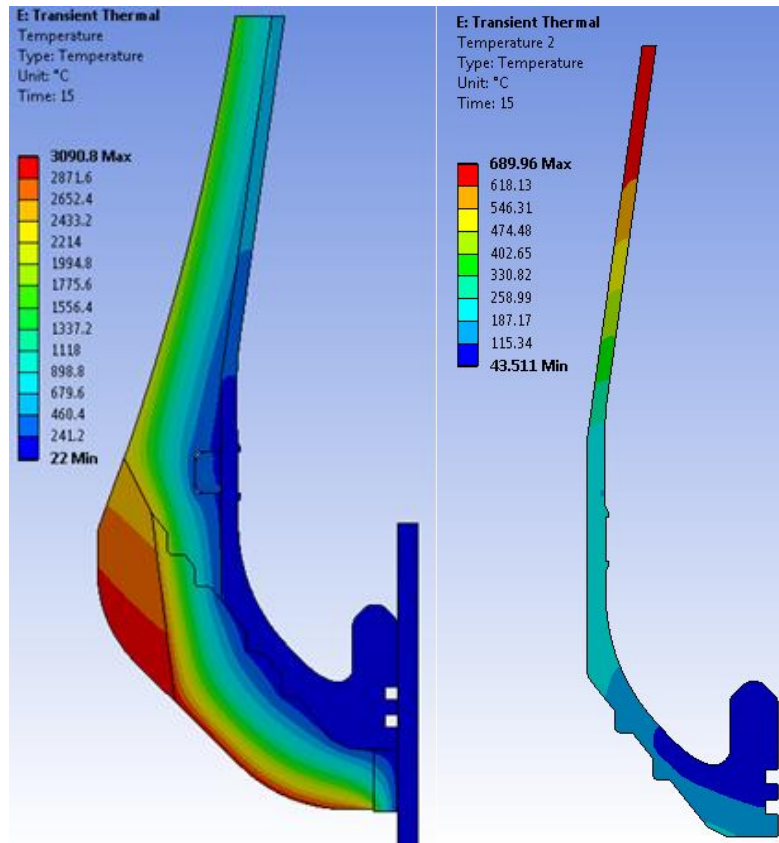


Figure 5.16: Temperature distribution in the nozzle insulation components (left) and in the structure (right)

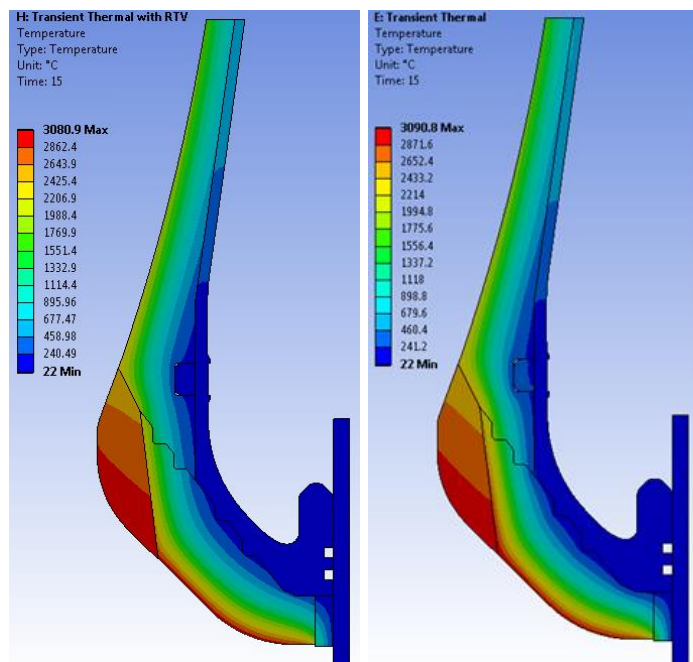


Figure 5.17: Temperature distribution at end of burn for the model including RTV adhesive (left) and the simplified case (right)

5.5.2. 3D cyclic analysis

After finalising the thermal design of the nozzle, the model was analysed in a 3D transient thermal and transient structural analysis. By slicing it into periodic sectors with periodic bolts, as shown in Figure 5.18, ANSYS Workbench™ was used to conduct the cyclic symmetrical analysis. As with the 2D case, all components of the insulation were bonded to each other and to the steel structure and a frictional contact was applied between the steel structure and the aluminium combustion chamber casing. The thread between the steel structure and bolt was modelled including friction between the bolt and the combustion chamber casing.

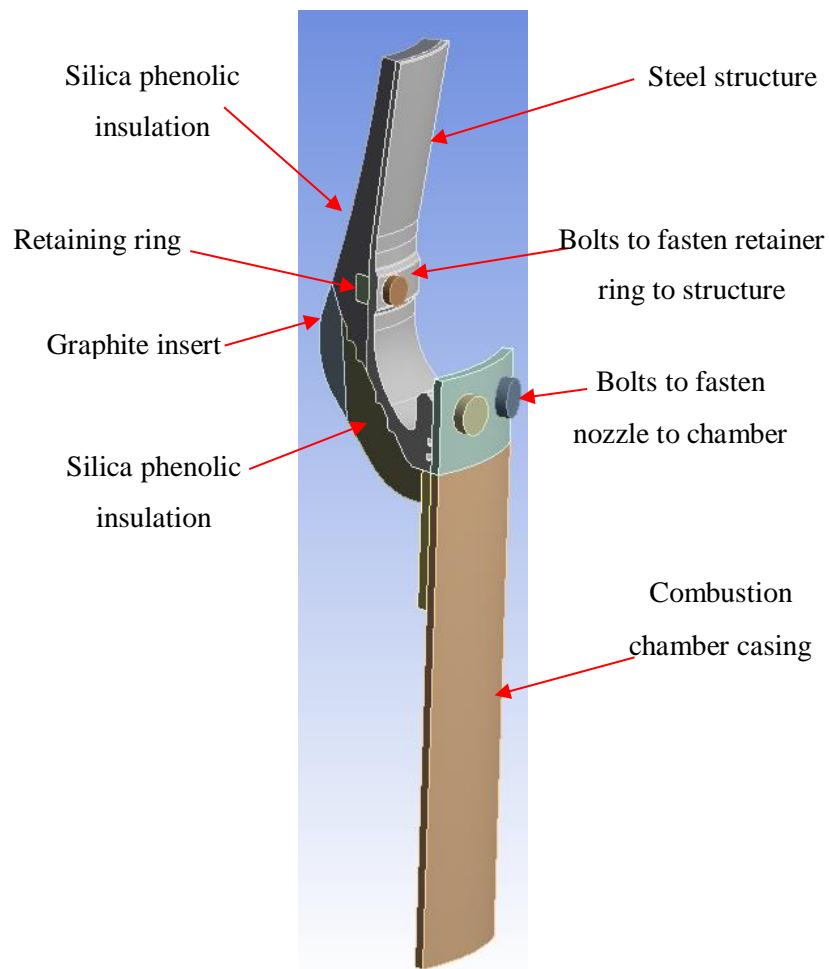


Figure 5.18: Cyclic symmetry 3D model for final thermo-structural analysis

One parameter that can be considered when generating the mesh for a thermal analysis is the Biot number (Bi), which is defined as the ratio of the convective heat transfer to the thermal conductivity of the solid and is given by:

$$Bi = \frac{h_g L_c}{k} \quad (5.25)$$

where L_c is a characteristic length. A qualitative analysis using this relationship shows that the conductive heat transfer of the nozzle materials is significantly lower than the convective heat transfer. This meant that the mesh for the thermal analysis had to be extremely dense to prevent non-convergence and negative temperature results. The mesh was refined until the minimum temperature residual converged and yielded sensible results. Another method to improve the residuals was the use of linear elements instead of quadratic where the mid-nodes of the elements were dropped. This resulted in a node count of 1048638 and element count of 2017938 for the thermal analysis. The average element quality was 84% and was deemed acceptable. Careful scrutiny indicated that lower quality elements showed regions of low thermal and stress gradients.

The fine mesh used in the thermal analysis could not be transferred directly to the structural side due to limited computational resources and the requirement of quadratic elements to sufficiently capture model deformation. Dissimilar mesh mapping was therefore employed to transfer the transient thermal loads to the structural simulation. The transient structural mesh consisted of 1462171 nodes, 923431 elements and an average mesh quality of 83%. In both thermal and structural simulations, the mesh was refined in regions of contact. As in the 2D case, RTV thermal resistivity was applied to the 3D analysis.

Figures 5.19 and 5.20 show the temperature and Von Mises stress distributions respectively. An animation of the results is supplied in Appendix D.3 and D.4. It is seen that there is a high stresses initially, due to the sudden thermal and pressure loading experienced by the nozzle at the beginning of the burn. The stresses then decrease before rising for the remainder of the burn. Stress concentrations that are higher than the yield of EN19 are noticed near the end of the burn, however the stresses are lower than the ultimate tensile strength of the material. This was deemed acceptable as the nozzle can be used only once due to the silica phenolic ablation. Deformation near the end of burn is unlikely to affect performance.

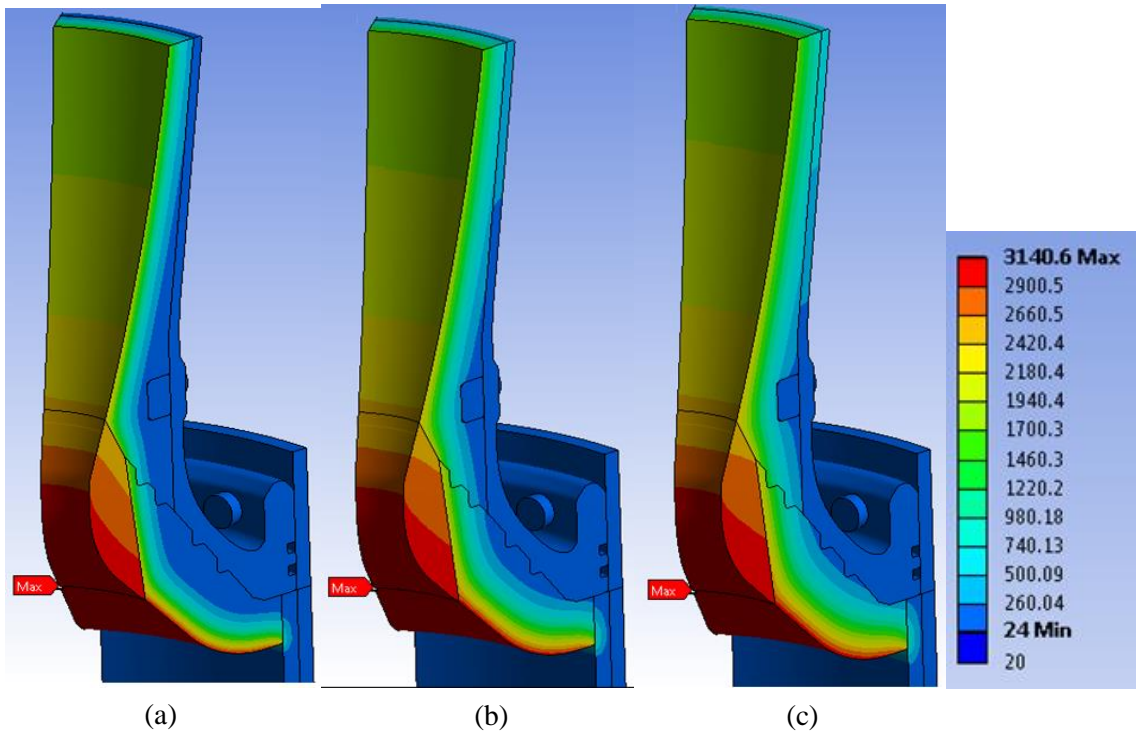


Figure 5.19: Temperature distribution at (a) 5 s, (b) 10 s and (c) 15 s

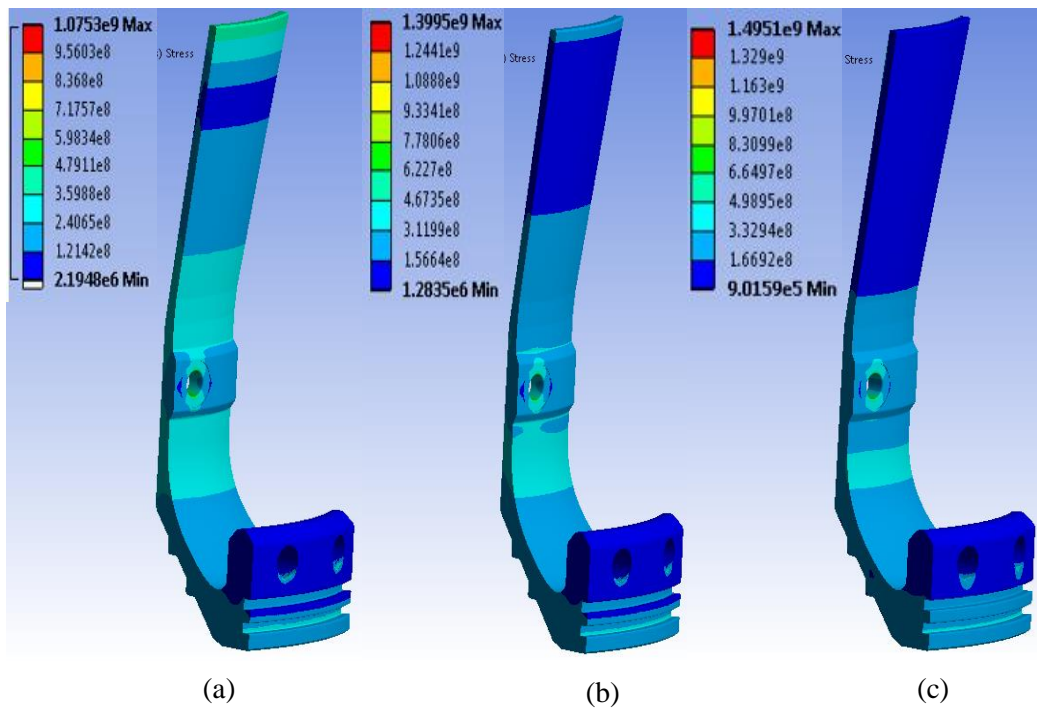


Figure 5.20: Von Mises stress distribution on nozzle structure at (a) 5 s, (b) 10 s and (c) 15 s

5.6. Discussion

The first iteration of P1B is intended to use pure paraffin fuel without aluminium additives. Nevertheless, the nozzle has been designed such that the steel structure can be used in motors with different aluminium loading, up to a maximum of 40% by mass. To ensure optimal expansion, the flow contour will have to be amended. In the case of pure paraffin, the mass flow rate is lower (comparing Tables 5.1 and 3.4) and consequently a lower convective heat transfer is expected, as shown in Figure 5.21. The lower propellant mass flow rate requires a smaller throat diameter than the aluminised motor, while the expansion ratio dictates that a thicker insulation be used for the same nozzle structure. The changes would result in a non-optimal nozzle design for lower aluminium loadings, which is considered acceptable in the context of the HSRP.

The nozzle components for the pure paraffin wax motor have been manufactured and are shown in Figure 5.22. The retaining ring was split in half so that it can be bonded in the machined groove of the divergent section. Prior to bonding, the steel structure was sand blasted to provide a rough surface to aid in adhesion of the RTV. The composite components were chemically cleaned to remove any residual oils. Figure 5.23 shows the assembled and bonded nozzle. The silica phenolic and retainer ring components were bonded with RTV first and after curing the graphite throat was added. Water proof lacquer was then applied to avoid moisture ingress.

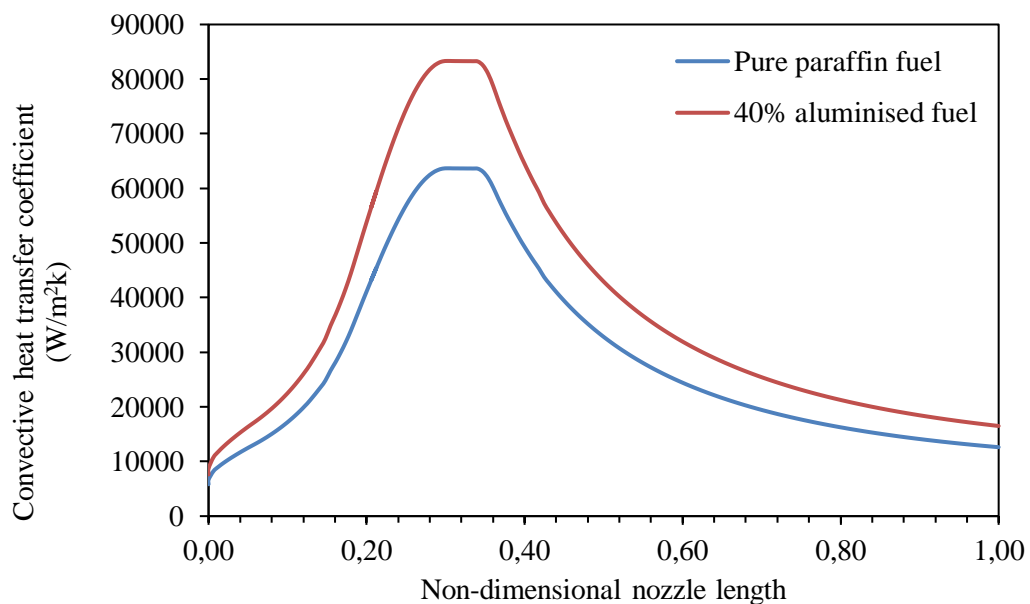


Figure 5.21: Comparison of convective heat transfer between 40% aluminised fuel and pure paraffin fuel at 40 bar chamber pressure



Figure 5.22: Manufactured P1B nozzle components



Figure 5.23: Completed P1B nozzle with bonded components

5.7. Summary

This chapter described the approximate Rao method used to generate the contour of the nozzle divergent section for P1B. This was executed in HRPC to obtain the geometric points that were used in the CAD model. A comprehensive design process was employed to ensure the mitigation of the nozzle failure as seen with P1A in Chapter 2. The nozzle design and analysis methodology consisted of two iterative loops to optimise the thermal and structural design and to minimise the nozzle's mass. Significant research has gone into the development of nozzle for solid rocket motors and so similar techniques were used in the design of the nozzle for the P1B hybrid rocket. To ensure the structural integrity of the nozzle, an iterative transient thermo-structural analysis was completed which consisted of both a 2D axisymmetrical and 3D cyclically-symmetrical analyses. The 2D transient thermal analysis was used to verify the thicknesses of the graphite throat insert and the silica phenolic convergent and divergent sections. The iterative process was carried out such that the temperature at the nozzle structure root was not high enough to cause the material to weaken. Deformation, seen in the 3D case at the end of burn, was accepted as the nozzle is not meant to be re-used. The nozzle was designed for the worst thermal loading case which is the 40% aluminised grain, and by modifying the flow contour, the same design can be used with fuel grains that have a lower aluminium content. The final design was manufactured which involved the bonding of the silica phenolic insulation (convergent and divergent sections) and graphite throat insert to the steel structure.

6. Phoenix-1B Injector Design and Analysis

6.1. Introduction

This chapter discusses the design of the P1B injector that supplies the combustion chamber with the required N_2O flow rate of 1.9 kg/s at peak operating conditions, as described in Chapter 3. Given the performance of P1A and the issue of combustion instabilities, as described in Chapter 2, a correct injector design can lead to the mitigation of combustion instabilities for P1B. The physiochemical properties of nitrous oxide adds complexity to the accurate determination of the mass flow rate. Analytical models attempt to resolve this, however from literature, CFD analysis results have been shown to have a better correlation to actual mass flow rates.

6.2. Injector design

6.2.1. Combustion instabilities in hybrid rocket motors

The problem of combustion instability often occurs during the development of a rocket propulsion system, as seen with P1A. Large chamber pressure spikes and thrust oscillations are the result of combustion instabilities that impart large vibrational loads on the rocket. In some cases these cause structural damage to the vehicle and it is therefore paramount that instabilities be minimised.

Instabilities can be categorised into two groups, namely, high frequency (acoustic) and low frequency (non-acoustic) (Waxman, et al., 2014). Acoustic instabilities form when there is a resonance between energy release from the combustion process and the natural acoustic modes of the chamber cavity. There are three natural acoustic mode types: radial, tangential and longitudinal.

The primary non-acoustic instabilities in a hybrid motor are based on a complex coupling of thermal transients in the solid fuel grain, wall heat transfer blocking (blocking factor) due to the regression rate, and transients in the boundary layer that is formed on the fuel surface (Karabeyoglu, et al., 2005). These instabilities have been observed in both liquid and gaseous oxidiser hybrid propulsion systems (Karabeyoglu, et al., 2007) and are synonymous with large L/D motors, where L is the length of the fuel port and D is the port diameter (Morita, et al., 2013). One of the mechanisms that generate low-frequency instabilities is the coupling of the thermal lags, the gas-phase combustion, and the gas dynamics in the combustion chamber. Karabeyoglu et al. (2005) gives an in-depth description and development of associated mathematical models in an attempt to characterise low frequency combustion instabilities and calculate the time lags

associated with fuel and oxidiser vaporisation and reactions. A simple correlation for the frequency (f) of primary hybrid rocket motor oscillations is given by:

$$f = 0.2341 \left(1 + \frac{1}{O/F} \right) \frac{G_0 RT_{av}}{LP_C} \quad (6.1)$$

where O/F is the oxidiser to fuel ratio, G_0 is the oxidiser mass flux, RT_{av} is the average gas constant and temperature product which has a value of $4.47 \times 10^5 \text{ (m/s)}^2$ for nitrous oxide, L is the fuel port length and P_C is the average chamber pressure.

The second low frequency type is termed the feed system coupled instability (FSCI) and this is of interest in the present work with regard to the injector and feed system. FSCI's are the result of hydrodynamic communication between the combustion chamber and feed system and are mainly seen in liquid oxidiser systems. The mechanisms and phenomena that promote FSCI are (Waxman, et al., 2014) (Karabeyoglu, et al., 2007):

- Time lags associated with combustion and vaporization of the fuel and oxidiser.
- Oxidiser mass flow rate that is dependent on the chamber pressure.
- Compressibility of the fluid in the feed system.

According to Waxman et al. (2014), the following design considerations are necessary to suppress or eliminate FSCI:

- Fuel and oxidiser vaporisation must occur rapidly.
- Enhance atomisation characteristics to minimise vaporisation time.
- Make use of a large length to diameter ratio for the orifice to ensure reattachment of the flow after the vena contracta.
- Short feed system must be used so as to decrease compressibility of the oxidiser.
- The system must be designed for a high injector pressure drop or the chamber pressure should be decreased.
- If possible, an isolating element should be used to impede the hydrodynamic communication upstream of the chamber. An isolating element is a feed system component that enables the oxidiser mass flow rate to be independent of the pressure differential between the oxidiser tank and combustion chamber. An example of this component is a cavitating venturi that has been used in liquid oxygen feed systems.

6.2.2. Injector type

There are three common injector types, namely, axial, impinging and swirl. Swirl injectors increase oxidiser residence time but impart swirl in the exhaust plume, which may cause off-axis thrust. Impinging injectors have been shown to suffer from combustion instabilities as seen in Figure 6.1. Figure 6.2 shows the pressure time traces for the same motor as in Figure 6.1 but with an axial injector.

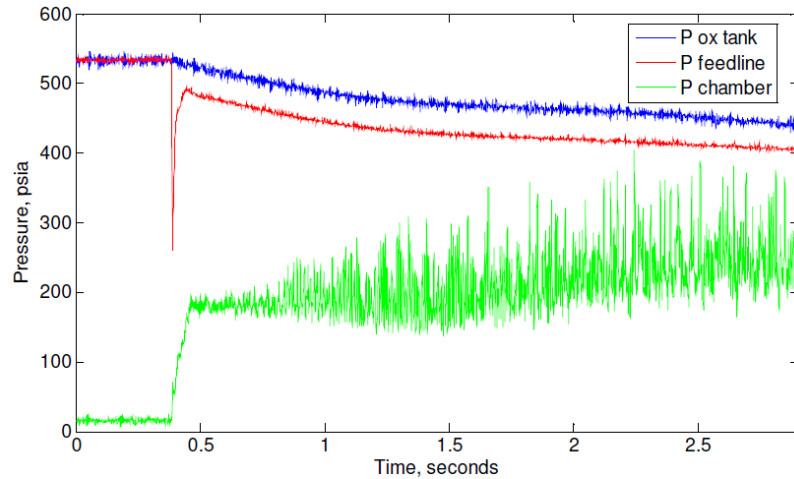


Figure 6.1: Pressure time traces of hot fire with impinging injector (Waxman, et al., 2010)

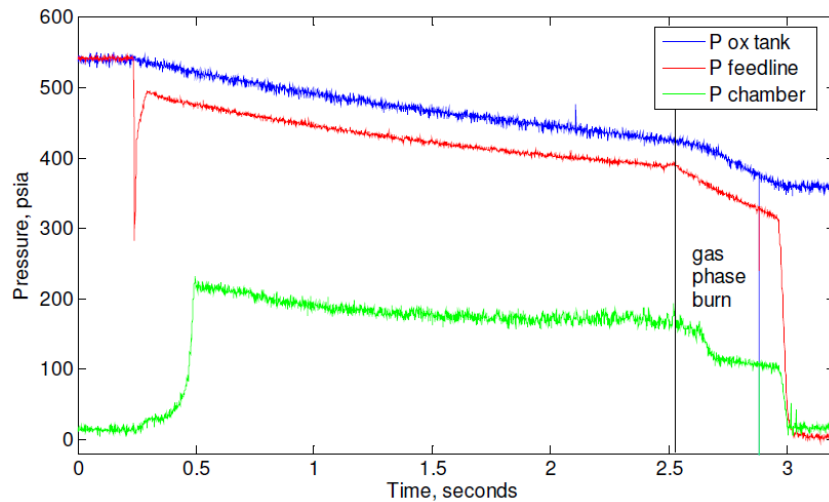


Figure 6.2: Pressure time traces of hot fire with axial injector (Waxman, et al., 2010)

A reason for the reduced instabilities with the axial injector is the presence of a hot gas re-circulation zone, illustrated in Figure 6.3. The recirculating hot gas heats up the incoming oxidiser which aids in vaporisation. With the impinging injector this hot gas re-circulation zone is either diminished or non-existent (Sutton and Biblarz, 2001).

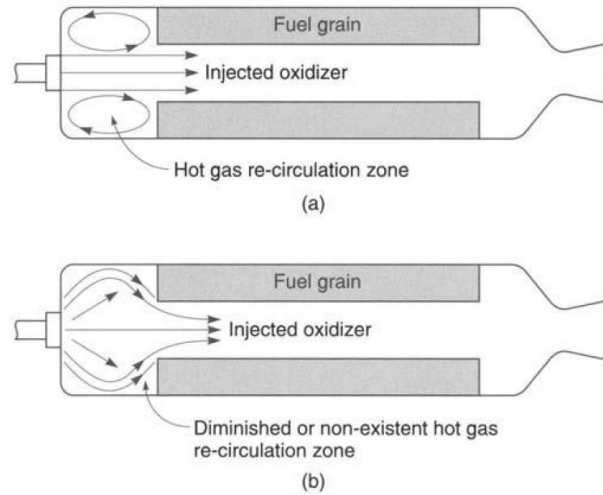


Figure 6.3: (a) Axial injection and (b) impinging injection in a hybrid rocket motor (Sutton and Biblarz, 2001).

Increasing the number of small injector holes assists in rapid vaporisation and atomisation of the incoming fluid, thereby reducing the associated time lags and negating combustion instabilities (Waxman, et al., 2010).

Fine atomisation of the incoming oxidiser aids in the mitigation of low frequency combustion instabilities by minimising the vaporisation time lag. There are three non-dimensional numbers that can be used to describe the atomisation of a fluid through an orifice. The first is the Reynolds number, the second is the Ohnesorge number and the third is the Weber number. The Ohnesorge number compares the influence of the fluid viscosity to the forces of the droplet formation and the Weber number compares the inertial forces to the surface tension between liquid and gaseous phases. Due to the interaction between the fast liquid ejected from the injector and the surrounding gas in the chamber the Weber number is suggested to be greater than 50 for fine atomization to occur (Gamper, et al., 2013). The Ohnesorge (Oh) and Weber (We) numbers are given by:

$$Oh = \frac{\eta}{\sqrt{\rho\sigma d}} \quad (6.2)$$

$$We = \frac{\rho u^2 d}{\sigma} \quad (6.3)$$

where η is fluid's viscosity, σ is the surface tension of the liquid, ρ is the density, u is the velocity and d is the orifice diameter. The orifice diameter of one of the holes in the PIB injector plate was selected to be one millimetre to provide adequate atomisation without using expensive tools to machine smaller holes.

6.3 Mass flow rate modelling

The thermo-physical nature of nitrous oxide adds complexity to mass flow rate modelling in hybrid motors. This is because at operating conditions, nitrous oxide exists as two phases (liquid and vapour) and is fairly compressible as given in Figures 6.4 to 6.6. It can also be seen that increasing the temperature results in more vapour formation and thus increases the vapour pressure. The main advantage of nitrous oxide is its self-pressurisation ability as illustrated in Figure 6.4. At room temperature, N₂O has a sufficient vapour pressure (~50 bar) to feed the liquid oxidiser to chamber without the use of addition pressurisation tanks and complex control systems, however, due to its thermo-physical properties, nitrous oxide rapidly decomposes at 36°C, which results in a near instantaneous pressure rise.

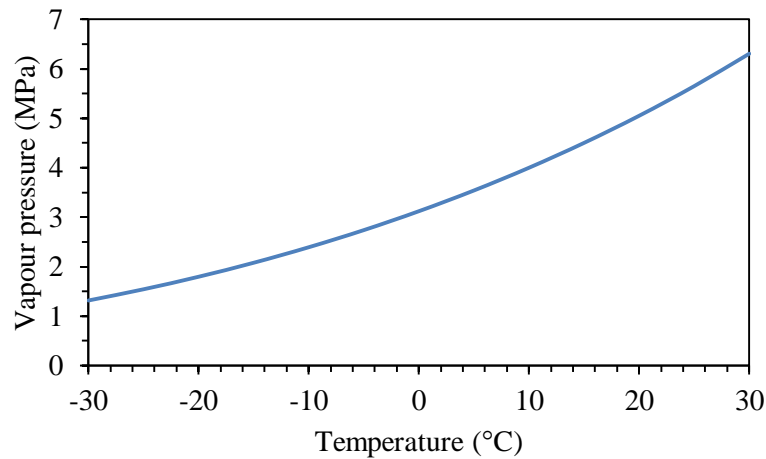


Figure 6.4: Nitrous oxide vapour pressure vs temperature

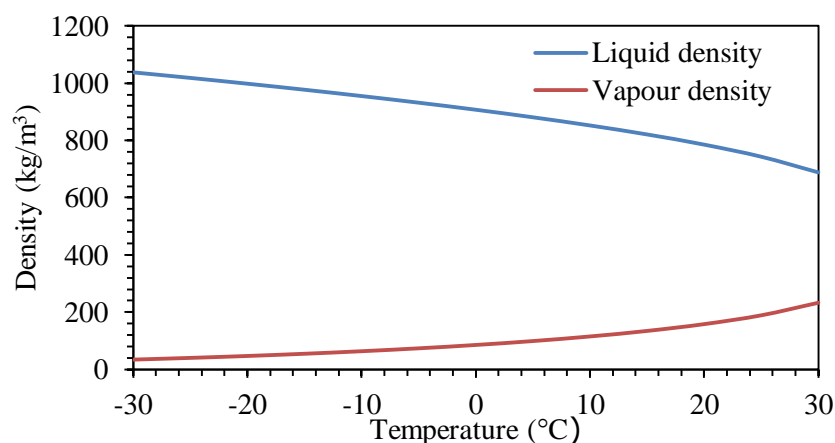


Figure 6.5: Nitrous oxide density vs temperature

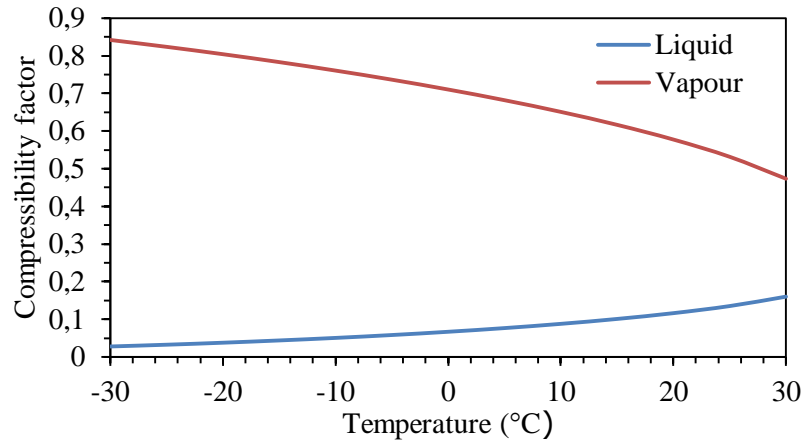


Figure 6.6: Nitrous oxide compressibility factor vs temperature

There are three methods that attempt to predict the mass flow rate of nitrous oxide through an injector (Soloman, 2011; Waxman, 2014). With reference to Figure 6.7, the standard incompressible liquid model is given by:

$$\dot{m}_{incom} = N_{inj} C_d A_{inj} \sqrt{2\rho_1(P_1 - P_2)} \quad (6.4)$$

where C_d is the orifice discharge coefficient, A_{inj} is orifice cross sectional area, N_{inj} is the number of orifices, ρ_1 is the upstream flow density, and difference between P_1 and P_2 is the pressure differential across the injector. This model is only applicable when the compressibility of the flow is near zero.

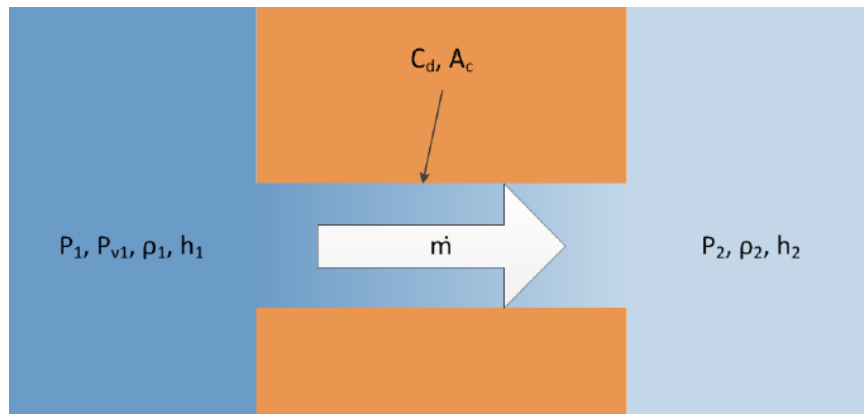


Figure 6.7: Injector orifice cross section defining flow parameters (Soloman, 2011)

A second method is the homogenous equilibrium model (HEM) which attempts to account for the formation of bubbles and vapour pockets resulting from the fluid flashing to vapour as it expands through the injector. The model assumes that:

- Phase change is isentropic.
- There is thermodynamic equilibrium between the liquid and vapour portions.
- No velocity difference exists between the phases.

The model is given as:

$$\dot{m}_{HEM} = N_{inj} C_d A_{inj} \rho_2 \sqrt{2(h_1 - h_2)} \quad (6.5)$$

where ρ_2 is the downstream fluid density and $(h_1 - h_2)$ is the change in enthalpy across the injector.

The third variant is a combination of the incompressible flow model and HEM, and is named the non-homogeneous non-equilibrium model (NHNE). This adds a weighting to each of the other models through a non-equilibrium parameter, κ , which is given by the ratio of the bubble growth time (τ_b) to the residence time of the fluid in the injector (τ_r) as given by Equation (6.6). Equations (6.7) and (6.8) can be used to calculate the time parameters and are combined to form Equation (6.9),

$$\kappa = \frac{\tau_b}{\tau_r} \quad (6.6)$$

$$\tau_b = \sqrt{\frac{3}{2} \frac{\rho_L}{P_{v1} - P_2}} \quad (6.7)$$

$$\tau_r = L \sqrt{\frac{\rho_L}{2\Delta P}} \quad (6.8)$$

$$\kappa = \sqrt{\frac{P_1 - P_2}{P_v - P_2}} \quad (6.9)$$

where ρ_L is the fluid density, P_{v1} is the upstream vapour pressure, L is the length of the injector orifice and P_1 and P_2 are the upstream and downstream static pressures respectively. The NHNE model is given by Equation (6.10) and accounts for the fact that when the residence time of the bubbles is significantly less than the characteristic time for bubble growth, a small amount of

vapour will be formed at the exit and the incompressible model is valid. However, when the bubble time is less than the residence time, then the flow rate can be predicted by the HEM model. This occurs in injectors with large length-to-diameter ratios.

$$\dot{m}_{NHNE} = C_d A_{inj} N_{inj} \left[\left(1 - \frac{1}{1 + \kappa} \right) \dot{m}_{incom} + \frac{1}{1 + \kappa} \dot{m}_{HEM} \right] \quad (6.10)$$

One of the main problems with the above models is that the discharge coefficient varies due to uncertainty associated with nitrous oxide. Cold flow tests must be completed to fully characterise the injector design, and validate the mass flow rate calculations (Waxman, et al., 2013).

6.4. Two phase CFD and final design

In order to determine the number of holes on the axial injector a two-phase VOF (volume of fluid) CFD analysis was carried out, in conjunction with the application of the mass flow rate models in section 6.3. Holes of diameter 1 mm were selected for the PIB injector so that the static pressure within each orifice drops below the vapour pressure, thus cavitating the oxidiser and flashing it from liquid to vapour, which is known as an isolating element. Other than impeding the hydrodynamic communication upstream of the chamber, the selected orifice diameter aids in oxidiser atomisation and consequently shorter vaporisation time.

Substantial research into the predication and characterisation of two phase flows, including experimentation, was carried out by Waxman (2014). This work was used by Invigorito et al. (2016) to validate a computational approach in determining the oxidiser mass flow rate through an injector of a two phase fluid. A similar method was used in the desinging of the PIB injector whereby the mass flow rate through a single orifice was found by completing a CFD analysis. The number of orifices required was then found by dividing the required mass flow rate by the simulaton result. A problem with this approach is that the upstream (and consequently downstream) pressures decay during operation due to the use of a blowdown system. Therefore a constant oxidiser mass flow rate cannot be achieved for the duration of the burn. However, simulations conducted for the lower pressure drops suggested that the flow still cavitates in the injector as shown in Figure 6.8. The use of the mass flow rate models yielded between 58 and 61 injector orifices with the CFD yielding 60 orifices at peak operating conditions. The procedure for setting up the two phase VOF transient cavitation model in STAR-CCM+™ was obtained from the User Guide (STAR-CCM+, 2015). Due to the two phase nature of nitrous oxide, the CFD results are considered more realistic than the analytical models (Invigorito, et al., 2016),

although the agreement obtained between the two approaches also provide some confidence in the CFD results.

Figures 6.9 and 6.10 show the final design of the injector plate having 60 axial one millimeter diameter orifices and a thickness of 10 mm (Figure 6.8). During the design process, the discharge coefficient (C_d) was assumed to have a value of 0.8 (Genevieve, 2013) (Waxman, et al., 2013) and so to ensure this, the inlet of each orifice was chamfered (Waxman, et al., 2013). To aid in oxidiser vaporisation, the injector plate was made of copper which has a higher thermal conductivity that can transfer heat from the combustion chamber into the incoming oxidiser. The injector plate is fastened to the injector bulkhead via six studs as shown in Figure 6.10.

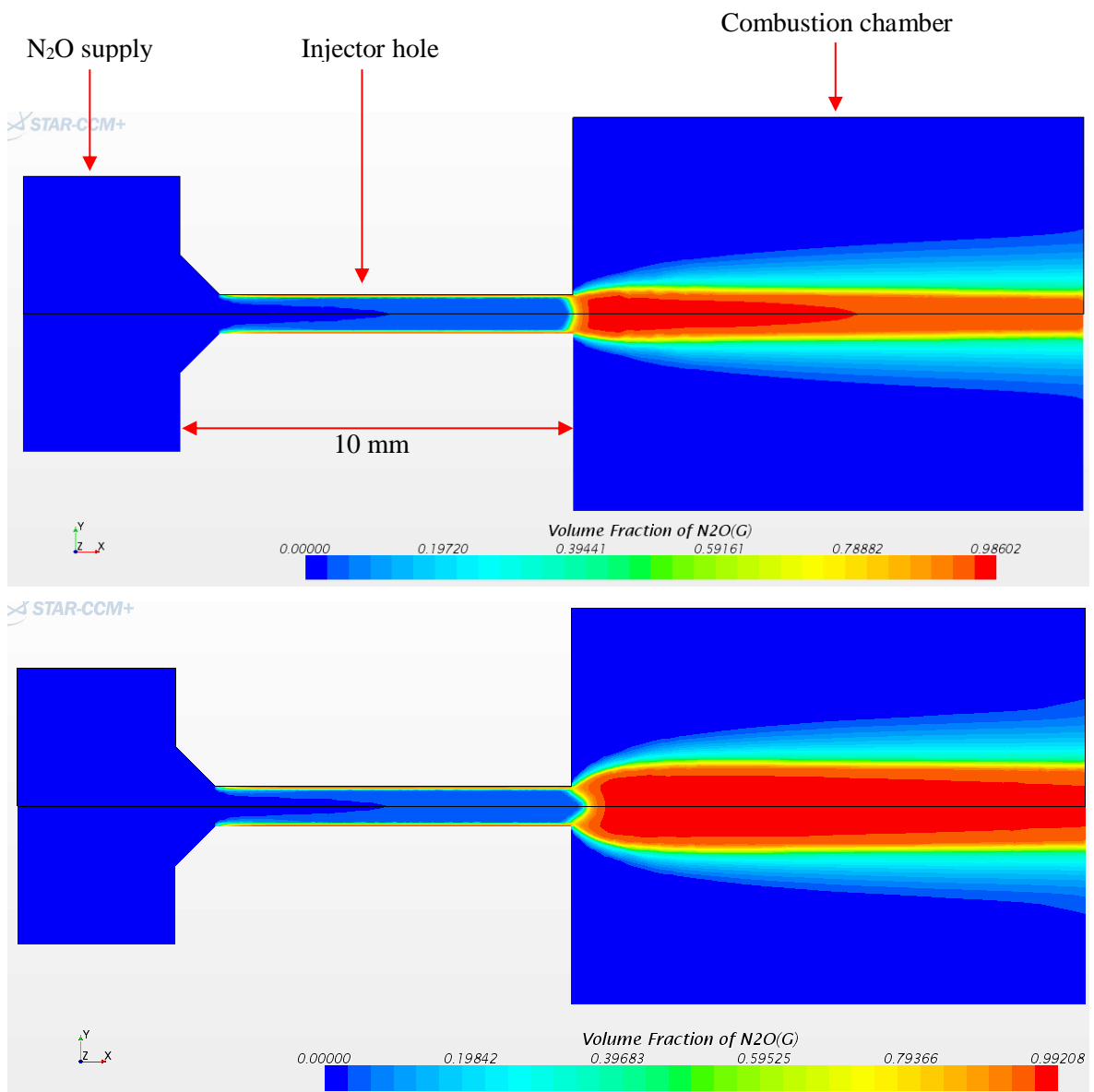


Figure 6.8: Nitrous oxide vapour volume fraction for (top) 65 bar upstream and 40 bar downstream pressure and (bottom) 57 bar upstream and 38 bar downstream pressure

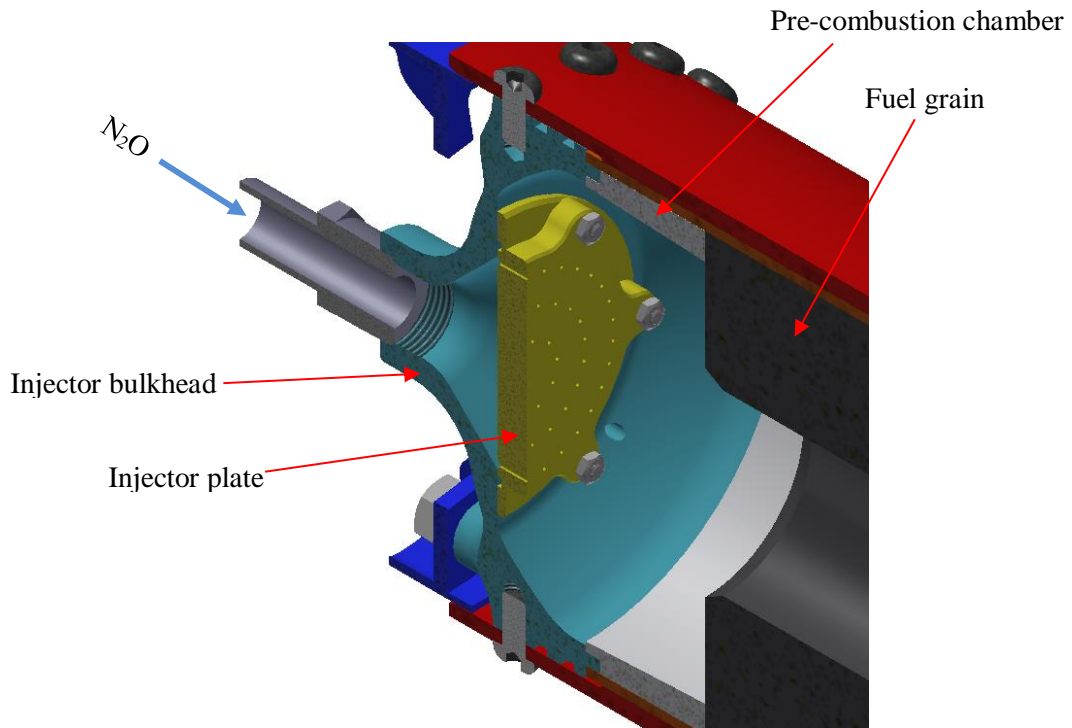


Figure 6.9: Cross-sectional rendition of the combustion chamber fore end

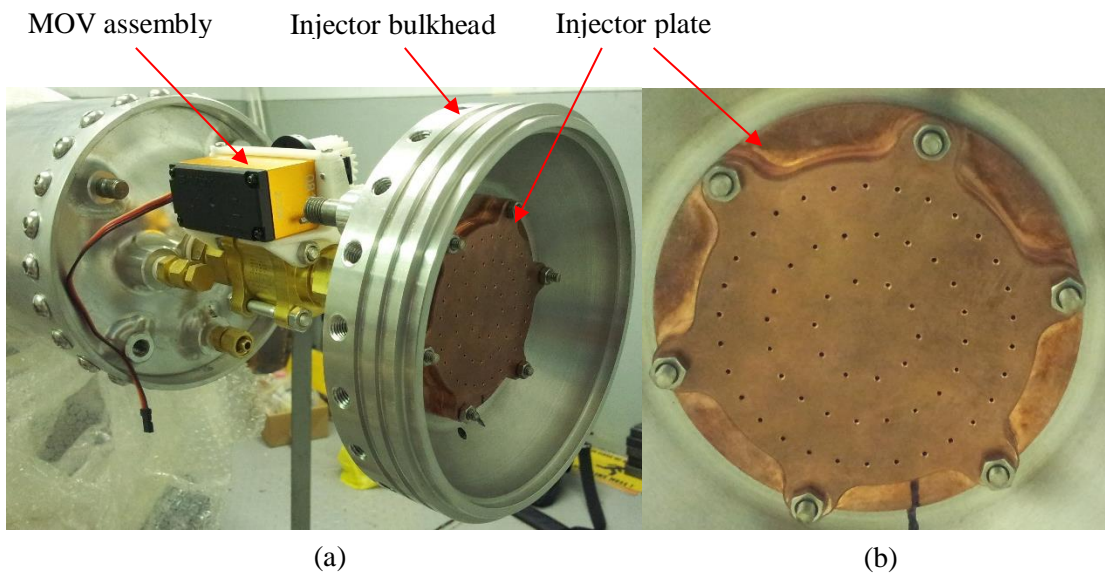


Figure 6.10: (a) Injector plate installed on the vehicle in readiness for cold flow testing, (b) view of the 60 one millimetre diameter orifices of the injector plate

6.6. Summary

A brief review of combustion instabilities was completed, focusing on feed system coupled instabilities which was used in the design of the P1B injector. Decreasing vaporisation time and avoiding compressibility effects in the feed system should reduce the instabilities and the use of an isolating element should also mitigate the hydrodynamic communication between the chamber and tank. An axial injector has been shown from literature to produce significantly lower instabilities than an impinging one. Three models namely, the incompressible, HEM and NHNE were used in an attempt to predict the mass flow rate of a two phase flow. Completion of a two phase volume of fluid CFD analysis resulted in the final injector plate design having 60, one millimetre diameter orifices to produce a mass flow of 1.9 kg/s.

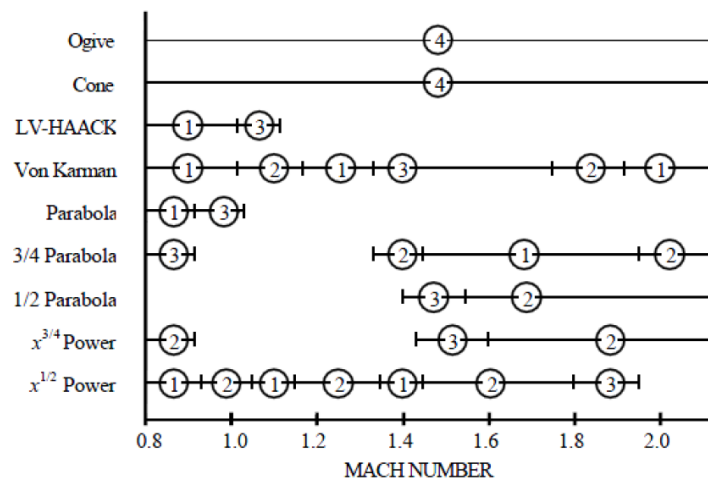
7. Phoenix-1B aerodynamics

7.1. Introduction

This chapter briefly describes the design of the nose cone and fin can for P1B. It should be noted that the aerostructural design of P1B was not the primary focus of this work and was therefore not optimised. Although in-depth analyses were not carried out, a conservative design approach was adopted to ensure aerodynamic stability of the vehicle and adequate structural performance of the rocket's nose and fins.

7.2. Nose cone design

Initial trajectory simulations of P1B carried out using the HYROPS software tool yielded a maximum Mach number of 1.92. The nose cone shape was selected using the selection chart shown in Figure 7.1, which indicates that the $\frac{3}{4}$ parabola and Von Karman profiles are superior at this speed. The P1A vehicle mass was slightly greater than that of the theoretical vehicle, on which the simulations were initially performed, due to non-ideal manufacturing. A conservative approach was thus taken for P1B and the $\frac{3}{4}$ parabola was selected.



Comparison of drag characteristics of various nose shapes in the transonic-to-low Mach regions. Rankings are: superior (1), good (2), fair (3), inferior (4).

Figure 7.1: Nose cone shape selection chart (Minnesota and Stroick, 2011)

The nose cone contour may be determined from Equation 7.1.

$$y = R \left(\frac{2 \left(\frac{x}{L} \right) - K \left(\frac{x}{L} \right)^2}{2 - K} \right) \quad 7.1$$

where K is 0.75 for a $\frac{3}{4}$ parabolic, R is the base radius and L is the length of the nose cone. Glass fibre reinforced plastic (GFRP) was selected as the fabrication material for the nose cone as it allows penetration of radio frequency signals related to the telemetry system (unlike carbon fibre) and is less expensive. In order to determine the required thickness of the composite nose cone, a CFD analysis was completed with the aim of characterising the external pressure loading on the nose. The results given in Figure 7.2 show that the peak drag is experienced when the vehicle is travelling through Mach 1. An axisymmetric analysis was then completed for a velocity of Mach 1.1 at zero degree angle of attack, the results of which can be seen in Figure 7.3. The external pressure distribution along the 1 m nose was then determined from the CFD results and is shown in Figure 7.4. The pressure peaks at 2.4 bar at the nose tip and then decreases rearwards, with a sudden pressure change visible due to the shock forming 80 cm from the tip. These results were provided to the nose cone manufacturer who determined that the minimum theoretical thickness was 2 mm. For the purposes of manufacturing and handling, this was increased to 3 mm. Although the vehicle is expected to reach a maximum velocity of Mach 1.92, the time spent at this speed is 0.15 s. Nevertheless, in order to avoid excessive heating of the composite, an aluminium tip was machined and bonded to the GFRP nose cone. A thermocouple can be inserted in the nose tip to measure the tip temperature during flight. The manufactured nose cone weighs 2 kg and is shown in Figure 7.5.

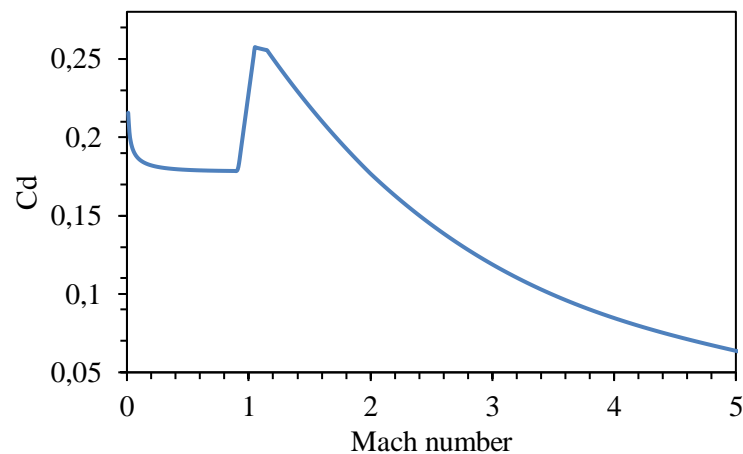


Figure 7.2: Coefficient of drag as a function of Mach number

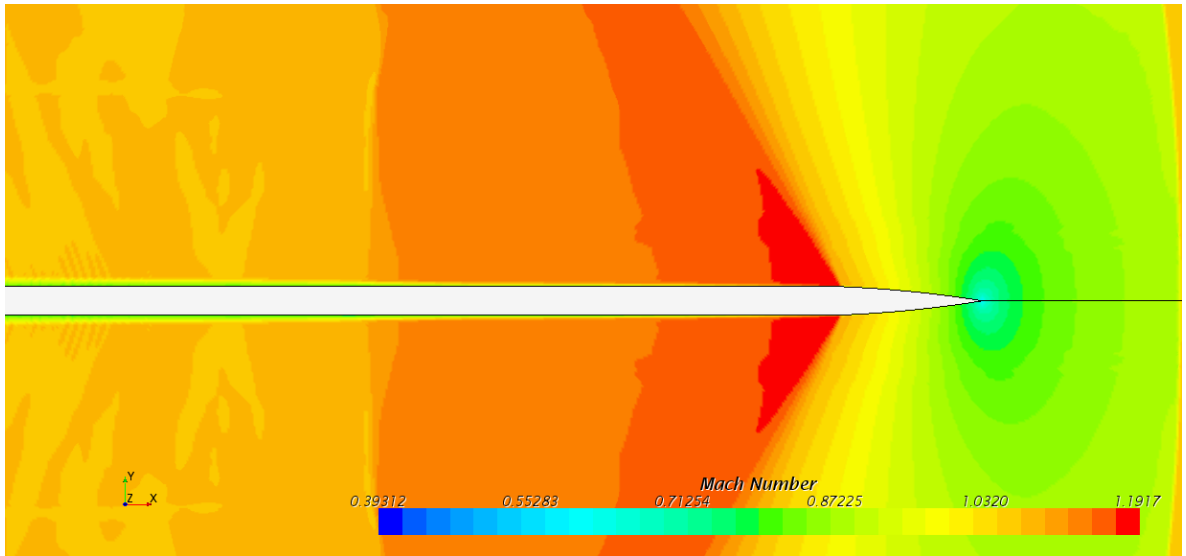


Figure 7.3: Mach distribution for P1B at Mach 1.1

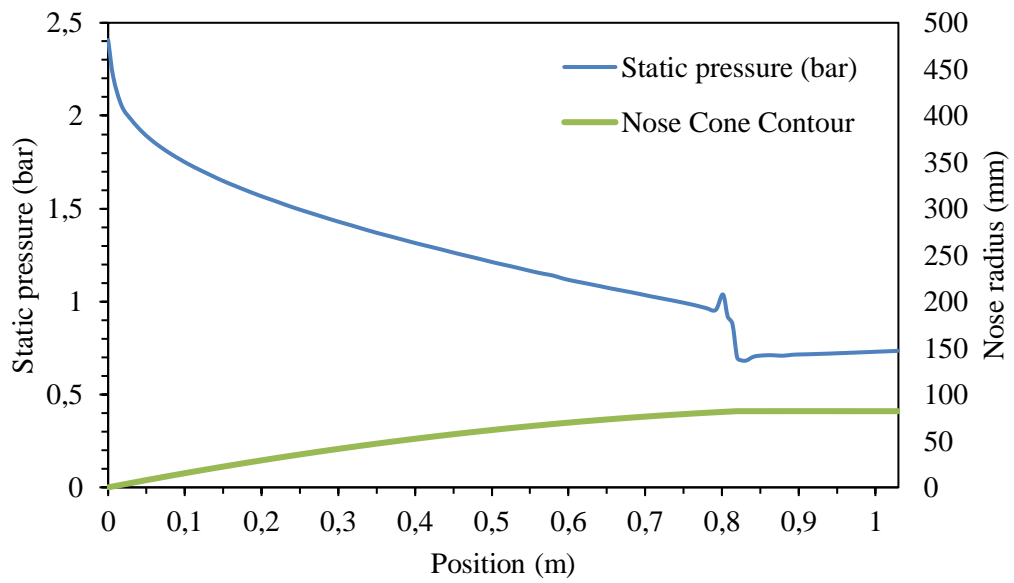


Figure 7.4: Pressure distribution on nose cone



Figure 7.5: Manufactured nose cone

7.3. Fin design

The P1B fin design and dimensions were based on those of P1A. The fin dimensions are given in Table 7.1 which can be read in conjunction with Figure 7.6. The method of attachment and fin material, were however changed. GFRP was chosen as it is lighter than aluminium and provides a superior attachment method. Unlike P1A, where individual fins were attached to the vehicle via a fin rail, P1B makes use of a fin can where the four aerofoils are bonded and blended onto a GFRP cylinder that slides over the combustion chamber as shown in Figure 7.7. A fillet radius of 35 mm was applied to the base of each fin to stiffen it and prevent bending and flutter. Unidirectional fibres were used from fin tip to fin tip to increase rigidity. A conservative approach was used as the design was not subjected to a comprehensive analysis. This resulted in a total fin can mass of 6 kg, which is 2 kg lighter than that of P1A.

By increasing the fin sweep length, the centre of pressure is pushed rearwards. This was done to ensure that the stability of the rocket was within one to two calibres, where the stability dimension is given by the distance between the vehicle's centre of pressure and centre of mass. Allowance was made for a slightly heavier rocket by designing the fins such the rocket has a stability margin of two calibres (that is, centre of pressure is located two times the rocket diameter behind the centre of mass). As in the case of P1A, the fins of P1B were canted by 0.5° to attain spin stabilisation.

Table 7.1: P1B fin dimensions

Parameter	Unit	Specification
Root chord	m	0.54
Tip chord	m	0.2
Wing span	m	0.15
Sweep	m	0.431
Thickness	m	0.009

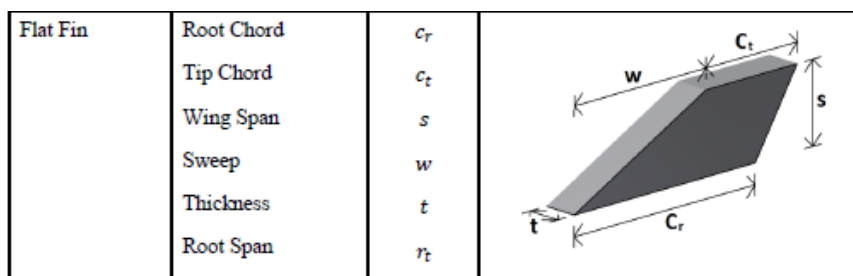


Figure 7.6: Fin design nomenclature (Chowdhury, 2012)

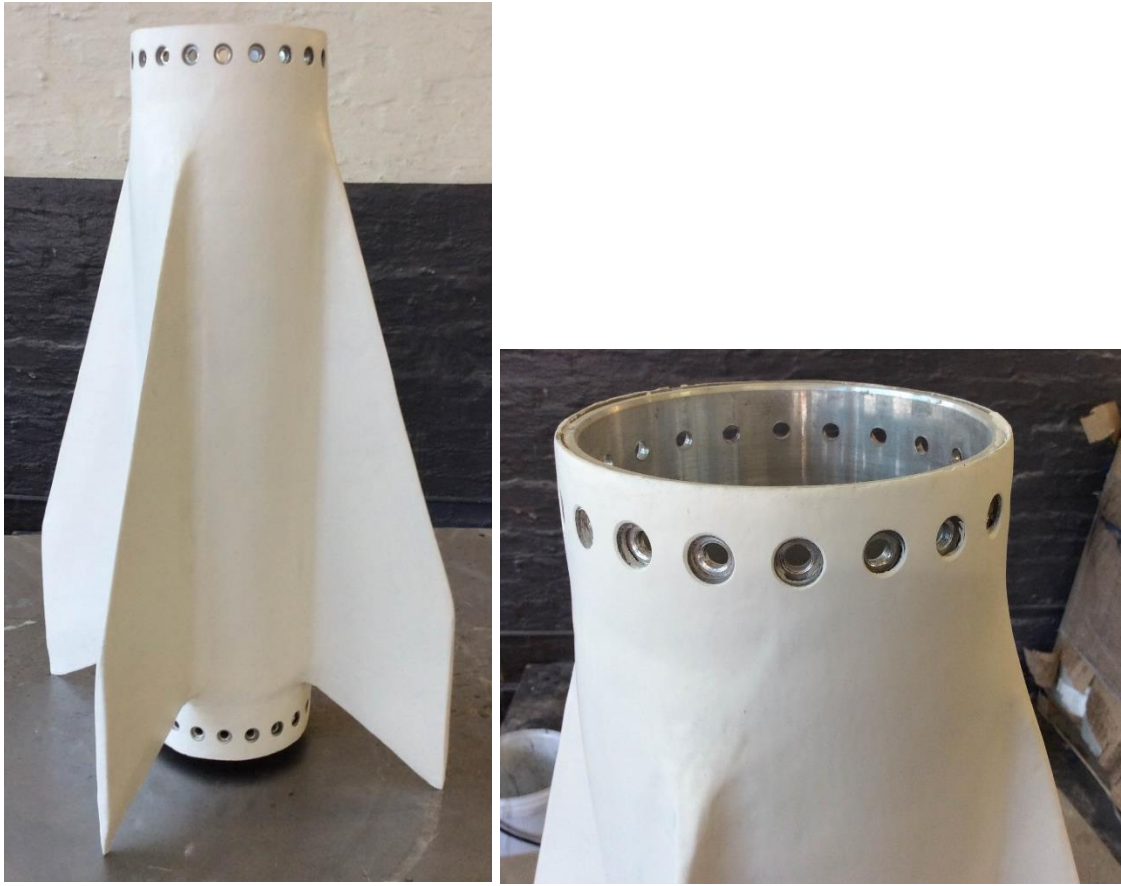


Figure 7.7: P1B fin can installed on the combustion chamber

7.5 Summary

A simplified but conservative design approach was adopted with respect to P1B airframe aerodynamics. A $\frac{3}{4}$ parabolic nose cone profile was selected for P1B based on the expected peak velocity of the vehicle. The thickness of the GFRP nose cone was derived from a CFD analysis which was conducted to determine the external pressure loading. For reasons of practicality this was increased slightly to 3 mm. A fin can design was adopted for P1B and provides a conservative stability factor of two calibres. To strengthen the fins, unidirectional fibres were laid from fin tip to adjacent fin tip. Both the nose cone and fin can were manufactured from GFRP to reduce costs and allow penetration of telemetry signals.

8. Final design and testing of Phoenix-1B

8.1. Introduction

This chapter serves to complete the design description of the P1B rocket and include a comprehensive comparison between P1A and P1B. The final theoretical performance parameters of the new vehicle are presented and a cold flow test of P1B described. Problematic areas such as the injector plate design and faulty vent quick-connect are highlighted and solutions are provided. At the time of writing, the vehicle had yet to be ground-tested or flown.

8.2. P1B vehicle design comparison

Tables 8.1 and 8.2 provide the design specifications and theoretical performance parameters of both P1A and P1B. Phoenix-1B is expected to reach an altitude of 17 km which is an increase of 2 km over the theoretical design and 14.5 km over the attained apogee of the P1A forerunner. This introduces added complexity with respect to launch site safety and necessitates the use of a flight termination system (FTS). A flight-qualified FTS is extremely costly for a developmental program such as the Phoenix HSRP, however, to ensure that the vehicle's energy footprint fits within the range's safety limits, the amount of nitrous oxide loaded into the vehicle will be limited. In doing so, the total impulse of the motor is reduced, shrinking the energy footprint.

Phoenix-1B is the first vehicle of the P1B series and the basis for future P1B variants to be compared to and improved upon. Similarly, P1B is compared to P1A with the new vehicle theoretically producing 1250 N more thrust than P1A and weighing 20 kg less with both vehicles utilising pure paraffin fuel. It is for this reason that some of the design specifications are similar in P1A and P1B, but the new composite nozzle represents a significant advancement over P1A. The combustion efficiency of P1B was assumed to be lower than that of P1A in this study mainly because of hot fire data from the P1A ground test. One significant difference between the two vehicles are the dimensions, with the P1B having a uniform diameter of 164 mm, whereas P1A had a tank diameter of 200 mm and tapering down to 180 mm. The smaller tank diameter of P1B meant that the oxidiser tank had to be longer than P1A (680 mm longer) to contain the same nitrous oxide load of 30 kg.

Table 8.1: Design specification comparison between P1A and P1B

			Specification	
	Parameter	Unit	P1A	P1B
Combustion chamber	Propellant		SASOL 0907 Paraffin wax	SASOL 0907 Paraffin wax
	Composition		97% wax, 3% charcoal	97% wax, 3% charcoal
	Port configuration		Single cylindrical	Single cylindrical
	Initial port diameter	m	0.05	0.06
	Grain diameter	m	0.156	0.148
	Grain length	m	0.4	0.404
	Combustion chamber length	m	0.66	0.67
	Combustion chamber diameter	m	0.18	0.164
Nozzle	Material		ATJ graphite	Silica phenolic, graphite, steel
	Type		Convergent-Divergent (CD)	Convergent-Divergent (CD)
	Contour shape		Bell-shaped	Bell-shaped
	Expansion ratio		5.99	6.38
	Throat diameter	m	0.0298	0.032
	Exit diameter	m	0.0731	0.083
	Nozzle length	m	0.134	0.156
Oxidiser tank	Oxidiser		Nitrous oxide	Nitrous oxide
	Supercharge gas		Helium	Helium
	Design oxidiser mass	kg	30	30
	Design supercharge gas mass	kg	0.006	0.005
	Tank volume	m ³	0.043	0.041
	Ullage	%	10	10
	Initial tank pressure	bar	65	65
	Tank length	m	1.6	2.28
	Tank diameter	m	0.2	0.164
Aerostructure	Nose cone shape		Ogive	3/4 parabola
	Forward airframe length	m	1.9	1
	Forward airframe diameter	m	0.2	0.164
	Recovery		Dual parachute	Nose recovery only

Table 8.1(cont.): Design specification comparison between P1A and P1B

Aerostructure	Material		Carbon fibre	Glass fibre
	Deployment system		Carbon dioxide (pyrotechnic)	Carbon dioxide (pyrotechnic)
	Fins		Four clipped-delta plan form trapezoidal, hexagonal cross-section	Four swept-delta plan form trapezoidal, hexagonal cross-section
General	Lift off mass (theoretical)	kg	90	70
	Vehicle length	m	4.55	4.224

The aluminium tubing will be used to construct both the oxidiser tank and the combustion chamber. The tube inner diameter of 153 mm limits the fuel grain diameter to 147 mm with a 3 mm thick phenolic/glass fibre/cotton thermal liner. Similarly to P1A, the pre- and post-combustion chambers of P1B were made from polyethylene. The use of lower-cost materials for airframe components such as glass fibre in place of carbon fibre and aluminium over stainless steel, has greatly reduced the overall cost of the P1B vehicle. Figure 8.1 provides the simulated ballistic (no parachute deployment) trajectory data for the new vehicle, assuming a gantry launch angle of 80° and zero wind. A cross-section rendition of the final P1B vehicle can be seen in Figure 8.2, showing major sub-assemblies and components. A rendition of the entire vehicle can be seen in Figure 1.4.

Table 8.2: Theoretical performance comparison between P1A and P1B

Parameter	Unit	Specification	
		P1A	P1B
Design peak thrust	N	4250	5000
Design O/F		6.8	6.8
Design combustion efficiency	%	95	90
Combustion chamber pressure	bar	40	40
Oxidiser mass flow rate	kg/s	1.34	1.9
Vacuum specific impulse	s	243	252
Total impulse	Ns	75 000	69000
Design apogee altitude	km	15.0	17.2
Maximum speed	m/s	571	661
Maximum acceleration	m/s ²	32.8	58.6
Ballistic flight time	s	126	132

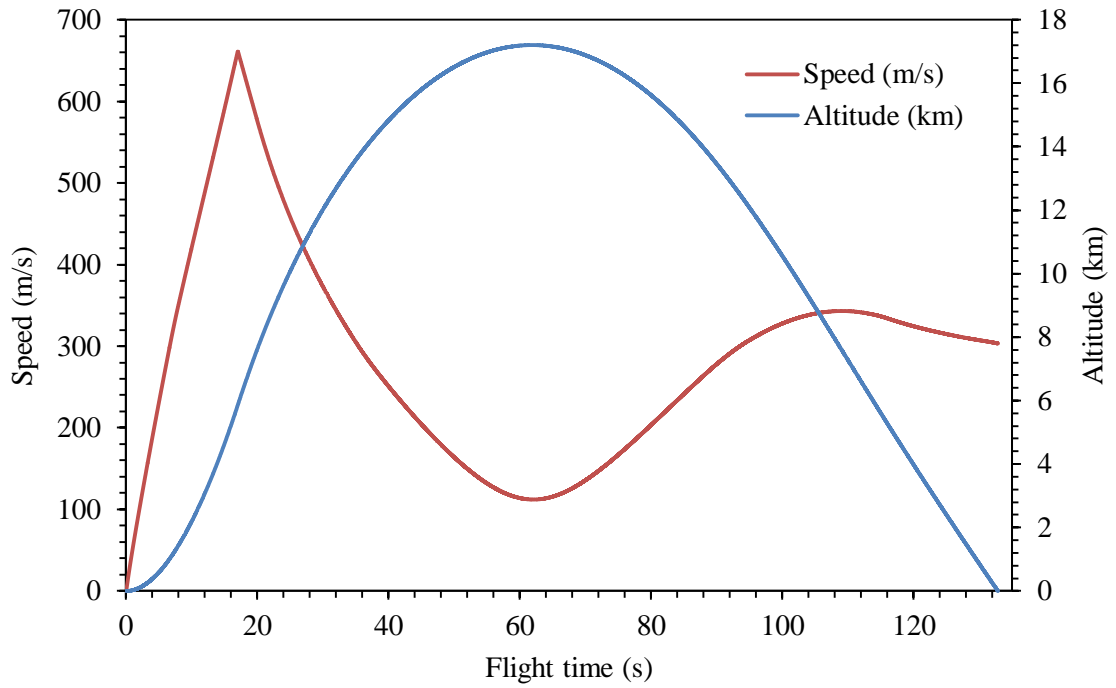


Figure 8.1: Simulated ballistic trajectory and speed of P1B for a launch angle of 80° with no wind at Overberg Test Range.

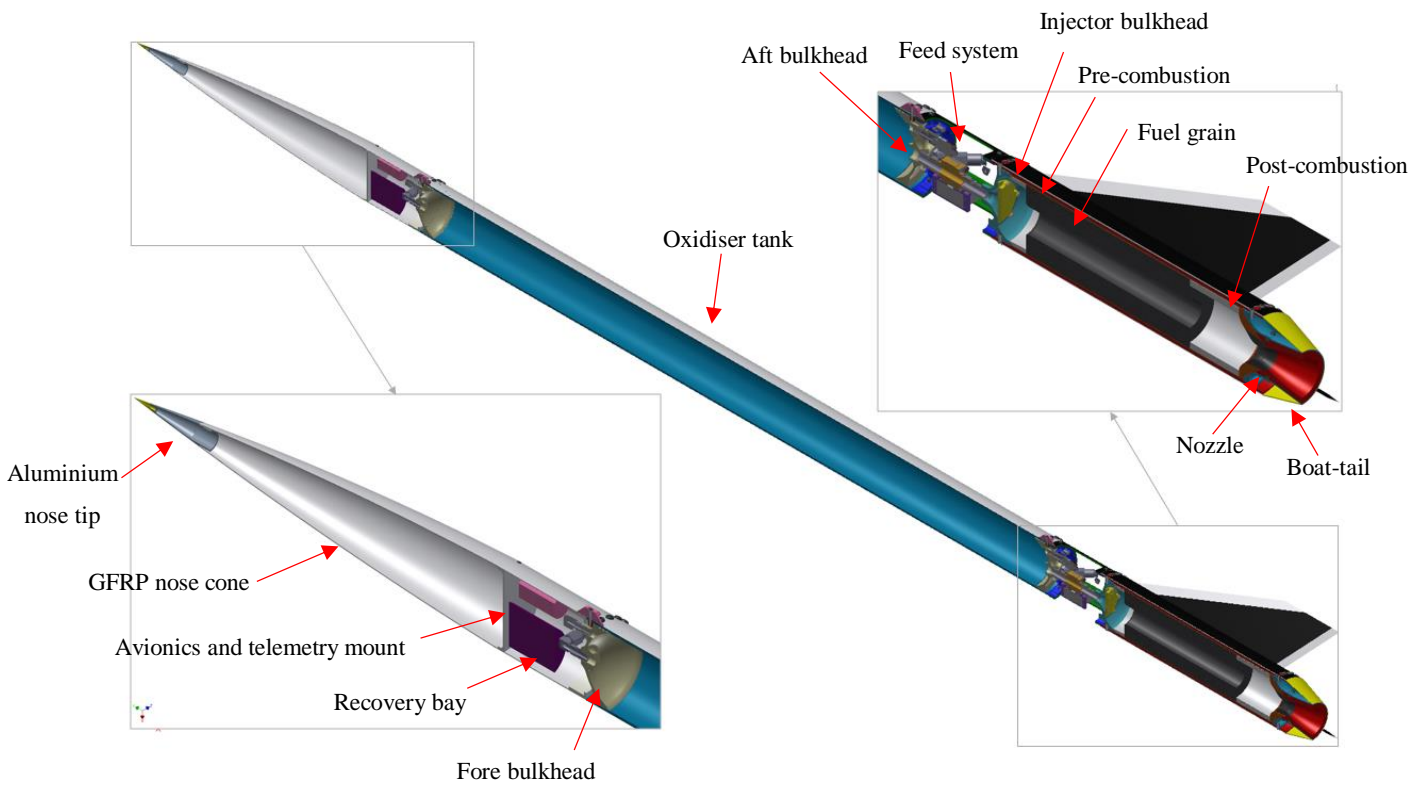


Figure 8.2: Cross-section rendition of the final design of P1B

8.3. Cold flow test

A cold flow test of the P1B hybrid rocket was conducted in September 2016. This was the first time nitrous oxide was loaded into the oxidiser tank which successfully contained the high pressure liquid with no leaks, even after pressurising to 65 bars. Figure 8.3 shows the vehicle in test configuration with no combustion chamber. This was done so as to enable the observation of the flow out of the injector.

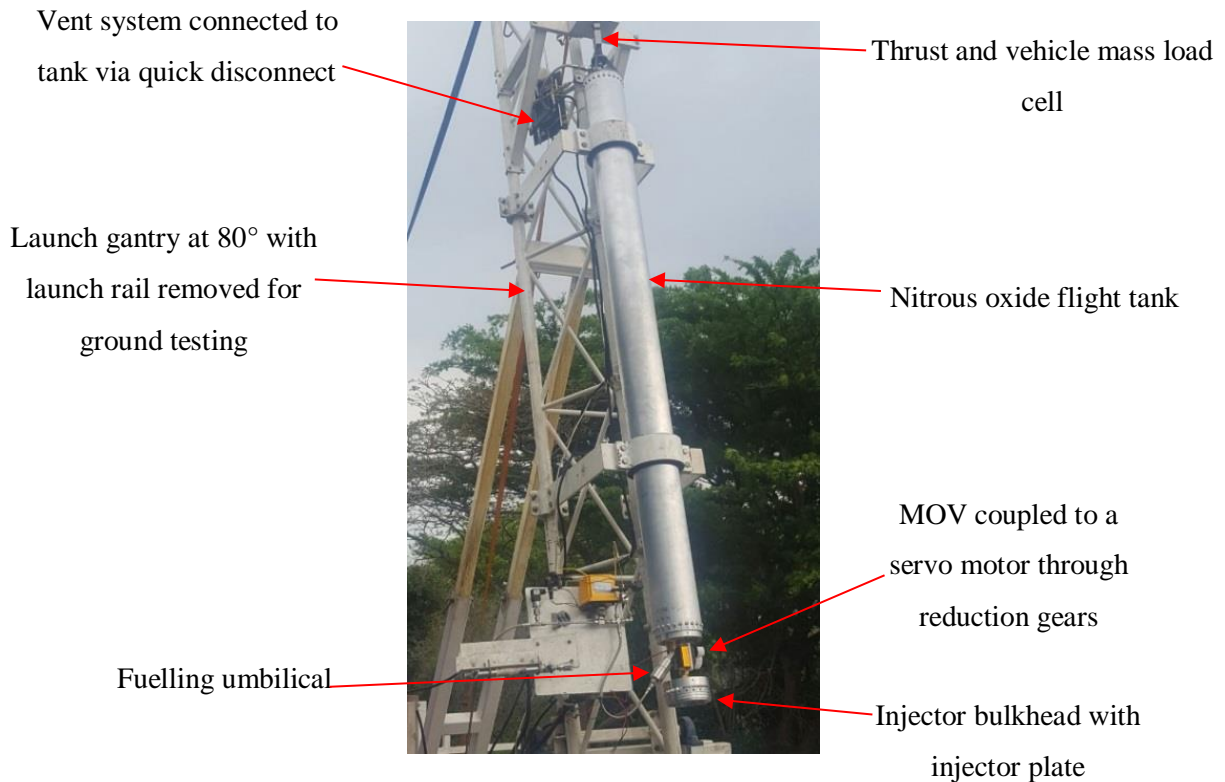


Figure 8.3: P1B Cold flow test

Post test data analysis (Figure 8.4) showed a difference in liquid and vapour pressure as well as the effect of venting. Once the vent valve opens, the pressure in the tank drops, creating a larger pressure differential between the pneumatic pump and flight tank, thereby driving nitrous oxide liquid flow. This is shown with the sudden drop in pressure in Figure 8.5. The difference in pressures is a positive indication that the hydrostatic pressure measurement method can be effective. However, during the test, a fault occurred with the vent system, specifically the quick disconnect, which resulted in the loss of venting control.

Another positive outcome of the test was the validation of the injector design. Figure 8.6 depicts snapshots of the video footage (Appendix D.5 and D.6). The fine atomisation of the incoming liquid nitrous can be seen in Figures 8.6 and 8.7 which corresponds to expectations. The improved

data acquisition can be seen in Figure 8.5, which stands in contrast to Figure 2.4. One improvement that could be made to actualise the hydrostatic flow measurement system is to incorporate a higher resolution data acquisition system. Due to the high vapour pressure of nitrous oxide and relatively low fluid density at room temperatures, the actual hydrostatic force may be miniscule which the current NI 12-bit ADC's cannot detect. Successful completion of a cold flow test will provide more data on this measurement system.

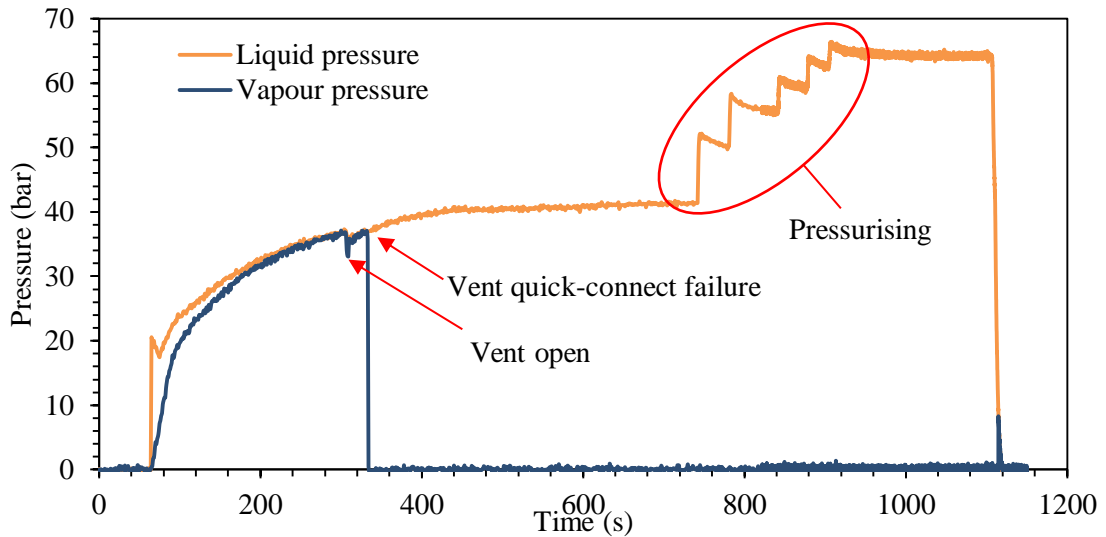


Figure 8.4: Pressure VS time traces of the liquid and vapour pressure in the flight tank for test duration

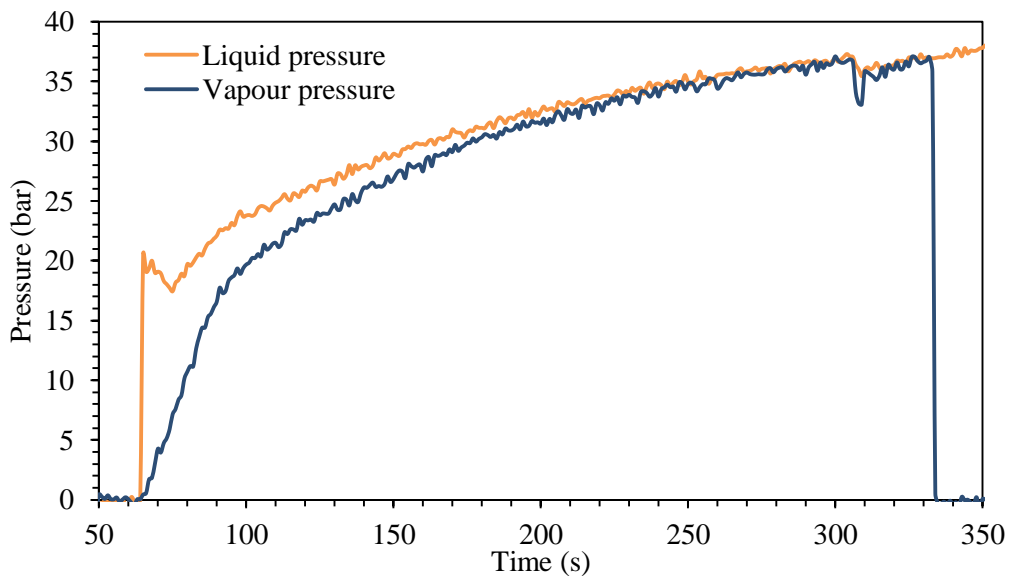


Figure 8.5: Pressure VS time traces of the liquid and vapour pressure in the flight tank until quick-connect failure



Figure 8.6: Injector plume development

During testing, however, a design flaw in the injector plate attachment was noted whereby the injector plate was ejected from the injector bulkhead as the MOV was fully opened, which can be seen in Figures 8.7 and 8.8. The injector plate was fastened to the injector bulkhead via M4 sized stainless steel studs which were screwed into six tapped threaded holes in the aluminium bulkhead (Figure 8.8(b)). Inspection of the bulkhead showed that the aluminium threads were stripped and were not tapped to the required depth. From the video footage (Appendix D.5 and D.6), ice build-up can be seen on the injector bulkhead which was due to the nitrous oxide expanding through the injector plate. It was proposed that the failure was due to the rapid cooling, which caused the aluminium to become brittle, and the reduced thread engagement length, which was attributed to a manufacturing flaw. A possible revised injector bulkhead design was developed which utilised a through hole design over the stud design and can be seen in Figure 8.9. This design relies on the strength of the stronger steel threads of the bolts whereas the original design depended on weaker aluminium threads. A higher torque setting on the bolts that fasten the injector plate to the bulkhead can be utilised in the improved design which strengthens the joint.



Figure 8.7: Injector plate being ejected from the injector bulkhead during cold flow test



Figure 8.7 (cont.): Injector plate being ejected from the injector bulkhead during cold flow test



(a)

(b)

Figure 8.8: (a) Injector plate damage after impact, (b) injector bulkhead

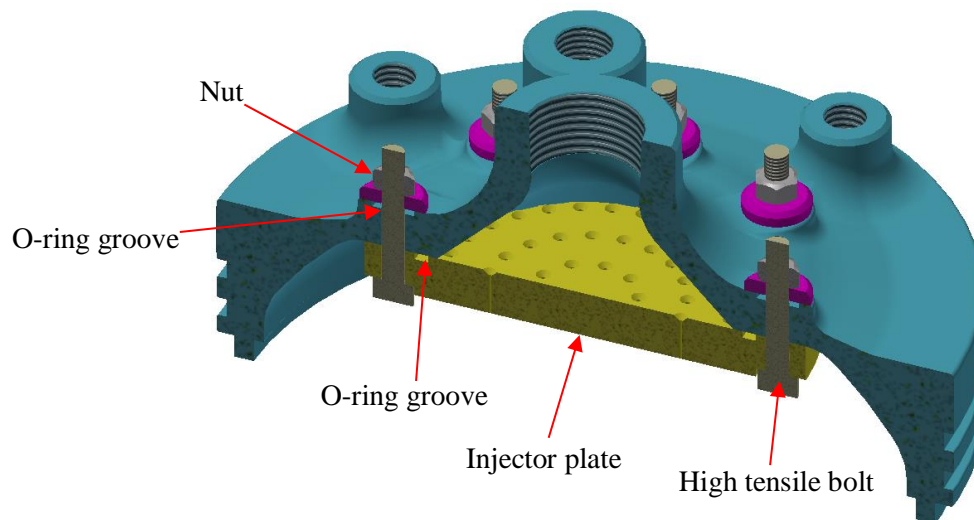


Figure 8.9: Cross-section rendition of the improved injector bulkhead design

8.4. Summary

A comprehensive comparison between the final P1B hybrid rocket and its predecessor, P1A was given. The P1B propulsion system significantly improves vehicle performance to provide a design apogee of 17 km. After successfully pressurising the oxidiser tank to 65 bars during a cold flow test conducted on the P1B vehicle, the oxidiser plume from the injector was observed and led to an improved injector attachment method to the injector bulkhead.

9. Conclusion and recommendations

9.1. Overview

The Phoenix Hybrid Sounding Rocket Programme aims to provide a launch capability to the local scientific community by developing a sounding rocket to carry experimental payloads into the upper atmosphere. This requires the development of a low-cost and reliable launch system. Due to their safety and cost-effectiveness, hybrid rocket propulsion systems are an attractive option for such applications.

The first vehicle that was developed in the Phoenix Programme was Phoenix-1A which was launched in August 2014 from the Overberg Test Range in the Western Cape, and is the first hybrid sounding rocket to be developed by students in South Africa. The next step in the programme has been the development of a low-cost hybrid rocket, designated Phoenix-1B, which has the capability to be launched on an ongoing basis. In order to establish the constraints and requirements of P1B, the developmental and testing processes of Phoenix-1A were analysed. This highlighted several design elements requiring revision, including the oxidiser tank, airframe, recovery system and nozzle.

9.2. Conclusions

The conclusions that are presented here are in reference to the objectives of this study that are given in Chapter 1:

Objective 1: Provide a modular propulsion system design to aid in the progression of the Phoenix HSRP.

Throughout the design of the P1B hybrid rocket, attention was paid to design modularity so as to provide a cost-effective and easily-reconfigurable propulsion system that can support future developments in the programme. In Chapter 3, the effect of the addition of aluminium loading to paraffin wax fuel was investigated and was found to increase the density specific impulse and improve the vehicle propellant mass ratio, at least on a theoretical basis. However, aluminium addition can also result in a substantial increase in combustion temperature. The manufactured nozzle was designed to operate according to the worst thermal loading case, where the fuel grain comprises of 40% aluminium. This would allow for the steel nozzle structure designed here to be used for any aluminium fuel loading up to 40% by mass. Lower aluminium fuel loadings require lower expansion ratios and therefore the flow contour of the nozzle would still need to be changed.

Such a change would be straightforward to make, however, considering that a pure paraffin wax fuel grain has been selected for the first version of P1B, the as-designed flow contour is non-optimal in this instance. However, this compromise was deemed to be acceptable at the current stage.

Additionally, in Chapter 4, modularity was achieved in the design of the oxidiser tank and combustion chamber. By avoiding welding and the negative consequences associated with heat affected zones, two bulkhead retention methods were investigated. These comprised the use of a spiral retaining ring and the more common radially bolted joint design. Both methods were analysed through FEA and were pressure tested. The spiral retaining ring was shown to be advantageous in terms of bulkhead installation, however, the bolted design was selected to avoid undue stresses imparted on the feed system. The final design incorporated 24 bolts for each of the oxidiser tank bulkheads and 20 bolts for the combustion chamber injector bulkhead and nozzle. O-rings were used around the bulkheads and nozzle to ensure adequate sealing. This design allows easy assembly and disassembly of the bulkheads and nozzle, as well as interchangeability for future designs.

Objective 2: Improve on the design, apogee and motor performance of P1A.

In chapter 2, the design and shortcomings of P1A were analysed so as to provide the necessary requirements and design criteria for an improved and more reliable P1B design. The aluminised grain investigation showed that there is small increase in characteristic velocity from 1457 m/s for pure paraffin wax to 1479 m/s for 40% aluminised wax. As the specific impulse is the product of the characteristic velocity and force coefficient (C_f), an increased C^* value will result in a higher specific impulse for the same force coefficient and consequently a higher density specific impulse with increasing aluminium loading.

The vehicle described in this study is the first of the P1B series of experimental rockets to investigate the flight performance gains of aluminium loading in the paraffin fuel and validate the results presented in this study. Given this, the current vehicle makes use of a pure paraffin and nitrous oxide propellant combination similar to P1A, however, P1B produces 1250 N more thrust which propels the vehicle to an apogee of 17 km, which is 2 km higher than the theoretical P1A apogee and 14.5 km higher than the P1A flight test apogee. With the higher design mass flow rate of P1B, the maximum simulated speed of P1B is 661 m/s as compared to 571 m/s simulated for P1A.

An intensive nozzle design and iterative thermo-structural analysis was conducted to develop a nozzle with greater structural robustness than that used in P1A. Simulation results were found to indicate critical design safety factors in excess of the minimum value of 1.5 on yield strength, with the exception of the nozzle structure which was designed according to the ultimate tensile strength to minimise mass. The nozzle was not designed to be re-used due to the ablation of the silica phenolic insulation.

Objective 3: The new vehicle must be cost effective and have a reduced mass.

In analysing the design and construction of P1A, it was found that the vehicle mass and cost were strongly sensitive to the airframe, oxidiser tank and combustion chamber designs. The P1A nose cone was made of pre-impregnated carbon fibre composite which required a costly manufacturing process to attain the specified tolerances, whereas the P1B's nose cone was made of lower-cost glass fibre composite. The fins of P1A were made of aluminium with stainless steel fin rails which resulted in an assembly mass of 8 kg. For P1B, a fin can design which slides over the combustion chamber was chosen and manufactured from glass fibre composite, resulting in a reduced mass of 6 kg.

The combustion chamber and oxidiser tanks of P1A were machined from solid billets of aluminium and welded together. This expensive process was avoided for P1B which utilised commercially-available 6061-T6 aluminium tubing for the oxidiser tank shell and combustion chamber casing. This tubing, however, had a reduced diameter of 164 mm compared to the P1A diameter of 200 mm, which resulted in a longer P1B booster section. These improvements resulted in the P1B vehicle weighing 70 kg at lift off, which is a 20 kg improvement over P1A.

Objective 4: Improve the ground support system to ensure a specified mass of oxidiser is loaded into the flight tank as well as develop an oxidiser flow rate measurement capability.

The data sampling rate of the ground support equipment was increased to better-acquire crucial data during vehicle testing. A method of measuring oxidiser mass in the flight tank was proposed, which makes use of tank hydrostatic pressure measurement. Pressure and temperature sensors located on the fore and aft ends of the oxidiser tank as well as a pressure sensor on the injector bulkhead, enable motor performance to be measured during ground testing and during flight. Flight performance data of hybrid rockets is scarce and the acquisition of such data is therefore one of the aims of the P1B flight test. The hydrostatic pressure measurement system has the

theoretical capability to measure the oxidiser mass flow rate by monitoring the changing hydrostatic pressure.

One of the main contributing factors to P1A not reaching its intended apogee was the fact that it could not be filled with its design-point nitrous oxide load. To overcome this, a vent system was incorporated on the GSE to enable the full 30 kg of nitrous oxide to be loaded into the P1B flight vehicle.

9.3. Recommendations and future work

At the time of writing, the Phoenix-1B vehicle is structurally complete and awaiting a final cold-flow test to validate the hydrostatic mass measurement system. Following this, a hot-fire test will be conducted before proceeding to launch. To acquire key motor performance and vehicle flight data, an onboard data acquisition and telemetry system is being developed which will transmit real-time data to a ground station during flight.

At the current stage, the following recommendations can be made to aid in the improvement of the initial P1B variant. The thermo-structural analysis of the nozzle assumed isotropic material properties. To further increase the accuracy of the analysis, orthotropic properties should be included. Ideally an aero-thermal-structural analysis should be completed on the nozzle which requires propellant dependent flow properties.

Further attention should be given to characterising and reducing combustion instabilities. It has been acknowledged that flow recirculation in the pre-combustion chamber heats the incoming oxidiser and aids in its vaporisation. An enhanced analysis of this phenomenon can be undertaken by extending the two phase model described in this dissertation to include the entire pre-combustion chamber cavity. While only low frequency combustion instabilities were considered in this study, high frequency instabilities should also be addressed to ensure the absence of destructive pressure oscillations. Future work may also consider the effect of instabilities on combustion efficiency in hybrid rocket motors.

Finally, as the design of the P1B aerostructure was not of primary concern in this work, it is suggested that in-depth structural analysis be undertaken in order to minimise the mass of the aerostructure and improve its aerodynamic efficiency.

References

- Babula, M., 2016. *Nuclear Thermal Rocket Propulsion*. [Online] Available at: <http://trajectory.grc.nasa.gov/projects/ntp/> [Accessed 20 October 2016]
- Balmogim, U., Brooks, M. J., Pitot de la Beaujardiere, J. F., Veale, K., Genevieve, B. and Roberts, L. W., 2015. *Preliminary Design of the Phoenix-1B Hybrid Rocket*. Orlando, 51st AIAA/SAE/ASEE Joint Propulsion Conference.
- Bartz, D. R., 1957. A Simple Equation for Rapid Estimation of Rocket Nozzle Convective Heat Transfer Coefficients. *Journal of Jet Propulsion*, 27(1), pp. 49-53.
- Bartz, D. R., 1965. Turbulent Boundary-Layer Heat Transfer from Rapidly Accelerating Flow of Rocket Combustion Gases and of Heated Air. *Advances in Heat Transfer*, Volume 2, pp. 1-108.
- Brooks, M. J., Pitot de la Beaujardiere, J. F., Chowdhury, S. M., Genevieve, B. and Roberts, L. W., 2010. *Introduction to the University of KwaZulu-Natal Hybrid Sounding Rocket Program*. Nashville, American Institute of Aeronautics and Astronautics.
- Chowdhury, S. M., 2012. *Design and Performance Simulation of a Hybrid Sounding Rocket*, MScEng Thesis, Durban: University of KwaZulu-Natal.
- Dyer, J., Doran, E., Dunn, Z., Lohner, K., Bayart, C., Sadhwani, A., Zilliac, G., Cantwel, B. and Karabeyoglu, A., 2007. *Design and Development of a 100km Nitrous Oxide/Paraffin Hybrid Rocket Vehicle*. Cincinnati, 43rd AIAA/ASME/SAE/ASEE Joint Propulsion Conference and Exhibit.
- Genevieve, B., 2013. *Development of a Hybrid Sounding Rocket Motor*, MScEng Thesis, Durban: University of KwaZulu-Natal.
- Genevieve, B., Pitot, J., Brooks, M., Chowdhury, S., Veale, K., Leverone, F., Balmogim, U. and Mawbey, R., 2015. *Flight Test of the Phoenix-1A Hybrid Rocket*. Orlando, 51st AIAA/SAE/ASEE Joint Propulsion Conference, AIAA Propulsion and Energy Forum.

Gordon, W. E., 1962. *The Relative Importance of Density, Specific Impulse and other Solid Propellant Properties in the Frame of Long-Term Research Goals*, Virginia: Institute for Defense Analyses.

Heston, T., 2009. *How to relieve stress in welding*. [Online] Available at: <http://www.thefabricator.com/article/testingmeasuring/how-to-relieve-stress-in-welding> [Accessed 20 October 2016].

Humble, R. and Altman, D., 1995. *Space Propulsion Analysis and Design*. United States of America: McGraw-Hill.

Indian Space Research Organisation, 2016. *Sounding Rockets*. [Online] Available at: <http://www.isro.gov.in/launchers/sounding-rockets> [Accessed 20 October 2016].

Invigorito, M., Elia, G. and Panelli, M., 2016. An Improved Approach for Hybrid Rocket Injection System Design. *International Journal of Mechanical, Aerospace, Industrial, Mechatronic and Manufacturing Engineering*, 10(4), pp. 640-650.

Karabeyoglu, A., 2012. *Lecture 10: Hybrid Rocket Propulsion Design Issues*, Stanford: Stanford University.

Karabeyoglu, A., 2012. *Lecture 8, Hybrid Rocket Propulsion Fundamentals*, Stanford: Stanford University.

Karabeyoglu, M. A., Altman, D. and Cantwell, B. J., 2002. Combustion of Liquefying Hybrid Propellants: Part 1, General Theory. *Journal of Propulsion and Power*, 18(3), pp. 610-620.

Karp, A. C., 2012. *An investigation of liquefying hybrid rocket fuels with applications to solar system exploration*, Stanford: Stanford University.

Leverone, F. K., 2013. *Performance Modelling and Simulation of a 100 km Hybrid Sounding Rocket*, MScEng Thesis, Durban: University of KwaZulu-Natal.

Lohner, K., Dyer, J., Doran, E., Dunn, Z. and Zilliac, G., 2006. *Fuel Regression Rate Characterization Using a Laboratory Scale Nitrous Oxide hybrid Propulsion System*. Sacramento, 42nd AIAA/ASME/SAE/ASEE Joint Propulsion Conference and Exhibit.

- Martin, S. and Pfaff Jr., R. F., 2016. *NASA Sounding Rocket Program Overview*. [Online] Available at: <http://rscience.gsfc.nasa.gov/srrov.html> [Accessed 30 October 2016].
- Marxman, G. A., Wooldridge, C. E. and Muzzy, R. J., 1963. *Fundamentals of Hybrid Boundary Layer Combustion*. Palm Beach, AIAA Heterogeneous Combustion Conference.
- MatWeb, 2016. *Aluminium 6061-T6*. [Online] Available at: http://www.matweb.com/search/datasheet_print.aspx?matguid=1b8c06d0ca7c456694c7777d9e10be5b [Accessed 15 November 2016].
- McCormick, A., Hultgren, E., Lichtman, M., Smith, J., Sneed, R. and Azimi, S., 2005. *Design, Optimization, and Launch of a 3" Diameter N₂O/Aluminized Paraffin Rocket*. Tucson, 41st AIAA/ASME/SAE/ASEE Joint Propulsion Conference & Exhibit.
- NASA, 1975. *Solid Rocket Motor Nozzles Monograph*, Cleveland: National Aeronautics and Space Administration.
- Rao, G. V., 1958. *Exhaust Nozzle Contour for Optimum Thrust*. *Jet Propulsion Journal*, Volume 28, pp. 377-382.
- Rao, G. V. R., 1961. *Recent Developments in Rocket Nozzle Configurations*. *American Rocket Society Journal*, pp. 1488-1494
- Seitzman, J. M., 2012. *Bell/Contoured Nozzle, AE6450 Rocket Propulsion Lecture*, Georgia: Georgia Tech.
- Smalley, , 2015. *Ring Design handbook*, United States of America: Smalley.
- Smith, D. M., 1970. *A Comparison of Experimental Heat-Transfer Coefficients in a Nozzle with Analytical Predictions from Bartz's Methods for Various Combustion Chamber Pressures in a Solid Rocket Motor*, Springfield: North Carolina State University.
- Soloman, B. J., 2011. *Engineernig Model to Calculate Mass Flow Rate of a Two-Phase Saturate Fluid Through and Injector Orifice*, MSc Thesis, Utah: Utah State University.

STAR-CCM+, 2015. *STAR-CCM+ User Guide Version 9.06*, United States of America: CD-adapco.

Sutton, G. P. and Biblarz, O., 2001. *Rocket Propulsion Elements, Seventh Edition*. Canada: John Wiley and Sons.

Thakre, P., 2008. *Chemical Erosion of Graphite and Refractory Metal Nozzles and its Mitigation in Solid-Propellant Rocket Motors*, Pennsylvania: Pennsylvania State University.

Thakre, P., Rawat, R., Clayton, R. and Yang, V., 2013. Mechanical Erosion of Graphite Nozzle in Solid-Propellant Rocket Motor. *Journal of Propulsion and Power*, 29(3), pp. 593-601.

United States Military, 1998. *MIL-DTL-27426C, Rings, Retaining, Spiral (Uniform Cross Section)*, United States of America: Department of Defense.

Waxman, B. S., 2014. *An Investigation for use with high vapor pressure propellants with applications to hybrid rockets, PhD thesis*, Stanford: Stanford University.

Waxman, B. S., Beckwith, R., Tybor, F., Zimmerman, J. and Stoll, A., 2010. *Paraffin and Nitrous Oxide Hybrid Rocket as a Mars Ascent Vehicle Demonstrator*. Anaheim, AIAA Space 2010 Conference and Exposition.

Waxman, B. S., Zimmerman, J. E., Cantwell, B. J. and Zilliac, G. G., 2013. *Mass Flow Rate Characterization of Injectors for use with Self-Pressurizing Oxidizers in Hybrid Rockets*, Stanford: Stanford University.

Waxman, B. S., Zimmerman, J. E., Cantwell, B. J. and Zilliac, G. G., 2013. *Mass Flow Rate Characterization of Injectors for use with Self-Pressurizing oxidisers in Hybrid Rockets*, Stanford: Stanford University.

Waxman, B. S., Zimmerman, J. E., Cantwell, B. J. and Zilliac, G. G., 2014. *Effects of Injector Design on Combustion Stability in Hybrid Rockets Using Self-Pressurizing Oxidisers*. Cleveland, 50th AIAA/ASME/SAE/ASEE Joint Propulsion Conference.

Wirsig, G., 1996. *Space Propulsion Analysis and Design*. United States of America: McGraw-Hill.

Zilliac, G. and Karageyoglu, A. M., 2006. *Hybrid Rocket Fuel Regression Rate Data and Modeling*. Sacramento, 42nd AIAA/ASME/SAE/ASEE Joint Propulsion Conference and Exhibit.

Appendix A: Nozzle design flow chart

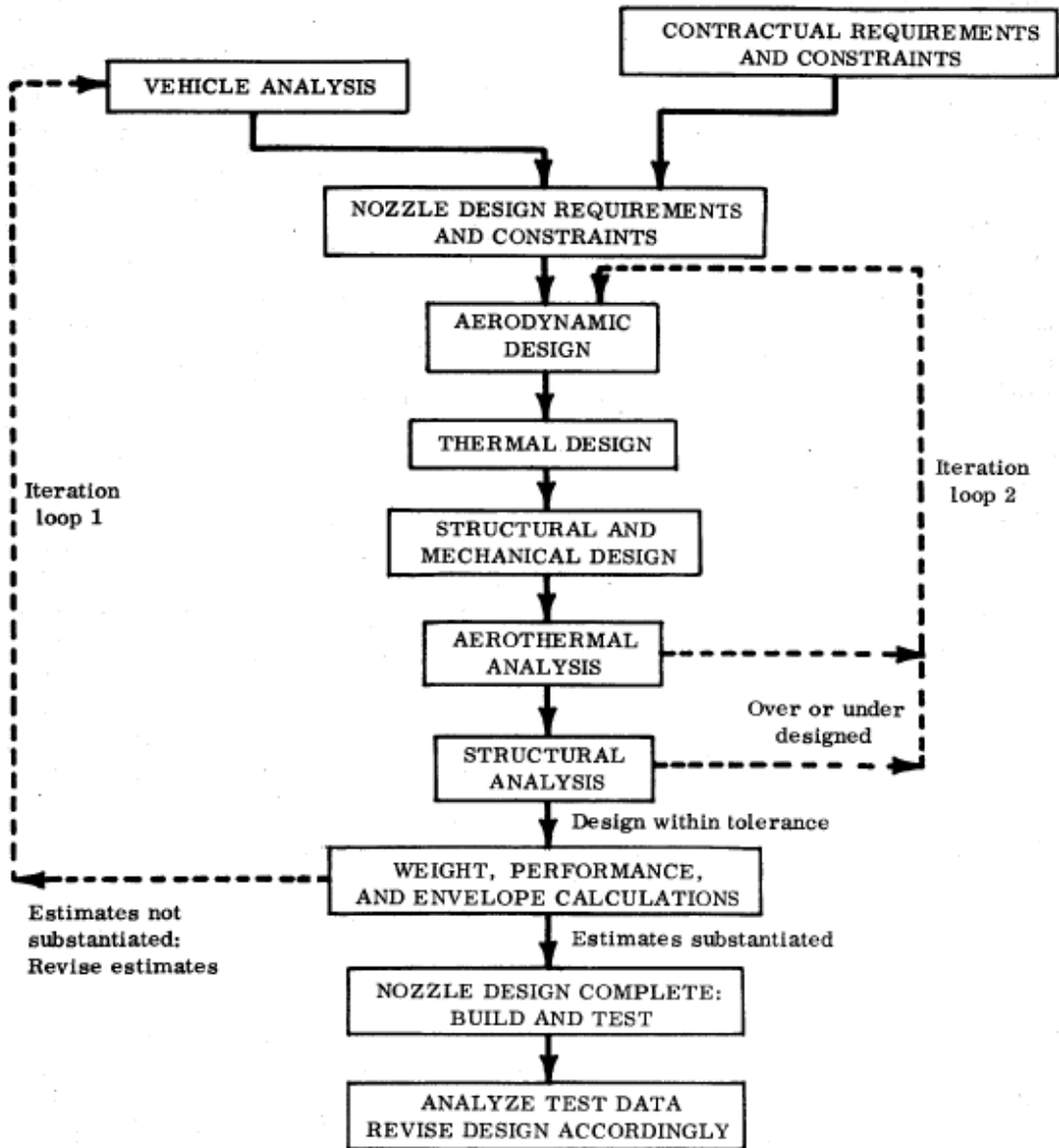


Figure A.1: Standard nozzle design procedure (NASA, 1975)

Appendix B: MATLAB code for nozzle loading calculations

Main Code

```
clc
clear all
close all

%% Nozzle Contour
progCon = waitbar(0,'Reading Nozzle Contour');

NozConFID = 'curve_workpoints.xls'; %filename of coordinates of workpoints
NozConRaw = xlsread(NozConFID); %reading spreadsheet into array

for j = 2:length(NozConRaw) %create new array exluding first row and z co-ord, convert from cm to m

    NozCon(j-1,1) = NozConRaw(j,1)/100; %x value
    NozCon(j-1,2) = NozConRaw(j,2)/100; %y value
    progressCon = j/length(NozConRaw);
    waitbar(progressCon)
end

rIn = NozCon(1,2); %Inlet radius
rEx = NozCon(length(NozCon),2); %outlet radius
[ minYValue,MinYInd] = min(NozCon,[],1); %finds smallest y value
rTh = minYValue(1,2); %Throat radius
rThInd = MinYInd(1,2); %Index of throat radius

ARIn = (rIn/rTh)^2;
AREx = (rEx/rTh)^2;

close(progCon)

%% Transients - Retrieve per second data

HRPCFID = 'HRPC_Motor_Performance.xls'; %filename of HRPC motor performance - transients
HRPCRaw = xlsread(HRPCFID); %Read transients into array

t = 1; %Counter initialisation - read from row number t

while isnan(HRPCRaw(t,1)) == 0
    HRPC(t,:) = HRPCRaw(t,:); %write only transient data to new array
    t = t + 1;
end

boolean = 1;
count = 1;
Pstart = 40e5; %Inital Pressure to start simulation - peak pressure

%Finds peak pressure and writes to first row in transient array
while boolean == 1
    if HRPC(count,20) >= Pstart
        boolean = 0;
        Trans(1,1) = HRPC(count,1); % Writes time - t
        Trans(1,2) = HRPC(count,15); % Wtites OF ratio - OFc
        Trans(1,3) = HRPC(count,20);% Writes pressure - Pc
        Trans(1,4) = HRPC(count,33); % Writes temperature - Tc
    end
end
```

```

    Trans(1,5) = HRPC(count,35); % Writes specific heat ratio - gamma
    Trans(1,6) = HRPC(count,49); % Writes Specific heat - Cp
    Trans(1,7) = HRPC(count,38); % Writes Characterstic velocity - C*
end
count = count + 1;
end

HRPCdeltaT = HRPC(2,1) - HRPC(1,1); %Calculates time step in HRPC output
stepTrans = 1/HRPCdeltaT; %Time steps needed in 1 second
step = count + stepTrans - 1;
w = 2; %counter

%Copies data from HRPC to Transient array at calculates/specified time steps
while step <= length(HRPC)
    Trans(w,1) = HRPC(step,1); % Writes time - t
    Trans(w,2) = HRPC(step,15); % Wites OF ratio - OFc
    Trans(w,3) = HRPC(step,20); % Writes pressure - Pc
    Trans(w,4) = HRPC(step,33); % Writes temperature - Tc
    Trans(w,5) = HRPC(step,35); % Writes specific heat ratio - gamma
    Trans(w,6) = HRPC(step,49); % Writes Specific heat - Cp
    Trans(w,7) = HRPC(step,38); % Writes Characterstic velocity - C*
    step = step + stepTrans;
    w = w + 1;
end

%Insert last time data into Transient array
Trans(w,1) = HRPC(length(HRPC),1); % Writes time - t
Trans(w,2) = HRPC(length(HRPC),15); % Wites OF ratio - OFc
Trans(w,3) = HRPC(length(HRPC),20); % Writes pressure - Pc
Trans(w,4) = HRPC(length(HRPC),33); % Writes temperature - Tc
Trans(w,5) = HRPC(length(HRPC),35); % Writes specific heat ratio - gamma
Trans(w,6) = HRPC(length(HRPC),49); % Writes Specific heat - Cp
Trans(w,7) = HRPC(length(HRPC),38); % Writes Characterstic velocity - C*

%% Getting viscosity, Prandtl number and specific heat from NASA CEA
%Sends OF ratio, chamber pressure and temperature to NASA CEA - Function file
progCEA = waitbar(0,'Accessing CEA');
for u = 1:length(Trans)

    OF = Trans(u,2);
    Pc = Trans(u,3)*10^-5; %Convert Pascal to bar
    Tc = Trans(u,4);
    [vis,pranEq,pranFz,cpCEA] = RunCEA(OF,Pc,Tc);
    Trans(u,8) = vis*10^-4; % Writes viscosity to transient array
    Trans(u,9) = pranEq; % Writes Equilibrium prandtl number to transient array
    Trans(u,10) = pranFz; % Writes Frozen prandtl number to transient array
    Trans(u,11) = cpCEA*10^3; % Writes specific heat from NASA CEA
    progressCEA = u/length(Trans);
    waitbar(progressCEA)

end
close(progCEA)

%% Temporal and spatial calculations

syms m %Variable for solving equations
Mmax = 4; %Max expected Mach Number for simulation

```

```

progTime = waitbar(0,'Time Calculations');

for time = 1:length(Trans) %Time loop

    pStag = Trans(time,3); %Stagnation pressure
    tStag = Trans(time,4); %Stagnation temperature
    k = Trans(time,5); %Chamber specific heat ratio
    Cpc = Trans(time,11); %Chamber specific heat
    cstar = Trans(time,7); %Characteristic velocity - C*
    mu = Trans(time,8); %Chamber viscosity
    PrEq = Trans(time,9); %Chamber prandtl number assuming equilibrium flow
    PrFz = Trans(time,10); %Chamber prandtl number assuming frozen flow

    ex = (k+1)/(2*(k-1)); %exponent of compressible isentropic flow equations

    progNoz = waitbar(0,'Countour Calculations');

    for q = 1:length(NozCon) %Calculations along nozzle contour - spatial loop

        %solve for mach number at each discrete point on contour
        ARx(q) = (NozCon(q,2)/rTh)^2; %area ratio at each point
        NozCon(q,3) = ARx(q); %write area ratio to NozCon array

        eqnX = (1/m)*((2/(k+1))*(1+((k-1)/2)*m^2))^ex == ARx(q); %set up equation to solve

        if q <= rThInd %checks whether position is in convergant or divergant section of
nozzle
            MCon = vpasolve(eqnX,m,[0 1]); %solves for mach in convergant section
            Mx(q) = MCon;
            disp('Conv')
        else
            MDiv = vpasolve(eqnX,m,[1 Mmax]); %solves for mach in divergant section
            Mx(q) = MDiv;
            disp('Div')
        end

        Mxt(q,time) = double(Mx(q));

        %calculate free stream property along nozzle contour

        Trat = 1 + (((k-1)/2)*(Mx(q)^2)); %Stagnation temperature/static

        Tx = tStag*(1/Trat); %local static pressure
        Temp(q,time) = double(Tx); %Free stream property array - Temperature (1), Pressure
(2), density (3)

        Prat = (Trat)^(k/(k-1)); %Static pressure calculations
        Px = pStag*(1/Prat);
        Pres(q,time) = double(Px);

        %Bartz equation
        corFacx = 1/(((0.5*(Tx/tStag)*Trat+0.5)^0.68)*(Trat^0.12)); %Correction factor

        %Bartz equation
        hg1 = 0.026/((2*rTh)^0.2);
        hg2Eq = ((mu^0.2)*Cpc)/(PrEq^0.6); %Equilibrium flow
        hg2Fz = ((mu^0.2)*Cpc)/(PrFz^0.6); %frozen flow
    end
end

```

```

hg3 = (pStag*9.81/cstar)^0.8;
R = 0.5*((1.5*rTh)+(0.382*rTh));
hg4 = (2*rTh/R)^0.1;
hg5 = ((rTh/NozCon(q,2))^2)^0.9;
hgEq(q,time) = double(hg1*hg2Eq*hg3*hg4*hg5*corFacx); %Equilibrium flow
hgFz(q,time) = double(hg1*hg2Fz*hg3*hg4*hg5*corFacx); %Frozen flow

progressNoz = q/length(NozCon)
waitbar(progressNoz)
end

close(progNoz)
progressTime = time/length(Trans)
waitbar(progressTime)
end

close(progTime)

msgbox('Operation Completed');

%% Plots

PresConTime = figure('Name','Temporal and Spatial Pressure Distribution','NumberTitle','off');
surf(Pres)
xlabel('Time (s)')
ylabel('Station Number along Nozzle Contour')
zlabel('Pressure (Pa)')
hidden off
title('Temporal and Spatial Pressure Distribution')

TempConTime = figure('Name','Temporal and Spatial Temperature Distribution','NumberTitle','off');
surf(Temp)
xlabel('Time (s)')
ylabel('Station Number along Nozzle Contour')
zlabel('Temperature (k)')
hidden off
title('Temporal and Spatial Temperature Distribution')

ConvConFzTime = figure('Name','Temporal and Spatial Convective Heat Transfer Distribution -
Frozen','NumberTitle','off');
surf(hgFz)
xlabel('Time (s)')
ylabel('Station Number along Nozzle Contour')
zlabel('Convective Heat Transfer Coefficient - Frozen (W/m2k)')
hidden off
title('Temporal and Spatial Convective Heat Transfer Distribution - Frozen')

ConvEqConTime = figure('Name','Temporal and Spatial Convective Heat Transfer Distribution -
Equilibrium','NumberTitle','off');
surf(hgEq)
xlabel('Time (s)')
ylabel('Station Number along Nozzle Contour')
zlabel('Convective Heat Transfer Coefficient - Equil (W/m2k)')
hidden off
title('Temporal and Spatial Convective Heat Transfer Distribution - Equilibrium')

MachTime = figure('Name','Mach Number','NumberTitle','off');
surf(Mxt)

```

```

xlabel('Time (s)')
ylabel('Station Number along Nozzle Contour')
zlabel('Mach Number')
hidden off
title('Mach Number')

VisTime = figure('Name','Viscosity vs Time','NumberTitle','off');
plot(Trans(:,1),Trans(:,8))
title('Viscosity vs Time')

PranEqTime = figure('Name','Equilibrium Prandtl Number vs Time','NumberTitle','off');
plot(Trans(:,1),Trans(:,9))
title('Equilibrium Prandtl Number vs Time')

PranFzTime = figure('Name','Frozen Prandtl Number vs Time','NumberTitle','off');
plot(Trans(:,1),Trans(:,10))
title('Frozen Prandtl Number vs Time')

OFTime = figure('Name','OF ratio vs Time','NumberTitle','off');
plot(Trans(:,1),Trans(:,2))
title('OF ratio vs Time')

GamTime = figure('Name','Specific Heat ratio vs Time','NumberTitle','off');
plot(Trans(:,1),Trans(:,5))
title('Specific Heat ratio vs Time')

CpTime = figure('Name','Specific Heat vs Time','NumberTitle','off');
plot(Trans(:,1),Trans(:,11))
title('Specific Heat vs Time')

Cstarime = figure('Name','Charactersitic Velocity vs Time','NumberTitle','off');
plot(Trans(:,1),Trans(:,7))
title('Charactersitic Velocity vs Time')

Nozzlecontour = figure('Name','Nozzle contour','NumberTitle','off');
plot(NozCon(:,1),NozCon(:,2))
title('Nozzle contour')
xlabel('axial length (m)')
ylabel('radial length (m)')

% Write pressure and heat Transfer coefficient with temperature to excel/csv for use in ANSYS - creates
multiple files for each time step

progFiles = waitbar(0,'Writing Transient Files');

PresNameHead = 'Pressure_Trans_';
HCTNameHead = 'Heat_Transfer_Coeff_Temp_Trans_';
FIDext = '.dat';

for iFID = 1:length(Trans)

    PcsvFID = strcat(PresNameHead,num2str(iFID),FIDext);
    %delete(PcsvFID)
    Pcsv(:,1) = double(NozCon(:,1));
    Pcsv(:,2) = double(NozCon(:,2));
    Pcsv(:,3) = double(Pres(:,iFID));
    csvwrite(PcsvFID,Pcsv)

```

```

movefile(PcsvFID, I:\Masters Work\Nozzle design\RDM Nozzle\Boundary layer
flow_transient\Transient Files\Pressure');

HCTcsvFID = strcat(HCTNameHead,num2str(iFID),FIDext);
%delete(HCTcsvFID)
HCTcsv(:,1) = double(NozCon(:,1));
HCTcsv(:,2) = double(NozCon(:,2));
HCTcsv(:,3) = double(hgFz(:,iFID));
HCTcsv(:,4) = double(Temp(:,iFID));
csvwrite(HCTcsvFID,HCTcsv)
movefile(HCTcsvFID, I:\Masters Work\Nozzle design\RDM Nozzle\Boundary layer
flow_transient\Transient Files\Convective Heat Transfer Coefficient and Temperature');

progressFiles = iFID/length(Trans)
waitbar(progressFiles)
end

close(progFiles)

```

Function code to access NASA CEA

```

function [vis,pranEq,pranFz,cpCEA] = RunCEA(OF,Pc,Tc)
%%
Fuel_1='Paraffin-Wax C 50 H 102'; % reactant - Fuel 1
wt_F1='100'; % weight percent of Fuel 1 [%]
Enthalpy_F1='-1438200'; % enthalpy of Fuel 1 [J/mol]
Temp_F1='298'; % inert temperature of Fuel 1 [K]
Fuel_2=""; % reactant - Fuel 2
wt_F2=""; % weight percent of Fuel 2 [%]
Enthalpy_F2=""; % enthalpy of Fuel 2 [J/mol]
Temp_F2='298'; % inert temperature of Fuel 2 [K]
Oxidiser='N2O'; % reactant - Oxidiser
OxidiserTemp='298'; % inert temperature of Oxidiser [K]
Only=""; % species that are the only ones to be considered as products
Omit=""; % species that are to be omitted as possible products

% OF = 3;
% Pc = 40; %enter bars
% Tc = 3600; %temperature in kelvin

part1='problem';
part2=' rocket ';
part3=' o/f = ';
part4=' p(bar) = ';
part5=' t(k) = ';
part7=' reac ';
part8=' fuel= ';
part9=' wt(%) = ';
part10=' h(j/mol) = ';
part11=' t(k)= ';
part12=' fuel= ';
part13=' wt(%) = ';
part14=' h(j/mol) = ';
part15=' t(k)= ';
part16=' oxid= ';

```

```

part17=' t(k)= ';
part18='outp';
part19=' siunits plot tranport vis pran pranfz cp';
part20='only';
part21='omit';
part22='end';

ofstring=num2str(OF);           % O/F ratio
pcstring=num2str(Pc);          % chamber pressure [bar]
tcstring=num2str(Tc);

name = 'Prop'; %CEA file name
inpFID = strcat(name, '.inp');

fid=fopen(inpFID, 'w');
fprintf(fid, '%s\n', part1);
fprintf(fid, '%s', part2);
fprintf(fid, '%s', part3);
fprintf(fid, '%s', ofstring);
fprintf(fid, '%s', part4);
fprintf(fid, '%s', pcstring);
fprintf(fid, '%s', part5);
fprintf(fid, '%s\n', tcstring);
fprintf(fid, '%s\n', part7);
fprintf(fid, '%s', part8);
fprintf(fid, '%s', Fuel_1);
fprintf(fid, '%s', part9);
fprintf(fid, '%s', wt_F1);
fprintf(fid, '%s', part10);
fprintf(fid, '%s', Enthalpy_F1);
fprintf(fid, '%s', part11);
fprintf(fid, '%s\n', Temp_F1);
fprintf(fid, '%s', part12);
fprintf(fid, '%s', Fuel_2);
fprintf(fid, '%s', part13);
fprintf(fid, '%s', wt_F2);
fprintf(fid, '%s', part14);
fprintf(fid, '%s', Enthalpy_F2);
fprintf(fid, '%s', part15);
fprintf(fid, '%s\n', Temp_F2);
fprintf(fid, '%s', part16);
fprintf(fid, '%s', Oxidiser);
fprintf(fid, '%s', part17);
fprintf(fid, '%s\n', OxidiserTemp);
fprintf(fid, '%s\n', part18);
fprintf(fid, '%s\n', part19);
fprintf(fid, '%s\n', part20);
fprintf(fid, '%s\n', Only);
fprintf(fid, '%s\n', part21);
fprintf(fid, '%s\n', Omit);
fprintf(fid, '%s\n', part22);
fclose(fid);

fid2=fopen('my_inputs.txt', 'w');
fprintf(fid2, '%s\n', name);
fclose(fid2);

dos('FCEA2.exe < my_inputs.txt');

```

```
fid3=fopen(strcat(name,'.plt'));
i=1;
tline=fgetl(fid3);

while ischar(tline)
    if i==2
        line2=tline;
    end
    tline = fgetl(fid3);
    i=i+1;
end
fclose(fid3);

numsline2=str2num(line2);
vis = numsline2(1);
pranEq = numsline2(2);
pranFz = numsline2(3);
cpCEA = numsline2(4);
end
```

Appendix C: Manufacturing drawings

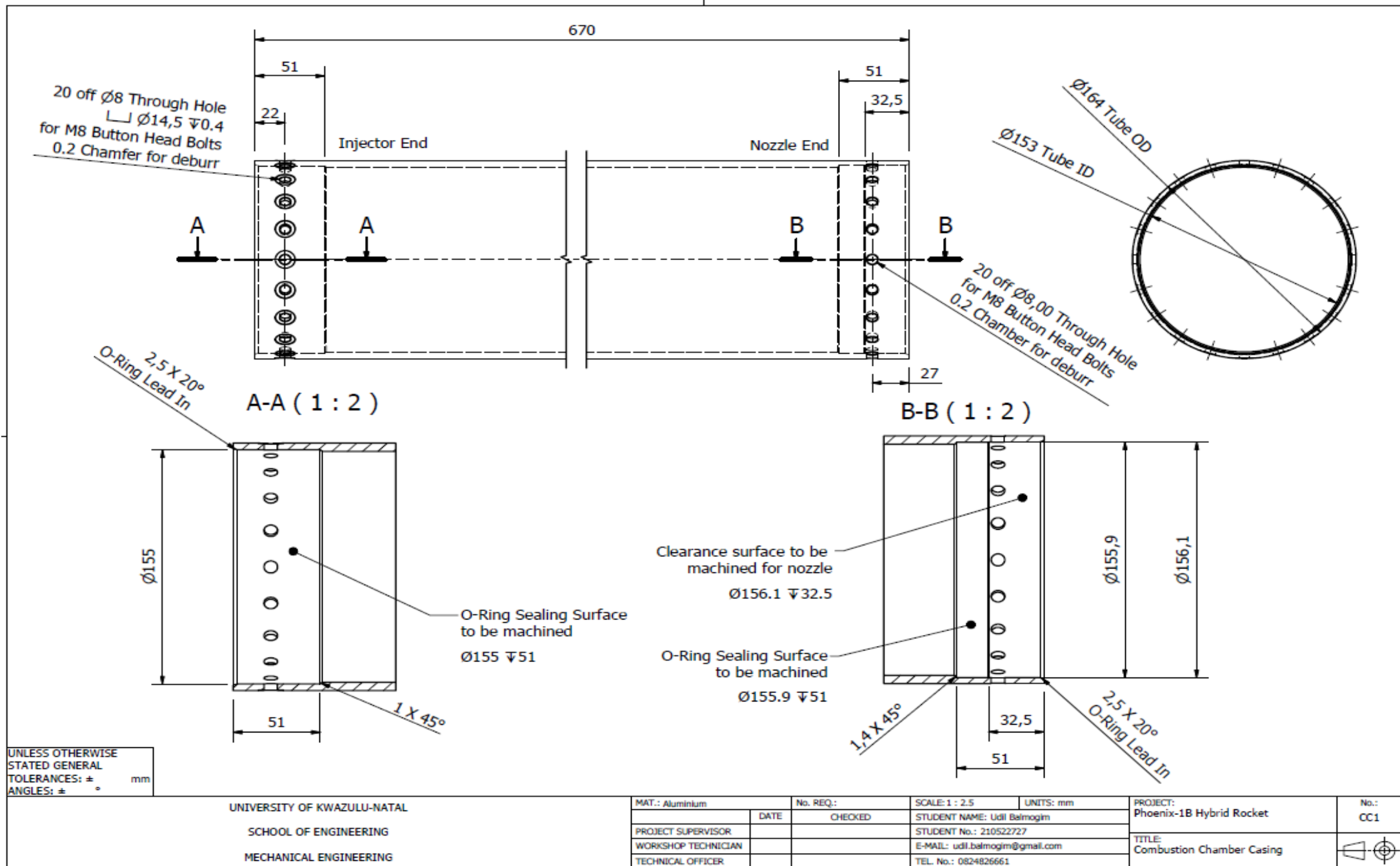
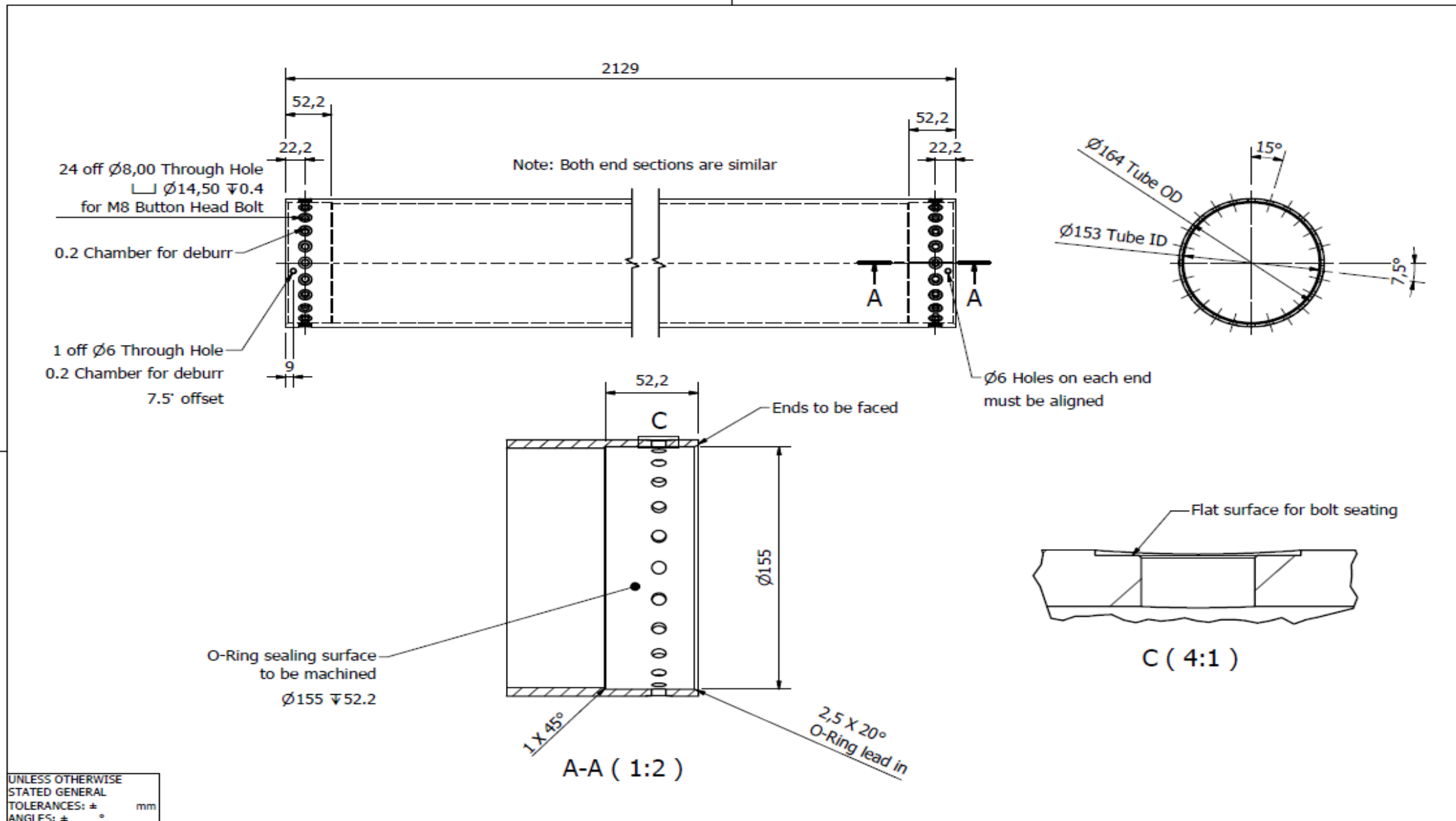


Figure C.1: Combustion chamber casing



UNLESS OTHERWISE STATED GENERAL TOLERANCES: \pm mm ANGLES: \pm °

UNIVERSITY OF KWAZULU-NATAL SCHOOL OF ENGINEERING MECHANICAL ENGINEERING	MAT.: Aluminium 6061 T6	No. REQ: 1	SCALE: 1 : 4	UNITS: mm	PROJECT: Phoenix-1B Hybrid Rocket	No.: OT1
	DATE	CHECKED	STUDENT NAME: Udil Balmogim			
	PROJECT SUPERVISOR		STUDENT No.: 210522727			
	WORKSHOP TECHNICIAN		E-MAIL: udl.balmogim@gmail.com		TITLE: Oxidiser Tank	
	TECHNICAL OFFICER		TEL No.: 0824826661			

Figure C.2: Oxidiser tank shell

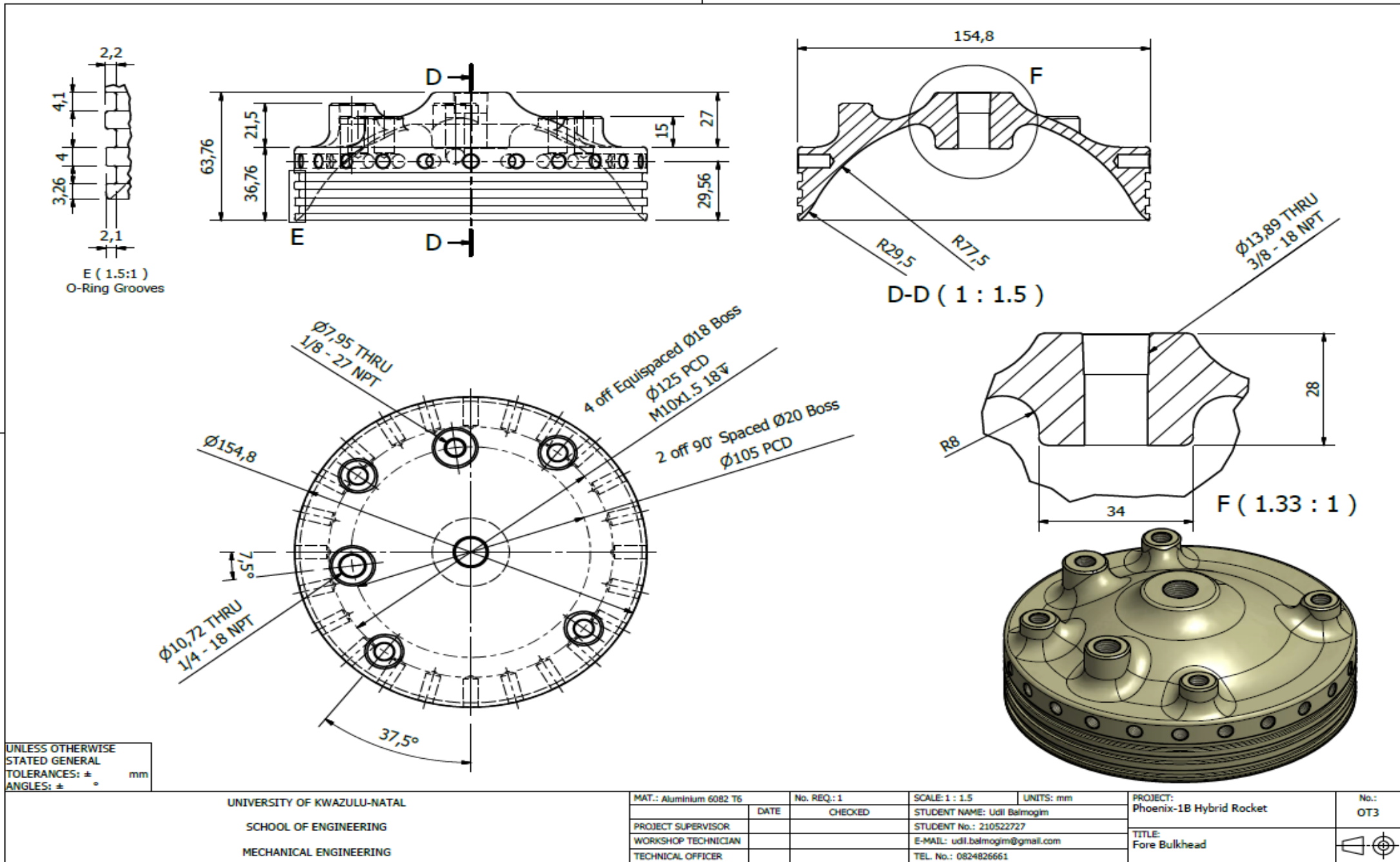


Figure C.3: Fore bulkhead

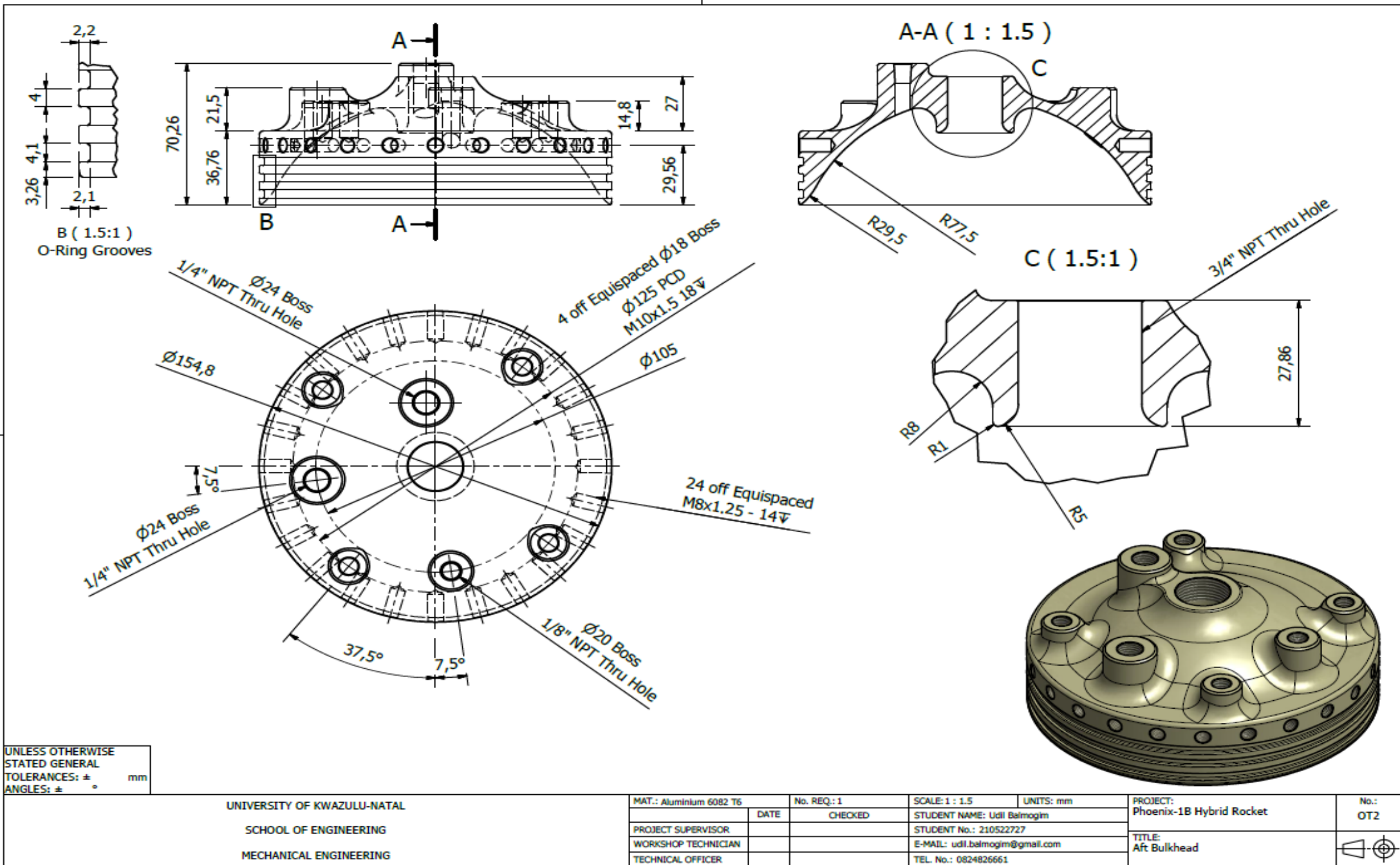


Figure C.4: Aft bulkhead

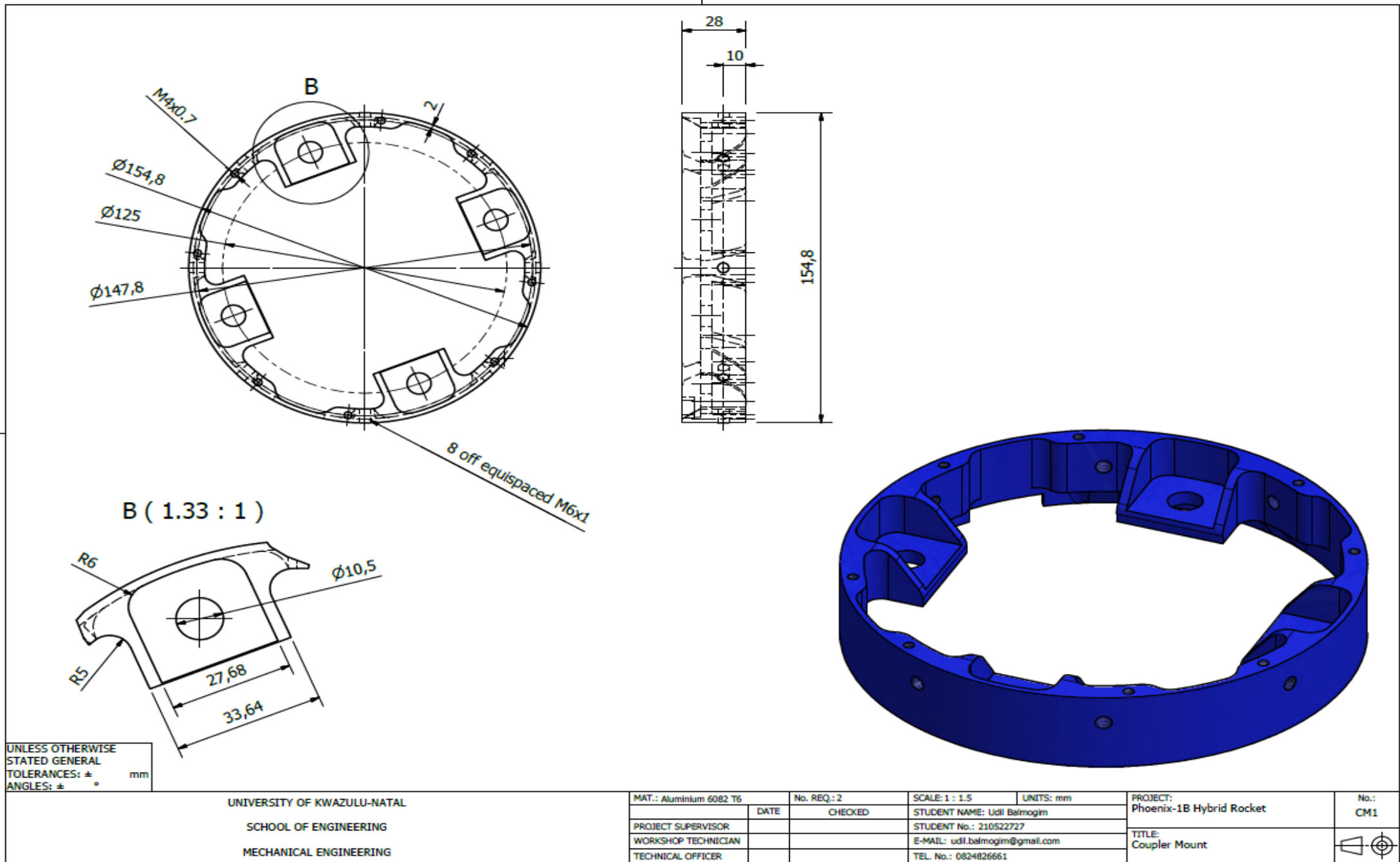
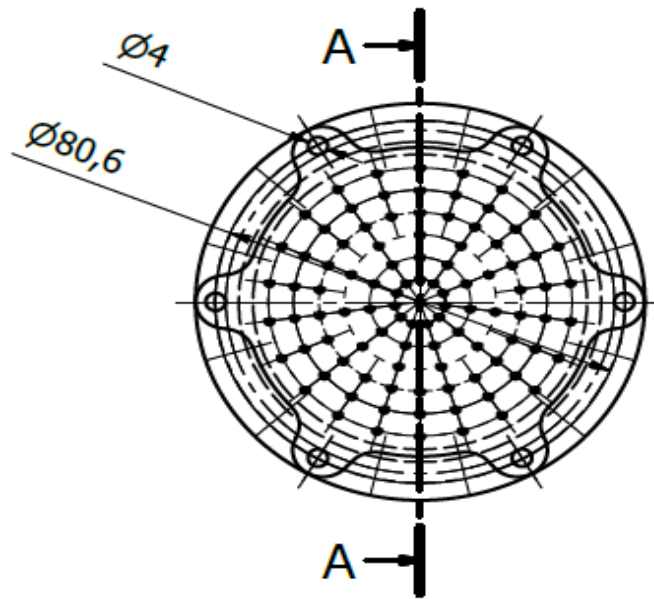
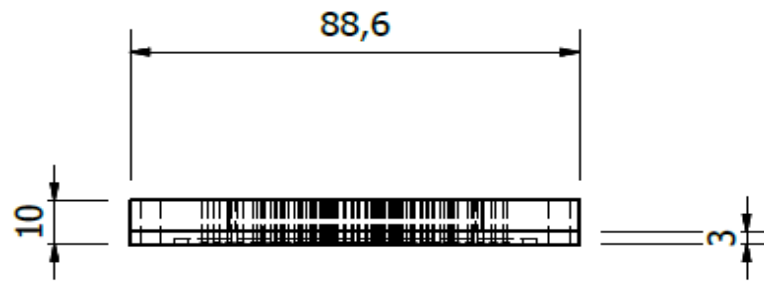
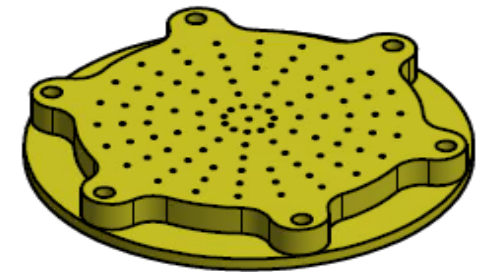
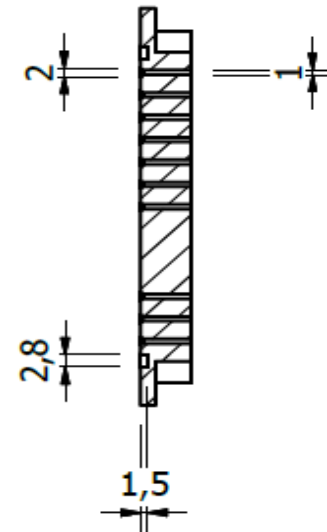


Figure C.6: Coupler mount



A-A (1 : 1.5)



UNLESS OTHERWISE
STATED GENERAL
TOLERANCES: \pm mm
ANGLES: \pm °

UNIVERSITY OF KWAZULU-NATAL SCHOOL OF ENGINEERING MECHANICAL ENGINEERING	MAT.: Brass	No. REQ.: 1	SCALE: 1 : 1.5	UNITS: mm	PROJECT: Phoenix-1B Hybrid Rocket	No.: CC6
		CHECKED	STUDENT NAME: Udil Balmogim			
	PROJECT SUPERVISOR	DATE	STUDENT No.: 210522727		TITLE: Injector Plate	
	WORKSHOP TECHNICIAN		E-MAIL: udil.balmogim@gmail.com			
	TECHNICAL OFFICER		TEL. No.: 0824826661			

Figure C.7: Injector plate

Appendix D: Videos

1. P1A hot fire test
2. P1A flight test
3. P1B Temporal and spatial temperature distribution in the final nozzle design
4. P1B Temporal and spatial Von Mises stress distribution in the final nozzle design
5. P1B cold flow test injector failure – normal playback speed
6. P1B cold flow test injector failure – slow motion

(CD disk will be provided here containing videos)